Development of Wide Band Gap Materials for Thin Film Silicon Solar Cells

vorgelegt von
Dipl.-Ing.
Simon Kirner
aus Berlin

von der Fakultät IV - Elektrotechnik und Informatik
der Technischen Universität Berlin
zur Erlangung des akademischen Grades

Doktor Ingenieur
- Dr.-Ing. -
genehmigte Dissertation

Promotionsausschuss

Vorsitzende:	Prof. Dr. Sibylle Dieckerhoff
Berichter:	Prof. Dr. Bernd Rech
Berichter:	Prof. Dr. Miro Zeman

Tag der wissenschaftlichen Aussprache: 11.07.2013

Berlin 2014
D83

Simon Kirner

Entwicklung von Kontakmaterialien mit hohem Bandabstand für Silizium Dünnschichtsolarzellen

Kurzfassung: Im Rahmen der vorliegenden Arbeit wurden Kontaktmaterialien mit hohem Bandabstand für den Einsatz in Silizium basierten Dünnschichtsolarzellen entwickelt. Genauer wurden Siliziumoxid- (SiO) und -karbid (SiC) -Schichten mit variabler Stöchiometrie mittels PECVD bei einer Anregungsfrequenz von 13.56 MHz hergestellt. Es wurde der Einfluss der Depositionsparameter auf das Schichtwachstum mittels Plasmadiagnostik, sowie auf die optoelektronischen und strukturellen Eigenschaften der resultierenden Schichten untersucht. Die Erhöhung der Depositionsleistung bewirkt bei mikrokristallinen Siliziumoxidschichten (μc-SiO_x:H) nicht die in einem mikrokristallinen Silizium (μc-Si:H) Regime sonst übliche Erhöhung der Kristallinität aufgrund des höheren Dissoziationsgrades, sondern im Gegenteil eine Verringerung. Dies konnte mit einem verstärkten Sauerstoffeinbau bei erhöhter Leistung erklärt werden. Die Kristallinität kann jedoch durch eine Erhöhung des Drucks im untersuchten Bereich wieder stark erhöht werden, was mit einer Verringerung des Ionenbombardements und/oder einer erhöhten Silanausnutzung erklärt werden konnte. Die Schichten wurden erfolgreich in a-Si:H/μc-Si:H Tandemsolarzellen als Zwischenreflektorschicht eingesetzt. Die Deposition einer dünnen μc-Si:H n-Schicht hinter der Reflektorschicht half dabei den Tunnelrekombinationskontakt wesentlich zu verbessern, welches sich in einem verringerten Serienwiderstand äußerte. Dieser Effekt konnte erfolgreich mittels Halbleitertheorie erklärt werden. Es wurde ein signifikanter Einfluss der Topographie des Substrats auf die Effektivität sowie auf die ideale Dicke des Zwischenreflektors beobachtet. Rigorose optische 2D Simulationen bestätigten dies und zeigten, dass insbesondere eine geringe Autokorrelationslänge der Oberflächenstruktur im Bereich von 100-300 nm dessen Effektivität begünstigt. SiC Schichten wurden in einem ähnlichen Regime abgeschieden wie die μc-SiO_x:H Schichten. Obwohl eine Kristallinität nicht erreicht wurde, können die präsentierten Ergebnisse eine Grundlage für die weitere Entwicklung bilden. Der Versuch der Kristallisierung von amorphen SiC Schichten mittels eines Elektronenstrahls zeigte erste vielversprechende Ergebnisse. Abhängig von der Stöchiometrie konnten Anzeichen der Bildung einer kristallinen SiC Phase beobachtet werden.

Development of wide band gap materials for thin film silicon solar cells

Abstract: In the frame of this work, wide band gap materials, in particular amorphous and microcrystalline silicon-oxide (SiO) and -carbide (SiC) layers, prepared by 13.56 MHz PECVD, were developed for application in thin film silicon solar cells. By means of optical, electrical and structural material characterizations combined with plasma diagnostics, the influence of the deposition parameters on the film growth were investigated. For microcrystalline silicon oxide (μc-SiO$_x$:H), it was found that with increasing deposition power, the crystallinity does not correlate with enhanced precursor dissociation as typical for pure microcrytalline silicon (μc-Si:H). Contrarily, it decreases significantly due to the higher observed oxygen incorporation. The crystallinity can be recovered by increasing the deposition pressure in the studied regime. This can be explained by reduced ion bombardment and/or increased silan depletion. The films were successfully applied as intermediate reflectors layer (IRL) in a-Si:H/μc-Si:H tandem solar cells. The deposition of a thin μc-Si:H n-layer behind the IRL was found to significantly improved the tunnel recombination junction resulting in a lower series resistance. The effect could be simulated using semi conductor theory. The effectiveness of the IRL in regard of the TCO substrate was investigated. Large differences regarding the effectiveness and the ideal thickness of the IRL were observed. Rigorous optical 2D simulations indicate that a low autocorrelation length of the TCO topography in the range of 100-300 nm increases the effectiveness significantly. SiC layers were deposited in a similar regime to the μc-SiO$_x$:H layers. Although no crystallinity was achieved, the presented approach can be a basis for further experiments. The electron beam crystallization of near stoichiometric layers showed first indications of a crystalline SiC phase.

Contents

1. Introduction

It is widely agreed that the excessive production of green house gases, that occurs during the generation of electricity by burning fossil fuels, is one of the main drivers for global warming. The external costs arising from this (i.e. costs that are not borne by the initiator), e.g. the increasing desertification or the steadily increasing probability of natural catastrophes [1], can thus be directly related to the prevalence of these technologies. Despite some efforts, the internalization of theses costs on a global level (through e.g. emission trading) is still not sufficient, mainly due to political reasons.

To increase the competitiveness of photovoltaic (PV) energy conversion against these discriminations, the cost for PV energy conversion has to be further decreased. One promising technology to reduce the module cost per watt is the thin film silicon solar cell technology. Here, the silicon is deposited directly onto a foreign substrate. The great advantage of this technology over the silicon wafer technology, which is currently dominating the PV module market, is the lower demand for energy and raw materials. The low energy demand results from the used process temperatures, which are typically below 250°C. Compared to other thin film technologies it has the further advantage that only inexpensive and abundant materials are used. Drawbacks of this technology are the low conversion efficiency, which is usually below 10 % for commercially available modules and the commonly used highly toxic gases. The low conversion efficiency is mainly due to the relatively low material quality and the resulting weak electronic properties compared to e.g. wafer based solar cells.

Solar cells based on amorphous hydrogenated silicon (a-Si:H) have already been produced for almost 40 years. The first production was reported by Carlson and Wronski in 1976 [2]. The technology was widely used in applications, where only low power was demanded and low costs were needed, such as in hand held calculators. With the increasing interest in PV in recent years, arising from the goal to have a more sustainable energy supply, a-Si:H based solar cells gained a lot of interest due its potential for very low cost per watt. Especially, this is appealing for large, utility scale PV plants.

The efficiency of a-Si:H based devices could be greatly enhanced by the combination with hydrogenated microcrystalline (μc-Si:H) silicon solar cells, which were first reported by Faraji et al. [3] and Flückiger et al. [4]. The combination of both cells into the a-Si:H/μc-Si:H technology, which was first shown by Meier et al. [5], allows high efficiencies of

currently up to 12.3 % [6]. Even higher efficiencies of up to 13.4 % were shown using an a-Si:H/μc-Si:H/μc-Si:H triple cell technology [7]. Compared to other solar cell technologies, however, these record efficiencies are still rather low. The fact that the cost for the whole PV system, usually scale with the *area* of the system and not with the installed *electrical power*, further severe the necessity for higher converions efficiencies of thin film silicon solar cells.

The main limitations of the a-Si:H/μc-Si:H solar cells are the light induced degradation of the a-Si:H top cell material, which are cause by the Staebler-Wronski effect [8] and the low absorption coefficient of the μc-Si:H bottom cell material, which is due to its indirect band gap. Due to the low absorption coefficient of the μc-Si:H, thicknesses of >2μm and an efficient light trapping are necessary to achieve high efficiencies for a-Si:H/μc-Si:H solar cells. The relatively high thicknesses mean a limitation to the throughput in this technology. The textured substrates needed for the light trapping, limit the electronic properties of the devices further.

To increase the current in the top cell without its thickness, an intermediate reflector layer can be used [9–11]. Thin solar cells are less affected by the light induced degradation and thus are more stable. The development of the intermediate reflector layer was one focus of this work. Another way to increase the current in the top cell is by reducing parasitic absorption in the doped layer [9–15]. These functional n- and p-type layers are necessary for the charge carrier separation, but usually do not contribute to the generated current. The challenge in the development of these layer is to achieve a low refractive index and a high bang gap at a sufficiently high conductivity. Wide band gap materials such as μc-SiO_x:H or a-SiC:H are commonly used for these applications as they fulfill the needed requirements .

A different approach, which avoids the limitations induced by the a-Si:H top cell, is the deposition of thicker layers of silicon and the successive crystallization by means of solid phase crystallization at high temperatures (e.g. 600°C) or by means of liquid phase crystallization, using for example a laser or an electron beam [16–18]. The resulting, so called poly silicon (poly-Si), has grain sizes up to the cm range and thus thicker devices should be possible, without severe losses in the electronic performance. Several cell designs are currently investigated. However, in all cell types, the parasitic absorption remains a limiting factor. To reduce these losses, the application of transparent functional layers is desirable. Another requirement for the application in poly-Si cells, is in many cases the stability against high temperature steps.

These were the starting conditions for this thesis: on the one hand, a fairly well known solar cell process existed that was to be further optimized, and on the other hand, a very new process existed where many fundamental issues were to be solved. As mentioned, the focus of this fork herein was to further increase the efficiency of these solar cells by

the optimization of the wide band gap layers. The development of these wide band gap layer focused relatively fast on the fabrication of microcrystalline silicon oxide (μc-SiO_x:H) and microcrystalline silicon carbide (μc-SiO_x:H) by means of plasma enhanced chemical vapor deposition (PECVD). Here again, the current state of the art regarding these materials was divers: μc-SiO_x:H had been developed for several years already and the process was fairly well understood. On the other hand, the process for the deposition of stoichiometric μc-SiC:H by PECVD was not yet explored extensively. However, the hypothesis was that μc-SiC:H can even outperform μc-SiO_x in its applicability as wide band gap material. Furthermore, it was believed that it is very resistant against high temperature steps occurring during the poly-Si crystallization processes. For μc-SiO_x:H, the growth and the dependence of the deposition parameter on the layer properties as well as the effect of the device integration were in the focus of this part of the work.

The optimization experiments could be referenced against a baseline process. In this baseline, a-Si:H/μc-Si:H solar cells with a stable efficiency of more than 9 % were made on a regular basis. The baseline process is based on a technology, which was prior to this work developed over many years at several research institutes and in collaboration with the industry. Among others, the Forschungszentrum Jülich [11, 19–22] and the Institute of Microengineering Neûchatel are to be mentioned [5, 10, 23–25].

The stable efficiency of the baseline process at the PVcomB could be step wise increased up to values above 11 % in the course of this work. During the many experiments, which were conducted to improve the solar cell process, important conclusions could be drawn regarding the processes, the deposited materials, their integration into the device and the interplay between the interface topography and the functioning of the device. Much knowledge, which was gained through the optimization for the deposition of μc-SiO_x:H, could be transferred and used to gain a deeper understanding regarding the deposition of μc-SiC:H. The conclusions and the experiments leading to these results are presented in the following work. The thesis is therefore structured as follows:

In chapter 2, the fundamentals about the materials, the device-structure and -functioning are described. Also, the fundamentals for the deposition of amorphous and in particular microcrystalline materials are presented.

In chapter 3, the experimental details are described. In the first part, the deposition tools are presented. Then, the technology for the fabrication of solar cells is described. In the final section, the characterization methods for the material and for the devices are introduced.

The chapters 4-6 contain the result sections. In the beginning of each chapter, the specific and recent literature is summarized to give the reader an overview of the current state of the art. Chapter 4 describes the results concerning the material studies of micro-

crystalline silicon oxide and chapter 5 the results regarding silicon carbide. Based on the findings in chapter 4, the integration of the microcrystalline silicon oxide layers in the a-Si:H/μc-Si:H solar cell baseline is described and the influence of the device performance is investigated.

Chapter 7 contains the summary and an outlook.

2. Fundamentals

In this chapter, the physical and technical fundamentals for this work are described. In section 2.1, important characteristics of the materials used for thin film silicon solar cells, namely hydrogenated amorphous and microcrystalline silicon (a-Si:H and μc-Si:H) and their alloys, are summarized. The second part 2.2 focuses on the functioning of the devices and the physical models used to describe them. Section 2.3 gives a brief introduction on plasma enhanced chemical vapor deposition with the emphasis on the techniques to deposit amorphous and microcrystalline silicon films. An overview of the basics for the materials, the functioning and the production processes for silicon thin film solar cell technology are given in the books by Schropp and Zeman [26] and Shah [27]. The fundamentals on PECVD can be found for example in the book by Lieberman and Lichtenberg [28].

2.1. Materials

The first part 2.1.1 of the materials section is about a-Si:H, the second part 2.1.2 about μc-Si:H and the third section 2.1.3 is about silicon alloys. This final part is again sub divided into a part about silicon oxide and a part about silicon carbide, which were fabricated in the frame of this thesis. A standard work regarding a-Si:H is the book by Street [29]. Information about a-Si:H and μc-Si:H in perspective of the application in solar cells can also be found in the above mentioned books [26, 27].

2.1.1. Hydrogenated Amorphous Silicon

Silicon is a chemical element of the fourth main group with the atomic number 14. Amorphous silicon compared to its crystalline counterpart (c-Si) differs in its long range order. Both have covalent bindings, however, in the amorphous phase, the binding-angles and -distances are not firm but statistically distributed. This leads to a blurring of the conduction and valence band and the formation of band tails. Furthermore, amorphous silicon has a high density of defects originating from open bindings between the atoms. These so called dangling bonds deteriorate the optoelectronic properties of the material significantly. The dangling bonds as well as the band tails can be understood as states

in the forbidden gap of the semi-conductor leading to recombination centers and defect absorption. The dangling bonds are amphoteric states, meaning they can be positively charged (acceptor like), neutral or negatively (donor like) charged by either being unoccupied, singly or dually occupied with electrons. The transport in a-Si:H is assumed to predominantly occur between the extended states, since the mobility in the defect states is significantly lower. The band gap in a-Si:H is therefore often referred to as mobility gap. An illustration of the effective density of states in the band gap is given in the right part of Fig. 2.1.[1]

A great technological advantage of amorphous- over crystalline-silicon is the fact that it can be deposited directly as a thin layer onto a foreign substrate by e.g. plasma enhanced chemical vapor deposition (PECVD). This was first shown by Sterling and Swann in 1965 [30]. Through the incorporation of hydrogen, which is usually present during the deposition by PECVD either from the precursor (typically SiH_4) or from an additional H_2 dilution, a large amount of dangling bonds can be passivated by hydrogen atoms. The number of dangling bonds can be reduced this way to below 10^{16} cm^{-3}, significantly improving the optoelectronic properties of the material. It is then typically referred to as hydrogenated amorphous silicon (a-Si:H) and is of high technological use, e.g. for thin film transistors or thin film solar cells. A schematic picture of the material is shown in the left part of Fig. 2.1.

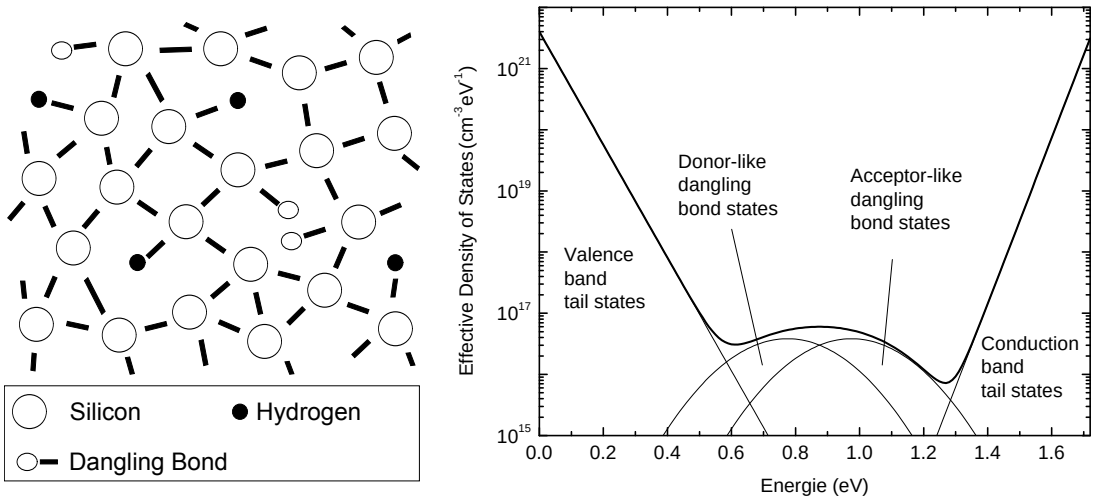

Figure 2.1.: (Left) A schematic illustration of the a-Si:H network and (right) its effective defect density of states as a function of energy. The sum (thick line) and the components from tail and dangling bond states (fine lines) are indicated, respectively. The parameters are taken from [26].

[1] For the calculation, the standard model for the description of the dangling bond states was used. Here, the amphoteric nature of the dangling bond states are approximated by two Gaussians, one representing the acceptor like and the other the donor like dangling bond states, which can either be occupied or unoccupied.

Due to the amorphous network, the k-selection rule diminishes, making a-Si:H a quasi direct semi-conductor with an increased absorption coefficient compared to c-Si in the visible wavelength region. This characteristic makes a-Si:H applicable as a wide-band gap absorber layer for multi-junction solar cells.

The electronic properties of a-Si:H are metastable: Upon illumination, the defect density of the material increases by typically more than one order of magnitude, deteriorating the quality of the material [31]. The effect can be reversed by annealing at 200°C [29]. This effect is known as the Staebler-Wronski-Effect (SWE) [8]. Solar cells incorporating absorber layers consisting of a-Si:H or its alloys suffer from the SWE in the way that the conversion efficiency decreases during the first hours of use. Depending on the spectral intensity and the temperature, an equilibrium is restored after a while and the conversion efficiency can be considered as *stable*. Typically, the cells are considered stable after 1000 h under standard test conditions (one sun illumination at 50°C), whereas most of the degradation occurs during the first 100 – 200 h. Results of studies regarding the stability of a-Si:H based solar cells fabricated for this work are given in section 6.4.

Doping of a-Si:H can be achieved via the implementation of boron for p- and phosphorous for n-type doping [32]. As with alloying, doping increases the defect density of the material, which can eventually counteract the doping effect: Charged defects energetically positioned close to the band edges pin the Fermi level and thus hinder a further decrease of the activation energy to below several hundreds of meV. The conductivity of n-type material is thus limited to a value of around 10^{-1} S/cm and that of p-type material to around 10^{-2} S/cm . The difference is explained by the fact that the conduction band tail is steeper compared to the valence band tail and thus the Fermi-level can be shifted closer to the conduction band [29].

2.1.2. Hydrogenated Microcrystalline Silicon

Hydrogenated microcrystalline silicon (μc-Si:H) can be produced in similar deposition systems as a-Si:H (such as PECVD). The material consists of a crystalline and an amorphous phase and typically voids [33]. A schematic view is given in Fig. 2.2. The first report about the deposition of μc-Si:H by means of PECVD was reported by Usui and Kikuchi in 1979 [34]. An overview of μc-Si:H and its application for thin film silicon solar cells is given e.g. by Rech et al. [19, 35] or in the books by Schropp and Zeman [26] and Shah [27].

The crystallinity of the material can be, for example, achieved via a high hydrogen dilution in the gas phase. The process is described in more detail in chapter 2.3. The crystallites typically grow in a columnar structure in the direction of the growth and can have sizes of a few 100 nm depending on the deposition properties as Fig. 2.2 suggests. The

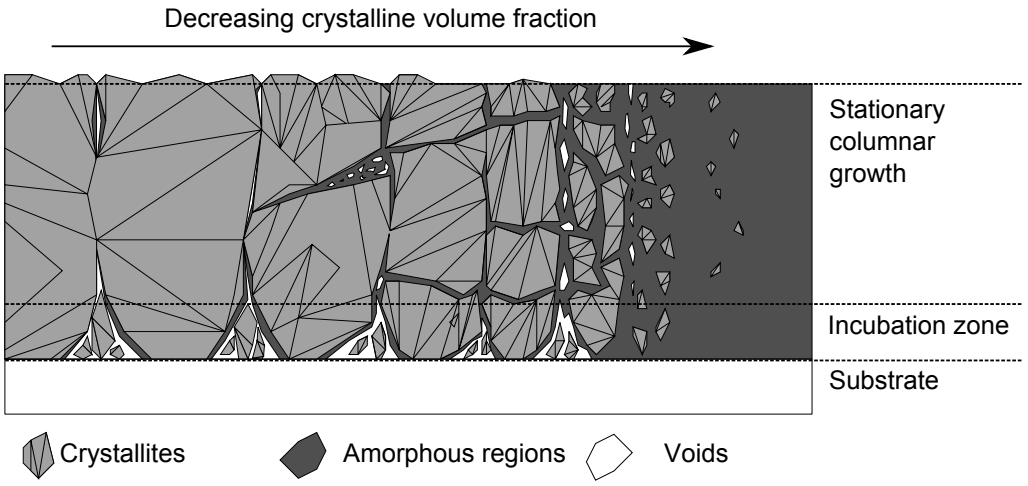

Figure 2.2.: Schematic view of the structure of microcrystalline silicon with different crystallinities according to [33].

optical properties of μc-Si:H are closer to c-Si with an increased absorption coefficient α between 700 – 1100 nm wavelength and a reduced α in the blue part of the spectrum (compare Fig. 2.3). This makes μc-Si:H an appropriate material for the use as a low-bandgap absorber material in multi junction solar cells. Due to the crystalline phase, its electronic properties are also greatly improved compared to a-Si:H. The dark conductivity increases strongly with the crystalline volume fraction. The best deposition regime for μc-Si:H based solar cells, however, is not at the highest crystallinity but near the on-set of crystallization, which is due to a reduction in the open circuit voltage with increasing crystallinity [33, 36]. As the a-Si:H passivates open bindings at the surface of the silicon grains in μc-Si:H, the reduction in open circuit voltage can be explained by an increase in the defect density resulting from the absence of sufficient a-Si:H [37]. Unlike a-Si:H, the metastability of the electronic properties of μc-Si:H under illumination are negligible from a certain crystallinity onwards.

The doping of μc-Si:H can be achieved in a similar manner as in a-Si:H, however the activation energy can be reduced further down to some 10 meV [26]. The conductivity of optimized microcrystalline doped layers is about a factor 1000 higher than in the amorphous material at room temperature [20].

2.1.3. Amorphous and Microcrystalline Silicon Alloys

The absorption coefficient as well as the refractive index of a-Si:H can be alternated by changing the deposition parameters, which is especially of great use when developing thin film silicon solar cells. In particular, through the addition of carbon, oxygen or nitrogen into the amorphous silicon network, the optical band gap increases, which is the

reason for the use of silicon alloys as window layers in thin film silicon solar cells. The widening of the absorption edge through the incorporation of foreign atoms, however, is typically accompanied by an increase in the defect density. Therefore, these silicon alloys are commonly not used as materials for absorbers, despite some reported experiments [38]. Amorphous silicon germanium (a-SiGe:H) on the other hand, an alloy with a more narrow band gap, has led to some considerable improvements in the conversion efficiency of thin film silicon solar cells in the past [39, 40]. Fig. 2.3 shows the absorption coefficients of a-Si:H and μc-Si:H and the wide band gap materials μc-SiO$_x$ and μc-SiC. For the latter, the absorption coefficients for two different polytypes (3C-SiC and 6H-SiC) are shown.

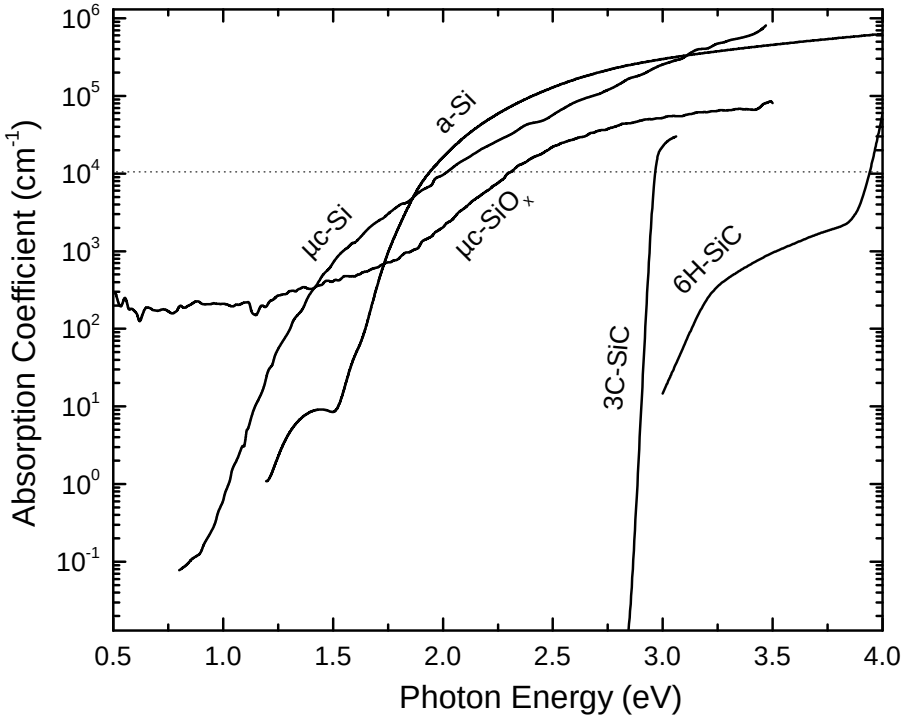

Figure 2.3.: Absorption coefficients as a function of photon energy for a-Si:H, μc-Si:H, μc-SiO$_x$:H, 3C-SiC and 6H-SiC. The data for μc-SiO$_x$:H was measured in the course of this thesis, the others are taken from literature [41, 42].

Silicon Oxide

Hydrogenated silicon oxide (SiO$_x$:H) can be deposited by PECVD with varying stoichiometry (from Si-rich semi conductor material to pure SiO_2) by admixture of e.g. CO_2 to the gas phase. As the Si-O binding energy is higher than the one of the Si-Si bond, the band gap increases up to 7 eV, similar to Vegard's law for alloys [43, 44]. With increased optical band gap, the conductivity of doped amorphous silicon oxide (a-SiO$_x$)

drops significantly by several orders of magnitude [45]. By adjusting the deposition parameters in a way similar to the ones used to obtain pure μc-Si:H, one can fabricate a two phase material consisting of a microcrystalline Si phase within an a-SiO$_x$:H network. This way, the material becomes significantly more conductive [11]. A transmission electron microscopy - energy dispersive x-ray spectroscopy (TEM-EDX) image of a μc-SiO$_x$:H sample prepared at the PVcomB is shown in Fig. 2.4.[2] The current understanding of this material is such that, similar to the growth of μc-Si:H, nucleation sites form on the surface that expand along the growth direction of the film. The silicon crystallites, also referred to as 'Si-filaments', have a diameter of down to a few nanometers and are embedded in a matrix of a-SiO$_x$:H [15]. From the colors in Fig. 2.4, one can distinguish between the a-SiO$_x$:H phase and the μc-Si:H phase.

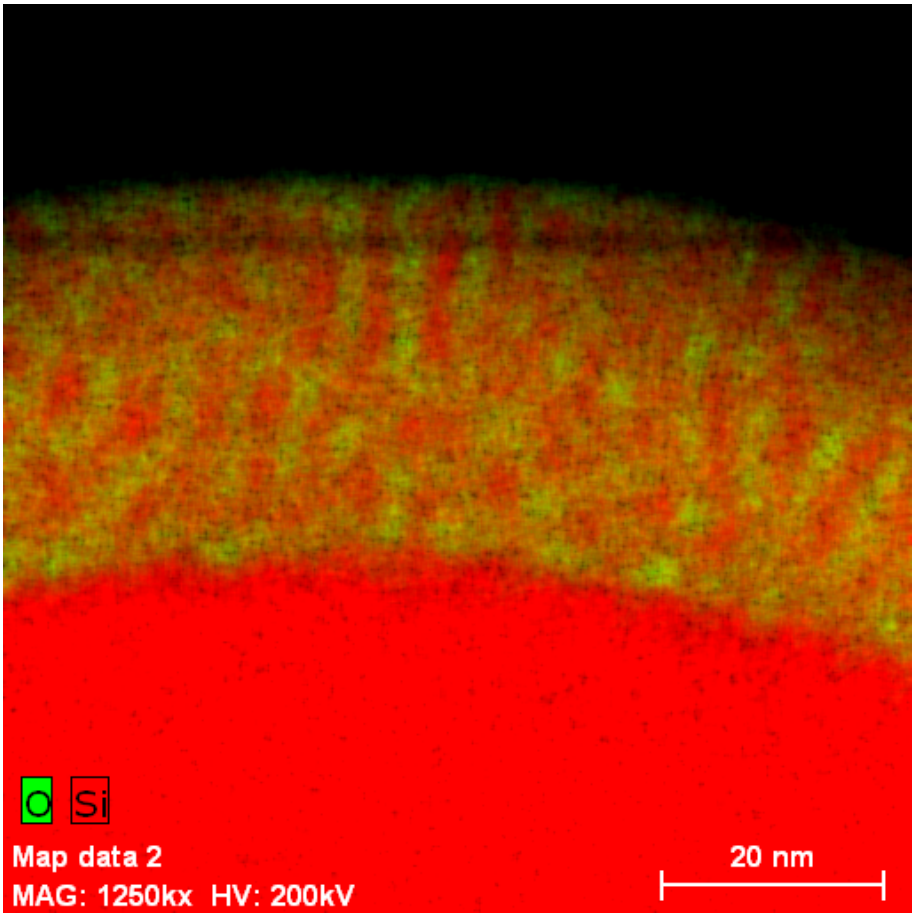

Figure 2.4.: Transmission electron microscopy – energy dispersive x-ray spectroscopy image of a μc-SiO$_x$:H layer on top of an a-Si:H layer. The green color indicates the a-SiO$_x$:H and the red color the μc-Si:H phase.

Recently, the use of μc-SiO$_x$:H at various positions in a-Si:H based thin film solar cells and

[2]The TEM image was prepared by Max Klingsporn in the context of his PhD thesis.

particular the use of its tunable optical properties have allowed to increase the efficiency of such devices significantly. A detailed literature overview of the application of this material can be found in the beginning of chapter 4. The study of the influence of the deposition parameters onto the material was one main focus of this work together with its application in solar cells, which is described in chapter 6. The goal therein is to optimize the material in such a way that the optical band gap is maximized at a (for the application in the solar cell) sufficiently high conductivity. This is realized by reducing the amount of μc-Si:H to its minimal required amount while maximizing the oxygen incorporation into the a-SiO_x:H phase.

Silicon Carbide

Microcrystalline silicon carbide (μc-SiC:H) has the potential to have even better optoelectronic properties than μc-SiO_x:H. Crystalline silicon carbide has, depending on its lattice structure, an optical band gap between 2.8 – 3.3 eV (see Fig. 2.3) and at the same time high charge carrier mobilities. Furthermore, it is known to be very temperature stable and, thus, could be used as wetting layer or diffusion barrier for crystallization processes [17, 18]. The abbreviation μc-SiC:H has been used in literature in two different connotations: In the first case, the material is a two-phase system consisting of a μc-Si:H and an a-SiC_x phase similar to the structure of μc-SiO_x:H [46, 47]. This type of material is denoted as μc-SiC_x:H in the following. The other type of material denoted here as μc-SiC:H, consists of a microcrystalline silicon carbide (μc-SiC) phase in an a-SiC_x:H matrix and has the desirable optoelectronic properties. Illustrations of the microstructure of the different materials are shown in Fig. 2.5. Crystalline silicon carbide is polymorphous with more than 200 different known polytypes. The most common ones are the cubical 3C-SiC and the hexagonal 4H- and 6H-SiC. Very common are also the mixtures of several poly-types [48].

2.2. Thin Film Silicon Solar Cells

The following section is devoted to the fundamentals of thin film silicon solar cells. The first part (2.2.1) discusses the device structure of the solar cells. In particular, it describes the functioning of thin film silicon solar cells. The second part (2.2.2)discusses two strategies how to improve photon absorption in the device in order to obtain high short circuit current densities. In this perspective, the role of the transparent conducting oxide (TCO) is described, which usually acts both as the front contact and as a light scatterer. The role of the intermediate reflector, whose development was one focus of this work, is also described in greater detail.

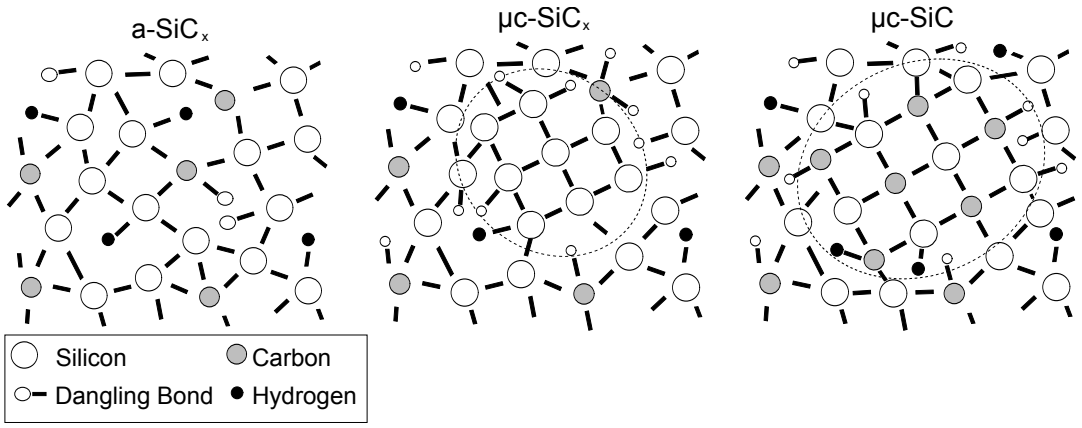

Figure 2.5.: Scheme of pure amorphous silicon carbide (a-SiC$_x$:H - left), a-SiC$_x$ containing a crystalline silicon phase (μc-SiC$_x$:H - middle) and a-SiC$_x$:H containing a crystalline silicon carbide phase (μc-SiC:H - right). The crystalline regions are enclosed by the dashed lines.

2.2.1. Device Structure

Thin film silicon solar cells are usually deposited as p-i-n-(or n-i-p-)single or -multi junction cells. An exception is the poly-Si cell, which is designed in a p-n-(or n-p-) configuration. The functioning, the differences and similarities of the different cell structures are described in the following.

a-Si:H- and μc-Si:H-based Single- and Multi-Junction Cells

In the p-i-n configuration, an intrinsic absorber layer is deposited in between two thin doped layers. The illumination is usually performed through the p- rather than the n-side of the device, due to the lower mobility of the holes. The p-layer plays thus a critical role, both, electronically and optically. For a long time, a-SiC$_x$ was the state of the art material for this layer [49, 50] whereas lately μc-SiO$_x$:H was successfully applied here due to the above mentioned reasons (compare section 2.1.3 and references [51, 52]). Often, the p-layer stack consists of a multi layer system with the first thinner layer being more conductive (less transparent) to assure a proper tunnel contact to the n-type TCO and the following layers being less conductive (more transparent) and thicker, to assure a sufficient field over the i-layer [53, 54]. The field is spanned over the entire i-layer and the transport is dominated by drift- more than by diffusion-currents. This design is used because of the rather poor electronic properties of the absorber materials and the resulting low charge-carrier diffusion length. A drawback of this design is that it limits the optimal thickness of the absorber layer. The device is limited by charge carrier recombination in the bulk. With increasing bulk thickness, this effect is more pronounced, which leads to a decrease in fill factor and open circuit voltage with increasing thickness, far below a

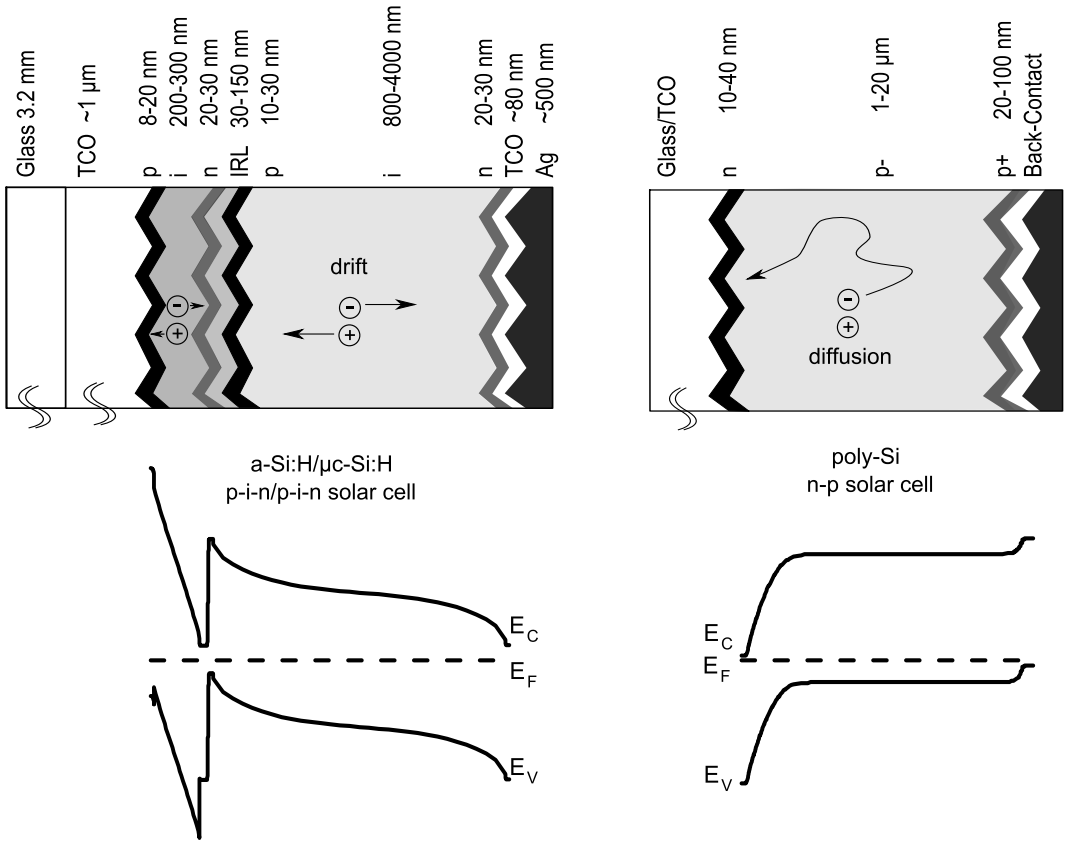

Figure 2.6.: The typical device structure and the schematic band diagram of a a-Si:H/μc-Si:H tandem solar cell and a poly-Si solar cell.

thickness were most of the light can be absorbed. This characteristic is even more pronounced because of the p-i-n design and the fact that the electric field across the i-layer decreases with increasing thickness. For μc-Si:H single-junction cells, this was shown experimentally by Vetterl et al. [55]. For a-Si:H solar cells, the effect of the light induced degradation (LID) is also more pronounced for thick cells. This is also due to more recombination inside the intrinsic layer due to the lower electric field [56, 57]. Different models for the transport in p-i-n-cells are given for example by [58] or [59].

To overcome the issue of the necessary thin layers and the resulting low light absorption within one cell, several p-i-n cells can be stacked monolithically on top of each other. Preferably, the band gap of the intrinsic layers is then adjusted, so that the material with the highest band gap is closest to the light source and the following i-layers have a smaller band gap. In this configuration, the sub-cell closest to the light-source can be very thin, even below 100 nm in some cases [57], which is favorable for the stability of the device performance. The following i-layers can be thicker without (in case they are amorphous) suffering much from LID. This is due to the fact that the light entering these layers has

less intensity and thus less defects are being created. Another advantage of multi junction solar cells in case of adjusted band gaps is the decrease of thermalization losses and the resulting increase in open circuit voltage. As mentioned in section 2.1.3, the absorption coefficient of a-Si:H and μc-Si:H can be varied to some extent through the deposition conditions as well as through alloying. To connect the sub cells loss free, low ohmic tunnel recombination junctions (TRJ) have to be formed at the interfaces. The challenges in the TRJ design with wide band gap layers are discussed in detail in section 6.1.

The sub cells are connected in series such that the current is limited by the cell, which generates the least current. Typically, the cell reaches its highest efficiencies, if the currents of all cells are matched, whereas the fill factor increases with the mismatch [60]. The current matching can be performed either by adjusting the thicknesses of the sub cells or by adjusting the reflectivity of the intermediate reflector layers (see section 2.2.2). Common configurations of p-i-n multi junction solar cells reported in literature are given in table 2.1. Also depicted are the typical thicknesses of the silicon absorber layers and the highest reported efficiencies.

Table 2.1.: Typical thicknesses and efficiencies of several types of multi junction thin film silicon solar cells

Type	Typical Silicon Thickness(nm)	Stable Efficiency (lab scale)	Reference
a-Si:H	200 – 300	10	[61]
μc-Si:H	1600	10.9	[62]
poly-Si	1400	10.5	[16]
a-Si:H/a-Si:H	300 – 400	10	[63]
a-Si:H/μc-Si:H	1000 – 4000	12.3	[6]
a-Si:H/a-SiGe:H/μc-Si:H	2000	12.5	[40]
a-Si:H/μc-Si:H/μc-Si:H	3500 – 6000	13.4	[7]

Despite the higher efficiencies of the triple cells, the a-Si:H/μc-Si:H tandem cell, also known as the 'Micromorph Cell' [5, 23], is probably the most attractive device for the manufacturing in industry due to its relatively low thickness, low deposition time and absence of the expensive material Germanium. The focus of this work lies thus on the improvement of the a-Si:H/μc-Si:H tandem cell, however, the developed layers are most likely also beneficial for other device types. A sketch of an a-Si:H/μc-Si:H tandem solar cell on a rough substrate is shown in Fig. 2.6.

Poly-crystalline Si Solar Cells

Besides the typical thin film silicon solar cells consisting of single- or multi- p-i-n-junctions, the research in the field of silicon solar cells is also focused on so called poly-crystalline Silicon (poly-Si) solar cells [16, 18, 64–66]. In this device, the high conversion efficiencies of the wafer-based technology shall be combined with the advantages of the thin film solar technology, such as lower demand for energy and raw material, simple and inexpensive manufacturing processes and the integrated series connection (see chapter 3.2 for further details). Poly-Si refers to a type of silicon with grain sizes that can be up to a few cm in size. It is typically deposited on a foreign substrate such as glass or metal and then crystallized using high temperature steps (solid phase crystallization, SPC) [66] or melted and then crystallized (liquid phase crystallization, LPC) [18] using for example a laser or an electron beam as energy source. It is therefore also referred to as 'recrystallized' silicon. Due to the larger grain size, the material quality is better than that for μc-Si:H and thicker absorber layers (>10 μm) should be possible without major deductions in the electronic properties. Therefore, these cells are made in a p-n or diffusion-driven-design as depicted in Fig. 2.6, where the bulk of the cell consists of a slightly doped material and the junction is formed by a thin, heavily doped emitter. Thus, the problem of the p-i-n cell arising from the decreasing electric field with increasing thickness described in section 2.2.1, is avoided.

An important issue in the development of the SPC process, at the moment, is the diffusion of foreign atoms out of the substrates, due to the relatively high temperatures occurring to the substrate during the crystallization of the silicon. Usually, diffusion barriers made of silicon alloys such as SiC_x, SiN_x or SiO_x are used to prevent the contamination of the absorber layers. In the context of this work, also diffusion barrier layers based on SiC_x were developed. For the LPC process, SiC_x layers play an important role as wetting layers to prevent the molten silicon from clustering upon crystallization. A current topic of interest is to combine this wetting layer with the function of a back-surface field by doping the layer heavily with boron. Using this technique, charge carriers that were generated inside the bulk are prevented from recombining at the rear-side.

2.2.2. Light Management Techniques

Light management describes the techniques to increase the light absorption in the active layers by light trapping, which is relevant for both described cell types, and the distribution of light to improve the matching of multi junction solar cells.

TCO Front Contacts

As described above, the absorption of thin film silicon solar cells is limited by (a) the low absorption coefficient of crystalline silicon (independent of the grain size) and (b) by the increased instability of thick a-Si:H (sub) cells. This leads to optimized thicknesses far below values where most of the potential solar spectrum is being absorbed during one light pass (some absorption coefficients are given in Fig. 2.3 and thicknesses are given table 2.1). To reduce this disadvantage, rough substrates are usually used to enhance the optical path length of the light through the device. Together with an efficient back reflector, the light path can be significantly enhanced leading to thin film silicon solar cells with short circuit current densities >28 mA/cm^2 [67] (for comparison wafer cells with 200 – 300 μm thickness can absorb up to 43 mA/cm^2 [68]. The theoretical limitations of light scattering were discussed by Yablonovitch [69].

For p-i-n cells, the substrate can either be in between the light source and the device as depicted in Fig.2.6 (superstrate- or p-i-n-configuration) or behind the device (substrate- or n-i-p-configuration) (the nomenclature for poly-Si cells is accordingly). As mentioned in section 2.2.1, the p-layer usually faces the light due to the lower mobility of the holes in p-i-n cells. The effect is less pronounced for poly-Si cells, due to the higher mobilities. In the first case, the superstrate should be as transparent as possible and usually glass coated with a transparent conducting oxide is used. In the latter case also opaque substrates such as metals or plastics can be used. Due to the limited in-plane conductivity of the silicon, the front electrode TCO transfers the current laterally and thus has to have an appropriate thickness of between 250 nm and two microns depending on its conductivity. The choice of TCO usually dominates the performance of the solar cell, due to its position in the device and its function as a light scatterer. The most important interplays between the TCO and an a-Si:H/μc:H-Si solar cell can be summarized into four points:

1. The *TCO/p-layer* contact has to be adjusted according to the electrical properties of the front contact and its stability against hydrogen plasmas [70, 71].
2. The *current matching* of the solar cell depends on the light scattering behavior. 2D simulations performed on periodic structures suggest that smaller features with a height and period of around 200 – 300 nm are ideal for the current in the top cell, whereas large features with a height and period of one micron and more are advantageous for the scattering in the red and infra-red region of the spectrum and are thus ideal for the μc-Si:H or poly-Si (sub-)cells [72, 73].
3. The *growth* of the silicon, especially the one of the μc-Si:H sub-cell, is strongly influenced by the topography of the superstrate - usually very narrow, sharp features, which have the most interesting optical properties, hinder the quality of the μc-Si:H growth [74, 75].

4. The topography of the TCO also has a high influence on the *performance of the intermediate reflector*. This interplay has been observed experimentally [76, 77] and partially by optical simulations [78]. A systematic study on this interplay is described in detail in chapter 6.3.

For the poly-Si solar cell, the stability of the TCO against high temperatures is essential as well as a thermal expansion coefficient close to the one of silicon. The TCOs used at the PVcomB can be grouped into three types, which are described in the following:

1. *Fluorine doped tin oxide (SnO_2:F)*, SnO_2:F is a common TCO used in industry for large area coatings. It is usually grown by atmospheric pressure chemical vapor deposition (APCVD) [79]. Through its growth, it attains a roughness in the range of σ_{RMS} = 40 nm, which allows light-scattering into the cell. The thickness of the TCO coated substrates used at PVcomB was optimized by the supplier to yield a sufficiently low sheet resistance (typically $R_{sheet} = 10 - 12\,\Omega/\square$). SnO_2:F has the disadvantages that when depositing the p-layer under high hydrogen dilutions, typically used for the deposition of μc-Si:H or μc-SiO_x:H, the contact properties deteriorate significantly [70] as mentioned above. Therefore, a p-layer system consisting of a-SiC:H has been used typically for this type of TCO.

2. *Aluminum doped zinc oxide (ZnO:Al)*, the material is usually deposited by sputtering [80–83]. The roughness is obtained through etching of the material typically with HCl for about 60s. Through the adjustment of the deposition conditions as well as the etching process, material with very large features (σ_{RMS} in the range of 120 nm) and good light-scattering properties in the long wavelength regions can be obtained or smaller features with correspondingly improved scattering in the shorter wavelength regions. Thus the current-matching of the sub cells can also be influenced through the adjustment of the ZnO:Al process. The highest stable efficiency reported for silicon thin film solar cells has been deposited on etched ZnO:Al, the device consisted of an a-Si:H/μc-Si:H/μc-Si:H triple junction [7] (compare table 2.1). However, as will be shown in section 6.3, a drawback of this type of TCO is the limitation of scattering the short wavelengths and the resulting comparably low top cell current for the a-Si:H/μc-Si:H solar cells. A solution of this problem could be adjustments to the etch process or alternative etchants such as HF [84] or in combination with textured glass. The electrical properties are comparable to SnO_2:F in the as-deposited case, but can be greatly improved via special post-deposition temperature treatments [85–87].

3. The last type of TCO used at the PVcomB is *boron doped zinc oxide (ZnO:B)*, the material is deposited by low pressure chemical vapor deposition (LPCVD) and is thus also referred to as LPCVD-ZnO:B. The growth of the material can be tuned in a way that very sharp features arise (σ_{RMS} = 70 nm), which are smaller in the

lateral dimension than ZnO:Al and thus have improved properties for the scattering of short wavelengths [88]. Accordingly, the highest efficiency reported for an a-Si:H/μc-Si:H tandem cell, has been deposited on this type of TCO. It has to be noted that this record cell also had a structured glass surface, and therewith a double structure which allows efficient scattering for both, top- and bottom cell. Short circuit current densities above 14 mA/cm^2 (>28 mA/cm^2 total current) and initial efficiencies well above 14% and above 12% after light soaking have been reported for this configuration [6]. The elctronic properties are typically worse than in the ZnO:Al due to a lower carrier density and thus the ideal thickness higher.

Intermediate Reflector Layer

The main limitation of the a-Si:H/μc-Si:H tandem cell is (as mentioned) typically the low current of the top cell. Here, the i-layer thickness cannot be increased arbitrarily without losing stability due to the Staebler-Wronski Effect. As mentioned above, the electrical quality of the bottom cell also suffers from an increased thickness, but only at much larger thicknesses. To increase the current in the top cell, intermediate reflector layers (IRL) can be used between the top and the bottom cell, which reflect part of the light back into the top cell. An IRL should have a low index of refraction and a low absorption coefficient. At the same time, the conductivity of the material has to be sufficiently high. In early publications ZnO:B or ZnO:Al has been suggested as material of choice for the intermediate reflector [23, 76]. The Zinc-Oxide intermediate reflector (ZIR) has the advantage that the material is very conductive and no negative influence on the fill factor of the device though an additional series resistance was measurable. However, due to this high conductivity, an additional laser scribe is necessary to prevent the short circuiting of the sub-cells via the ZIR. Furthermore, the deposition of the ZIR is usually not done in a PECVD system, but has to be done in another chamber, making the manufacturing process more complex. Therefore, a μc-SiO$_x$:H (see section 2.1.3) intermediate reflector (also referred to as Silicon Oxide Intermediate Reflector, SOIR) has thus been suggested as an alternative to the ZIR [9, 10, 89]. The material has the advantage that it is applicable to the PECVD process and the refractive index can be tuned to below 1.7 at a wavelength of 632 nm, which is even below the value for the ZIR which is at around 2.1 at this wavelength. μc-SiO$_x$:H also has a lower absorption coefficient than ZnO:Al or ZnO:B in the long wavelength regions (>700 nm)[77] and thus parasitic absorption can be lower in this wavelength region.

2.3. Plasma Enhanced Chemcial Vapor Deposition

Plasma enhanced chemical vapor deposition (PECVD) is a very common technique for the deposition of semi conductor thin films such as a-Si:H or μc-Si:H and its alloys. The fundamental principles of plasma discharges and material processing can be found in reference [28]. The deposition methods specific to thin-film silicon solar cells are for example described in references [26, 27, 35, 90]. Unlike in a thermal CVD deposition, the decomposition of the precursors is achieved via the use of a plasma that is usually realized through the application of a high-frequency field that is connected to two parallel plate electrodes, also referred to as a capacitively coupled plasma. Through the electric field, free electrons are accelerated and collide with precursor molecules. At sufficiently high energies molecules neutral radicals and ionized species are formed. The radicals diffuse to the surface and the film grows occurs through the sticking of radicals to the surface. Secondary reactions in the plasma can occur between the radicals and ions leading to further species. The radicals can move along the surface, desorb from the surface, or find their final place.

Due to their high energy and low mass, the electrons tend to diffuse towards the chamber surfaces and the susceptor, which are usually grounded. The positively charged ions remain inside the plasma bulk, which leads to a potential difference between plasma bulk and the surface. The potential difference causes ions to impinge onto the chamber and substrate surface. This ion bombardment can lead to a deterioration of the film quality. The quantitative description of the chemical reactions and the layer growth inside a PECVD reactor is still subject of current research as numerous possible reactions can occur. For SiH_4 discharges an overview is given by Perrin et al. [91].

For the deposition of a-Si:H or μc-Si:H, the typical precursor gas is SiH_4. It has a thermal decomposition temperature of 450°C, but due to the plasma decomposition much lower temperatures can be used. Besides the hydrogen of the SiH_4 molecules, high quality a-Si:H films are deposited under an additional hydrogen dilution with H_2/SiH_4 ratios in the range of 10/1 and more. The resulting film itself however, has only a hydrogen content of about 10-20 % [92]. Most of the hydrogen must therefore desorb from the surface. During the growth process, however, it improves the quality of the grown film significantly, such that the films density increases and the defect density decreases. If the hydrogen dilution is sufficiently high, crystalline growth occurs. The role of the hydrogen for the growth of a-Si:H and μc-Si:H and its alloys is being discussed widely in the literature [93–96]. The main points can be summarized as follows:

1. *Surface diffusion model:* The surface of the growing film is covered by hydrogen, which saturates dangling bonds on the the surface. The adatom diffusion length consequently increases and the film becomes denser [93].

2. *Preferential etching model:* The hydrogen etches preferentially the weak Si-Si bonds. A new precursor has the chance to form a stronger Si-Si bond and thereby increases the stability of the network [94]. This model is supported by data showing a decreasing deposition rate at increasing hydrogen dilution, however, it is found to be not a necessity for the microcrystalline growth [96].
3. *Hydrogen diffusion model* also known as *Chemical annealing model*: The hydrogen diffuses into the growth zone of the film, where it recombines with bonded hydrogen. The emerging H_2 effuses from the film. The nascent energy heats the film and restructures it. This model was first used to explain the so called layer-by-layer growth of μc-Si:H [95].

It should be noted that the hydrogen dilution used in the plasma deposition is not an indication for the hydrogen content of the layer [92] The deposition rate is typically of essential importance for the quality of the material. It is usually dominated by the deposition power, the total gas flow and the deposition pressure. The hydrogen dilution usually decreases the rate. Typical values for the deposition rate of the a-Si:H absorber layer at PVcomB are between 0.2 – 0.3 nm/s. For the growth of high quality μc-Si:H material, the rate can be higher (0.3 – 0.5 nm/s at PVcomB) without significant reduction in cell performance [97]. Here, the crystalline volume fraction plays the most important role for the quality of the solar cell as mentioned in section 2.1.2. Best cell results at PVcomB were made with material that has a Raman crystallinity of about 50 %, when annlyzed using the procedure described in section 3.2.2.

The influence of the deposition regime on the crystallinity and the quality of μc-Si:H has been studied intensively in the last years. The transition between a-Si:H and μc-Si:H can be obtained by the adequate variation of various deposition parameters, such as hydrogen dilution, RF power, pressure, electrode distance and temperature [97–99]. The investigation of the influence of these deposition parameters on the growth of μc-SiO_x:H and μc-SiC is another focus of this thesis, which is described in chapters 4 and 5. For the deposition of μc-Si:H absorber layers, the high power, high depletion regime can be used to obtain sufficiently high deposition rates at ideal crystallinities. Typically, the high power density is needed to dissociate enough atomic hydrogen to cover the surface. However, for high powers the ion energy increases, which deteriorates the film crystallinity and increases the defect density. To overcome this issue, high pressures are used, which decrease the high plasma potentials, that cause the ion bombardment. Increased pressures, however, reduce the amount of atomic hydrogen in the plasma again, which is needed for the crystallinity of the films due the hydrogen annihilation reaction [90]:

$$H + SiH_4 \longrightarrow H_2 + SiH_3 \tag{2.1}$$

This problem cannot be overcome by an increase of hydrogen dilution as long as enough atomic Si is available for the reaction to happen. However, through the adaption of the gas flows, the hydrogen annihilation can be circumvented if Silane is depleted. This deposition regime is therefore also referred to as high pressure depletion method [90]. Material deposited in this regime has typically very good properties for PV-application, which are a low grain boundary density and a strongly columnar growth, which results in a high spectral response in the red and infra-red region and good electronic properties [98].

3. Experimental Methods

The experimental part of the thesis is divided into the first section (3.1), which describes the fabrication of the samples, and the second section (3.2), which describes the methods used for the plasma diagnostics and the material solar cell characterizations.

3.1. Fabrication of the Layers and Solar Cells

In this section, the fabrication of the single layers and solar cells is described: The PECVD deposition method in general is described in section 3.1.1. Section 3.1.2 describes the substrate preparation, the silicon deposition by PECVD for single layers and solar cells, and the back contact deposition and laser structuring of the solar cells. The sample deposition and e-beam crystallization of the SiC samples is described in section 3.1.3. The deposition tools used were (a) the AKT-1600, an industrial-type PECVD tool with a high degree of automation and the ability to deposit on a large substrate size of up to $30 \times 30\ cm^2$ and (b) the VAAT-cluster tool, which is capable of very high substrate temperatures. The former was used for the deposition of μc-SiO_x:H and for the a-Si:H/μc-Si:H cell development; the latter was used for the experiments regarding the silicon carbide alloys.

3.1.1. The PECVD Process

As mentioned above, PECVD is the standard method for the deposition of a-Si:H and μc-Si:H layers. Detailed information about the method can be found for example in the book by Liebermann and Lichtenberg [28]. An illustration of a capacitively coupled parallel plate reactor, which was used for this work is shown in the next section.

In the PECVD process, the precursors mix by gas diffusion and dissociate through electron impact dissociation. The needed energy is provided externally by the RF power. Inside the plasma, energetically neutral radicals are formed as well as ionized species. Secondary processes induce gas phase chemical reactions, radical diffusion and film deposition. The number of possible reactions inside a plasma are numerous. An overview of the possible reactions in silane plasmas is given in [91].

For the deposition of the SiO_x alloys, CO_2 was used as oxygen precursor. The dissoci-

ation of CO_2 into CO and O is far more likely than the further dissociation of the CO radical, due to the difference in the binding energy. Thus, the incorporation of carbon into the layer through the admixture of CO_2 into the gas phase is very small. The growth kinetics for this alloy were described by Iftiquar et al. [100]. For the deposition of the SiC_x alloys, the precursor CH_4 was used. The dissociation of CH_4 is similar to the one of SiH_4, however, the CH_x species are relatively harder to dissociate and, thus, the incorporation of hydrogen into the layer is more pronounced [101]. The technique to deposit microcrystalline material has already been described in section 2.3. Doping was in all cases performed by the admixture of PH_3 for n- and TMB for p-type doping.

Besides the gas phase composition, the other deposition parameters also influence the film composition and its structural and optoelectronic properties. The parameters, which can be alternated to control the film growth, are presented in the following:

- The power density (P/A_{el}), which is the ratio of the RF power P and the electrode area A_{el}, controls the dissociation rate by determining the amount of electron impacts. It has thus a high influence on the film growth. Due to the differences in binding energy of the precursors, it also effects the partial density of species, which influences the film composition. It also has a strong influence on the plasma potential and therewith on the ion bombardment.
- The deposition pressure p controls the mean free path length of the particles. It also influences the plasma potential and therewith ion bombardment.
- With increasing substrate temperature T_s, the desorption from the film and the adatom diffusion lengths on the surface increases. At high temperatures, it can decrease the crystallinity due to increased hydrogen desorption from the surface [93].
- The total gas flow f_{tot} determines the supply of radicals for the film growth and therewith the upper limit for the deposition rate.
- The plasma excitation frequency has a strong influence on the plasma potential and plasma chemistry. It determines the width of the sheaths and the ion bombardment for a given ion flux. In this work, the frequency was fixed at 13.56 MHz for all depositions, which is an industrial standard frequency. Also higher frequencies, which are usually referred to as very-high frequencies (VHF), are being used for the deposition of a-Si:H and μc-Si:H (see for example [102]). In VHF plasmas, the ion bombardment is lower.
- A very useful indirect parameter is the residence time t_{res}, which is the average time, the molecules remain inside the reactor. Neglecting the heating effect of the plasma,

the residence time can be estimated according to

$$t_{res} \propto \frac{A_{el} d_{el} p}{f_{tot} p_0} \tag{3.1}$$

[103]where d_{el} is the distance between the electrode and the grounded susceptor, p the deposition pressure, p_0 the ambient pressure and f_{tot} the total gas flow. The residence time can thus be controlled by either adjusting the pressure, the electrode gap or the total gas flow. The residence time controls the gas utilization and therewith also the deposition rate. In the high power depletion regime (see section 2.3) long residence times are needed. The combination of low hydrogen dilutions and long residence times can lead to plasma polymerization (dusty plasmas).

Deposition Tools

As the both deposition tools AKT1600 and VAAT are in many aspects similar, the following description is to a large extent valid for both tools. The plasma excitation frequency used for all depositions was 13.56 MHz, which is an industrial standard frequency.

A cross section of an AKT1600 deposition chamber and the *in-situ* diagnostics used in the AKT1600 is given in Fig. 3.1. The AKT1600 has three deposition chambers (A, B and D), which are each used for different layers to avoid cross contamination and to increase the throughput. The top electrode is connected to an RF generator and functions also as the gas inlet (shower head design). The susceptor on which the substrate is placed functions as the counter electrode, which is grounded. In between the top electrode and the RF generator, a compensating network (matchbox) is inserted. The electrode has an area of 2500 cm^2 and the susceptor an area of 1600 cm^2. The susceptor can be moved vertically by means of an elevator for the transport of the substrates as well as to adjust the electrode distance and the plasma reactor volume to the desired size. The reactor volume is another parameter influencing the film growth as mentioned in section 3.1.1. The pressure is set using a valve system in between the chamber and the exhaust pump.

Typical substrate temperatures, which are achieved through heaters placed underneath the susceptor, for the deposition of a-Si:H in a PECVD reactor are around 185 – 220°C. Higher temperatures can be used in principle. The precursor gas supply is also indicated in Fig. 3.1. Besides the mentioned SiH_4 and H_2 for the deposition of a-Si:H and μc-Si:H, there are the dopant sources PH_3 and TMB; the oxygen and carbon alloyed wide band gap materials are deposited through an admixture of CO_2 and CH_4 into the gas phase. Nitrogen trifluoride (NF_3) together with Argon is used for the cleaning of the chambers by the use of an ion assisted etch plasma. The base pressure is below 10^{-2} kPa and typical deposition pressures are between 0.1 – 2 kPa.

,

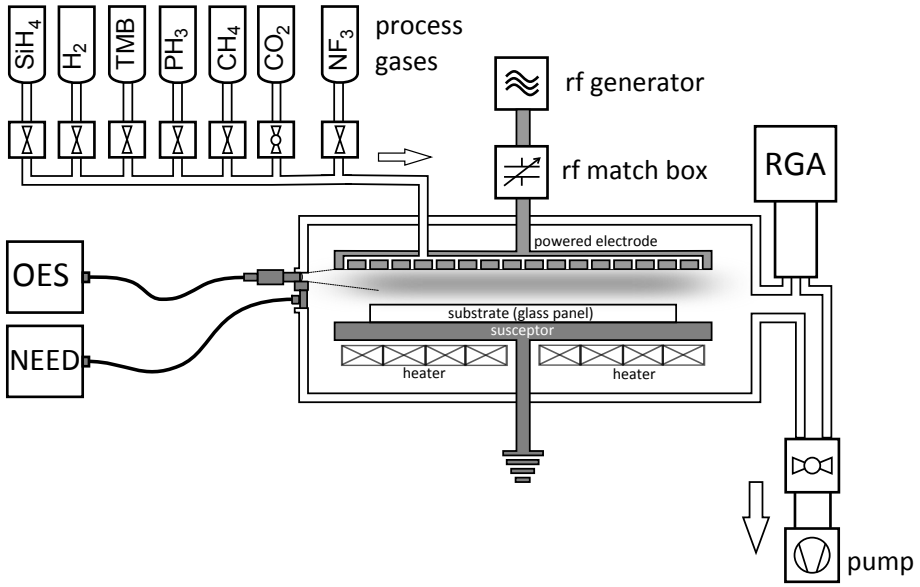

Figure 3.1.: Schematic view of a PECVD deposition chamber with gas supply and in situ diagnostic tools.

Furthermore depicted in Fig. 3.1 are the *in situ* plasma diagnostic tools used in the AKT, namely the optical emission spectroscope (OES) and the residual gas analysis (RGA) by means of quadrupole mass spectroscopy. The *in situ* plasma diagnostic tools are described in section 3.2.1.

The PECVD chamber of the VAAT Cluster Tool (Von Ardenne Anlagen Technik GmbH) has in principle a very similar structure as the chambers of the AKT1600. The main differences are as follows:

- The electrode is circular not rectangular with a diameter of about 200 mm.
- The chamber is designed specifically for high temperature applications. The heater is thus integrated directly into the susceptor. For the depositions, also a Si-wafer was used as substrate holder, which is placed directly onto the heater during the deposition.
- The vacuum is generated by turbo pumps and the base pressure is below 10^{-5} kPa.

3.1.2. Single layer and Solar Cell Depositions at the AKT-1600

Glass ans glass/TCO Substrates

All single layers and solar cells fabricated in the AKT1600 in the course of this thesis were deposited on thick industrial type low iron float glass, generally with a thickness of 3.2 mm. All process steps up to the measuring of the cells under the sun simulator were conducted on 300 x 300 mm^2 panels. For the solar cells, the glass substrates were coated with a TCO as the front electrode. In these cases, the glass substrates were pre coated with the TCO by external partners. Available were ANS12, a SnO_2:F TCO deposited by atmospheric pressure chemical vapor deposition (APCVD), DC-magnetron sputtered ZnO:Al and ZnO:B deposited by LPCVD. Before the deposition of the silicon layers, the glass substrates and TCOs were cleaned using a detergent (not for ZnO TCOs) and deionized water. The APCVD SnO_2:F as well as the LPCVD ZnO:B TCOs have a native roughness, the sputtered ZnO:Al TCO was etched after cleansing and prior to the cell deposition with HCl (0.5%) for 60 to 90 seconds at room temperature, as explained in section 2.2.2. For SiC depositions in the VAAT cluster tool, 0.7 mm Corning glass (type 7059) was used in all cases.

Baseline process for a-Si:H/μc-Si:H tandem cell deposition at the AKT1600

All μc-SiO_x:H layers and all devices were deposited in the AKT1600 tool. In the following, the solar cell process is being described. The depositions of the single layers were performed accordingly. A schematic view of all three deposition chambers, the load lock with the cassette for six substrates, and the transfer chamber with the robot is given in Fig. 3.2.

In the baseline process at the PVcomB, the substrate temperatures for the p- and amorphous i-layers were between 190 - 220 °C due to the fact that these two layer types were always deposited in the same chamber A. All n-layers were deposited in chamber B at a substrate temperature of 185°C and the μc-Si:H i-layer was deposited in chamber D at 190°C. Prior to the solar cell depositions, the chambers were thoroughly cleaned by Ar/NF_3 plasma etching to avoid cross contamination. After the cleaning, the chambers were conditioned (seasoned) to assure reproducibility. Due the partial etching of the material on the chamber walls, that always occurs during the PECVD process to some extent, the plasma and the film growth are affected by the material, which is on the walls prior to the actual deposition. Therefore, - depending on the successive layer - a doped or intrinsic a-Si:H or μc-Si:H layer was deposited in the chamber before the actual deposition without the substrate. After the substrate is transferred into the chamber, the cell deposition started with the p-layer in chamber A after a heating step of ten minutes.

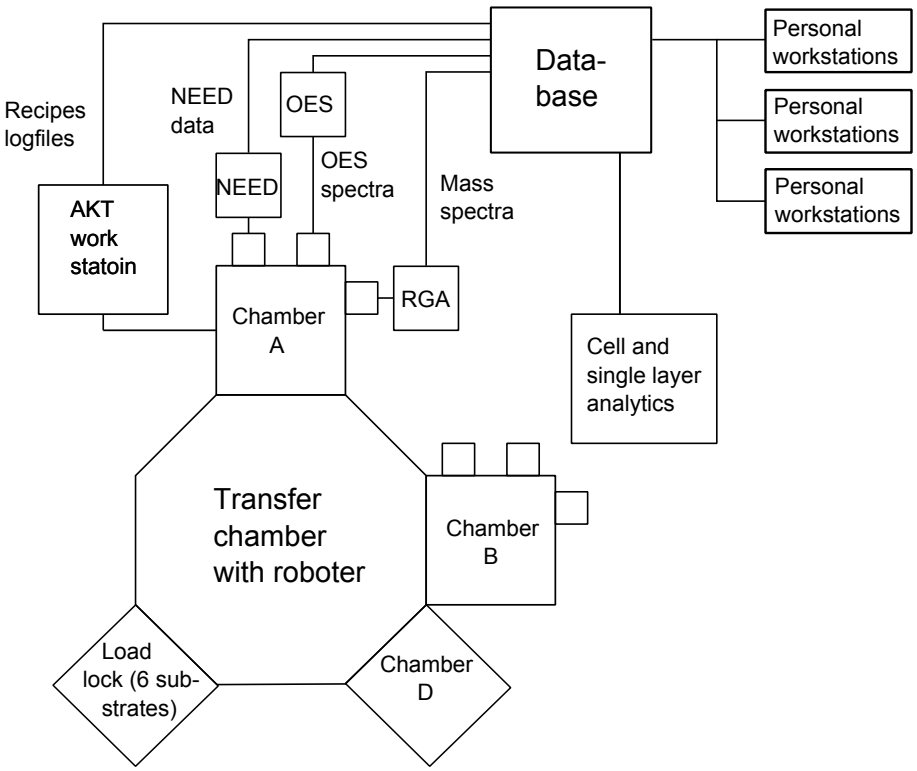

Figure 3.2.: Schematic view of the 3-chamber AKT1600 deposition tool as well as the *in-situ* diagnostic tools and the database infrastructure.

The standard sequencing for the a-Si:H/μc-Si:H tandem cell baseline is depicted in 3.1. As mentioned, the top cell p- and i-layer were deposited in the same chamber A. To avoid cross contamination, a long cleaning step has to be done in between the two depositions, during which the substrate was moved to another chamber. Both n-layers, including all intermediate reflector layers were deposited in chamber B. No cleaning steps were used in between top- and bottom-cell n-layer. However, a μc-SiO_x:H seasoning for the first deposition (typically first run in the morning) was done. The bottom cell i-layer was deposited in chamber D. After each bottom cell i-layer deposition (typically 2 μm) the chamber was cleaned to avoid the spalling of material from the chamber walls.

Fig. 3.2 also shows the database infrastructure at the PVcomB. Here, all the data is collected from the log files of the AKT1600, the in situ plasma diagnostics and the data from the sample characterization. This allows a comprehensive process monitoring and enables a fast analysis of all aspects (tool control, plasma properties and sample characteristics) for a conducted experiment.

Table 3.1.: Standard sequence for a-Si:H/μc-Si:H tandem cells. For the pre and post recipes, seas implies chamber conditioning (seasoning) and clean implies the NF_3 plasma etching of the chamber walls and t(s) represents the total step time.

Step	Chamber	Pre	t (s)	Main recipe	t (s)	Post	t (s)
1	A	Seas	280	Top cell p-layer	1000	Clean + seas	650
2	A			Top cell i-layer	1600		
3	B			Top cell n-layer	600		
4	A	Seas	280	Bottom cell p-layer	500		
5	D			Bottom cell i-layer	4500	Clean + seas	900
6	B			Bottom cell n-layer	400		

Laser Structuring, Back Contact Deposition Annealing

At PVcomB, both single cells as well as modules are being fabricated. In both cases, laser scribing is used to structure the cells. The process and design rules are being described for example by Gupta [104] or Repmann [99]. A schematic illustration is shown in Fig. 3.3. In this method, three steps are used to interconnect the solar cells: in the first step (P1) the TCO front contact is insulated with a laser of 355 nm wavelength. After the deposition of the active layers, the silicon stack is then separated by a laser of 532 nm wavelength (P2), which does not affect the front TCO. After the deposition of the back contact, the last separation step (P3) is conducted again with a laser of 532 nm wavelength. For the fabrication of single solar cells, a slightly alternated design can be used since the TCO does not have to be separated: After the deposition of the solar cell stack, several P2 scribes are placed close to each other to form a low ohmic contact to the front TCO. After the deposition of the back contact, single cells being cut with the P3 step of 1 x 1 cm^2 size. For the layout used at the PVcomB, this results in 180 separate cells on a 30 x 30 cm^2 panel, as can be seen in Fig. 3.4.

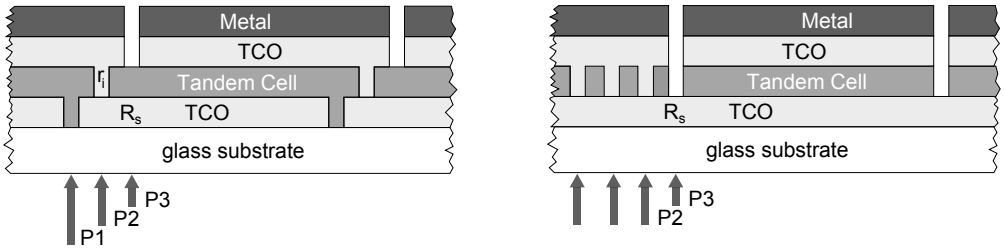

Figure 3.3.: Schematically shown are the cross sections for the laser scribing designs for the module (left) and for the cell design (right).

The back contact consists of 80 nm ZnO:Al and 200 nm Ag. The ZnO:Al improves the reflectivity of the back contact and reduces plasmonic losses at the nano-rough Ag surface [105]. The back contact is deposited on an automatic in line sputter tool from the company Leybold Optics. After the deposition of the back contact and the final (P3) laser step, the panels were annealed for 50 minutes at a temperature of 160*C*, which improves mainly the back contact. After the annealing step, the panels were cut into coupons of $100 \times 100\,mm^2$ size. The standard nomenclature for the coupons and the cells is depicted in Fig. 3.4.

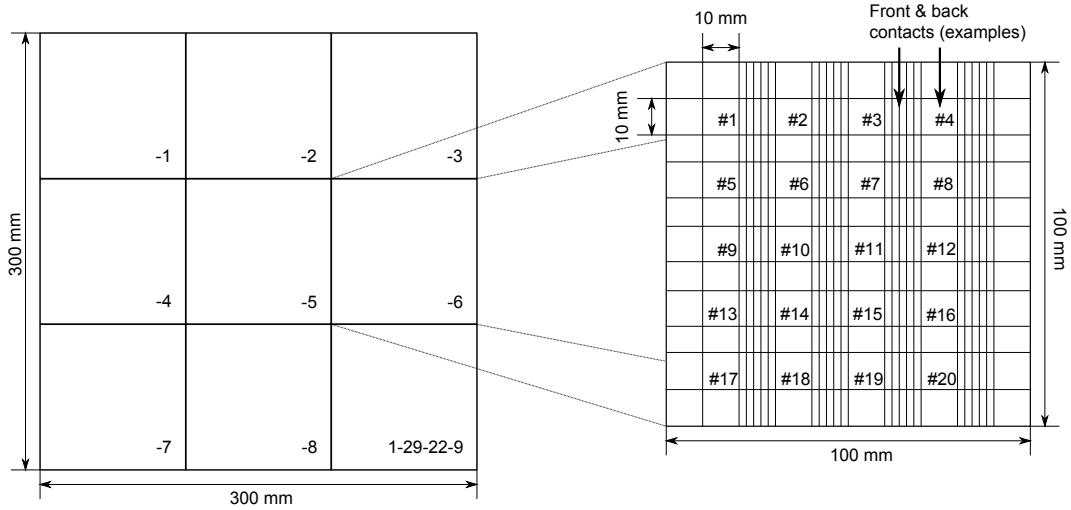

Figure 3.4.: (Left) Standard nomenclature for a $300 \times 300\,mm^2$ panel and (right)the standard cell-contacting scheme and -nomenclature of a $100 \times 100\,mm^2$ coupon (both views are from the deposition side).

3.1.3. Deposition at the VAAT and E-Beam Crystallization

The depositions at the VAAT were performed analogue to the depositions at the AKT1600. A difference was, as mentioned, that the samples were put on a substrate holder, which consisted of a Si wafer. Prior to the deposition, the samples were heated under H_2 flow depending on the deposition temperature between 5 to 10 minutes. All depositions on the VAAT were performed on $10 \times 10\,mm^2$, 0.7 mm thick Corning 7059 substrates, which were cleansed prior to the depositions.

The crystallization of the samples, were performed using the electron beam (e-beam) set up, which was conventionally used for the crystallization of the silicon absorbers for the poly-Si cells (compare section 2.2.1). The set up design and functioning is described for example in references [106, 107]. By choosing the appropriate energy flux and movement speed, silicon grains with sizes up to the cm range can be fabricated [18]. An illustration

of the assembly is depicted in Fig. 3.5. Therein, the sample is placed underneath a tungsten wire, which serves as the cathode and electron source. The pierce electrode is used to focus the electron beam onto the sample. The wire is heated by a constant current I_k. The electrons are accelerated towards the anode by an acceleration voltage V_a, which was typically between 5 – 15 kV. To allow coupling of the e-beam with the sample on glass, the edges of the sample are prepared with a conducting graphite solution. The crystallization was performed at a pressure of below $2 \cdot 10^{-}3\,Pa$, which is necessary for a stable electron beam. Through the e-beam, high energy densities between 0.3 and $0.6\,mJ/mm^2$ were injected into the material. The material melts and then crystallizes upon cooling. For the SiC crystallization experiments, which are described in section 5.3, the samples were annealed for 4h at 600°C prior to the crystallization to reduce the hydrogen content of the layers, which hinders a homogeneous crystallization. Another temperature step directly before the crystallization process was used to heat the samples to a temperature of 450 – 500°C. The e-beam movement speed of the e-beam holder were set to 12 mm/s.

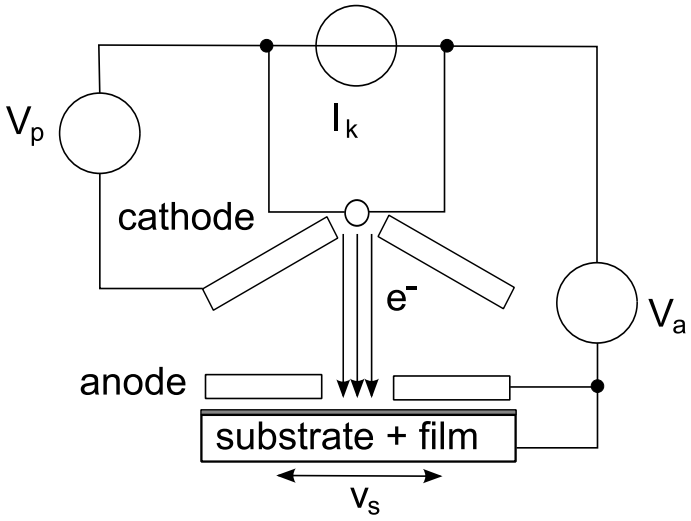

Figure 3.5.: Illustration of the assembly of the electron beam crystallization set up.

3.2. Characterization

In this section the different characterization methods used in this thesis are being described. They can be divided into the sections about the plasma diagnostics (section 3.2.1), the characterization methods for the single layers (section 3.2.2) and the methods for the characterization of the solar cells (section 3.2.3). More information about thin film silicon material and solar cell characterization are given for example in the books by Shah [27] or Schropp et Zeman [26].

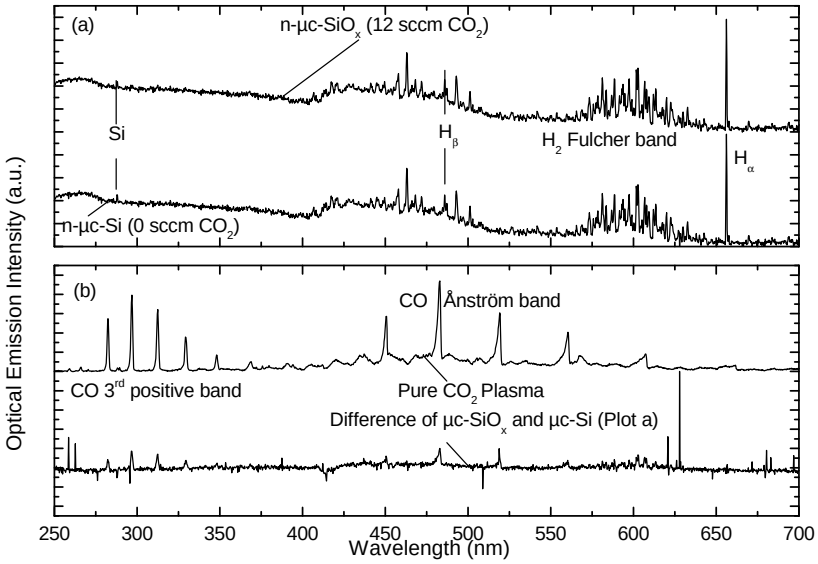

Figure 3.6.: Optical emission spectra (OES) of (a) a μc-Si:H and μc-SiO$_x$:H plasma and (b) a pure CO_2 plasma. Also plotted in (b) is the difference between the two spectra seen in (a).

3.2.1. In Situ Plasma Diagnostics

For the plasma diagnostics, two techniques were used namely optical emission spectroscopy (OES) and residual gas analysis (RGA).

Optical Emission Spectroscopy

OES measures the photons emitted during the relaxation of electrons in excited molecules in the plasma. By evaluating the peak intensities at the for the species characteristic emission lines, one can deduce qualitative conclusions regarding the plasma chemistry. For example, the transition between amorphous and microcrystalline growth can be monitored by the ratio of silicon related to hydrogen emissions (see e.g. [90]). This technique is also used in chapter 4.3 for the investigation of the transition to microcrystalline growth in μc-SiO$_x$:H. Exemplary spectra of plasmas for n-doped μc-SiO$_x$:H and μc-Si:H are shown in the top part of Fig. 3.6. Several characteristic peaks are indicated: atomic silicon *Si** at a wavelength of 288 nm, atomic hydrogen H_α at a wavelength of 656 nm and H_β at 486 nm and the H_2 Fulcher band.

For comparison, also the spectrum of a pure CO_2 plasma is given in the bottom part of Fig. 3.6 together with the difference of the two afore mentioned spectra. From the residual of both plasmas, it can be seen that the admixture of CO_2 has no significant change on the

intensities of *Si**, H_α and H_β in this example. Only weak signals from the Ånström and the 3rd positive CO band can be observed.

Residual Gas Analysis

From mass spectroscopy using a quadruple residual gas analyzer (RGA), which is mounted near the gas exhaust as depicted in Fig. 3.1, the process gas depletion D can be measured with $D = 1 - n/n_0$, where n_0 is the density of the source gas measured before the start of the plasma and n the density during the deposition. The calculated process gas depletion values for a μc-SiO_x:H plasma for example are depicted in Fig. 4.3 (in section 4.3).

The silane density was determined using the mass number $m = 30$, CO_2 using $m = 44$, and CO at $m = 28$. Since $m = 28$ is partly superimposed by the SiH_4 signal, the quantity was determined from the difference of the spectra of a μc-Si:H plasma with and without CO_2 admixture. From the ratio of CO_2 and CO, one can estimate the oxygen content in the film, under the assumptions of a uniform deposition within the chamber. The dissociation of CO is negligible due to its high dissociation energy. Thus, the O / Si ratio can be calculated as:

$$[O/Si]_{layer} = \left(\frac{D_{CO_2}}{D_{SiH_4}}\right) \cdot \left(\frac{F_{CO_2}}{F_{SiH_4}}\right) \tag{3.2}$$

where F_{CO_2} and F_{SiH_4} are the CO_2 and SiH_4 flow rates.

3.2.2. Single Layer Characterization

To characterize the material used in thin film silicon solar cells, it is useful to deposit the material as a single layer onto a substrate. The most relevant information for the optimization of the device are the film thickness as well as the optical-, electrical and structural characteristics. The difficulty extracting this information from the device itself, arises from the complex layer stack (with important layers of only a few nanometer thickness) as well as the fact that usually rough substrates are being used. A drawback of this approach is that the film properties depend on film thickness and substrate type. Thus, all absolute values have to be taken with care, however, there were no hints in the presented data that the *trends* differ on a single layer and within the device.

Film Thickness

The most direct way to measure the film thickness is by microscopic methods such as scanning- or transmission-electron microscopy (SEM or TEM). The disadvantage of these methods is the high complexity due the fact they are conducted under vacuum and de-

mand further complex preparation steps, which make these methods very time consuming and thus inapplicable for a large amount of samples. Also, the samples are usually unusable after the experiment (destructive measurements). Therefore, these methods were only conducted on an irregular basis. Some TEM results were already shown in section 2.1.3.

A common and more practical technique to determine the film thickness is *profilometry*. In this method a needle is driven over an edge and thus the film thickness is determined. At PVcomB a profilometer of the type Ambios XP-2 was used. A disadvantage of this method is again the destruction of the sample to obtain a clear edge. Furthermore, the method to produce the edge can be rather difficult. For the amorphous layers that adhere poorly to the substrate, the material can be partly removed simply by sticking a scotch tape onto the layer and pulling it off. For microcrystalline layers however, usually an adhesion layer consisting of SiN_x is deposited onto the substrate prior to the film deposition making the simple pull-off technique impossible. Other methods for the edge preparation such as chemical etching or laser ablation were tested but showed no sufficient accuracy.

The most common and fastest way to determine the thickness of the layers is by means of fitting optical measurements (such as transmission and reflection or spectral ellipsometry spectra) which will be described in the following section in more detail.

Optical Measurements

Two set-ups for optical measurements were used: (1) A Perkin Elmer photo spectrometer type Lambda 1050 with a deuterium and a halogen light source and a monochromator allowing measurements from 170 to 3300 nm wavelength. Measurements were done using an integrating sphere and a photomultiplier tube (for 250-860 nm) and a InGaAs detector (for 860-2500 nm). (2) A mapping table using also a deuterium and halogen lamp and an Avantes spectrometer was used. Due to the higher accuracy, the former was used for the determination of the thickness and the optical properties and the optical constants, refractive index n and absorption coefficient α. For the determination of the layer homogeneity, the mapping table was used.

The analysis of the spectra was done with the software tool SCOUT (W. Theiss Hard- and Software). This tool calculates the transmission and reflection spectra of a model layer stack using the transfer matrix algorithm [108]. The calculated spectra are then fitted to the experimentally obtained ones using the downhill simplex method. In this procedure the layer thicknesses as well as the optical properties of the material are parameters, which can be varied to reduce the difference of measured to calculated spectra. The model used to describe the dispersion function of the layers is the Tauc-Lorentz (TL)

model, which is advantageous for the fitting of amorphous materials [109] and is also suggested in literature for μc-SiO$_x$:H [10]. This model uses the expression for a Lorentz oscillator multiplied with the Tauc formular yielding an asymmetric expression for the imaginary part ϵ_2 of the dielectric function

$$\begin{aligned} \epsilon_2(E) = 2nk &= \frac{AE_0C(E-E_g)^2}{(E^2-E_0^2)^2+C^2E^2}\cdot\frac{1}{E}, \quad E > E_g, \\ &= 0, \qquad\qquad\qquad\qquad\quad E \leq E_g. \end{aligned} \tag{3.3}$$

Unlike in the (symmetric) expression for the Lorentz oscillator, where absorption is assumed to converge to zero for large wavelength, in the Tauc-Lorentz expression, the extinction is zero below a discrete gap energy E_g. It should be noted, that for spectra partially dominated by indirect absorption as it is the case in crystalline silicon between 1.1 and 3.3 eV the agreement between model and experiment is usually poor, mostly due to the sharp feature at the direct band gap. A comparison between a highly crystalline μc-Si:H n-layer (Raman crystallinity, F_c = *0.7*) and a μc-SiO$_x$:H layer (F_c = *0.3*) is given in Fig. 3.7. The expression for the real part of the dielectric function is obtained by the Kramers-Kronig relation. In total, Tauc-Lorentz model uses four parameters: the mentioned Tauc-gap E_g, below which absorption is assumed to be zero; oscillator resonance frequency E_0, oscillator strength A and oscillator damping C. Typically in this thesis, the layer thickness was used as another free parameter, which however increases the necessity for appropriate initial values. The value for $\epsilon_0 0$ (real part of dielectric function) at infinite wavelength, was kept constant at 1.

For layers fabricated in this thesis, the TL model yielded very good fits for layers with low and medium crystallinity (up to a value for F_c of 50%, see next section for a definition of F_c). For layers with higher crystallinity, fit quality decreased, which can be explained by the increasing contribution of indirect absorption of the c-Si phase, which (as mentioned) can not be accounted for with the TL model. The calculated thicknesses were very reproducible with run to run differences of below 1%.

As μc-SiO$_x$:H is a two phase system consisting of μc-Si:H and a-SiO$_x$:H, also models that account for multiple phases such as the Bruggemann effective medium approximation (BEMA) are applicable [110]. BEMA was for example used by Losurdo et al. [111] and Ram et al. [112] to model pure μc-Si:H. Attempts have been made in the course of this thesis to model μc-SiO$_x$:H using BEMA with the TL model for the a-SiO$_x$:H phase and the data suggested in [112] for the μc-Si:H phase and the void fraction. Due to the increase in parameters (3 additional parameters: Void-, small- and large-grain fraction), the determinacy of the fit decreased and no robust solutions were found. However, this approach is thought to be able to give good information about film stoichiometry and structure once calibrated to information about the crystallinity and the stoichiometry ob-

tained from other measurements such as secondary ion mass spectroscopy or TEM.

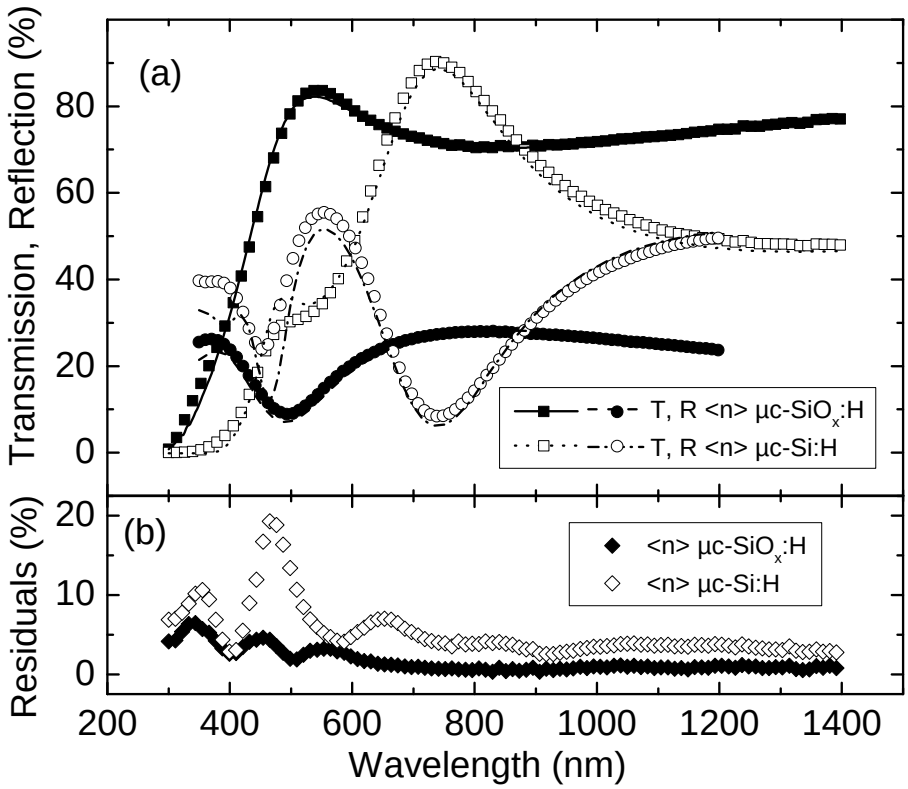

Figure 3.7.: (a) Transmission and reflection spectra as a function of wavelength for μc-SiO$_x$:H (■ and ●respectively) and μc-Si:H (open symbols) single layers deposited on glass and the corresponding fits (lines), (b) Sum of the residuals between fits of transmission and reflection spectra for μc-SiO$_x$:H (♦) and μc-Si:H (◇).

Fig. 3.7 shows as an example of the transmission (T) and reflection (R) spectra of μc-SiO$_x$:H and μc-Si:H layers on 3.2 mm glass and the corresponding fits. The residuals are calculated as the sum of the absolute values of the deviations of the calculated and experimentally measured spectra for each material. It can be seen, that the deviation for the layer without oxygen is greater than the one with oxygen, which is thought to be mainly due to the difference in crystallinity and the resulting higher fraction of indirect absorption.

In Fig. 3.8 calculated absorption spectra can be seen for layers deposited at various CO_2/SiH_4 ratios and resulting varying optical and structural properties. The calculation was performed as indicated on the one hand using Tauc-Lorentz model and on the other hand using Lambert-Beer's law similar to a method described in [113], which is a popular method for a fast determination of the absorption coefficient. The quantity E_{04}, which is defined as the photon energy, where the absorption coefficient is 10^4 cm^{-1} is also indicated. E_{04} is a robust measure for the optical band gap [114]. For intrinsic a-Si:H, E_{04} is

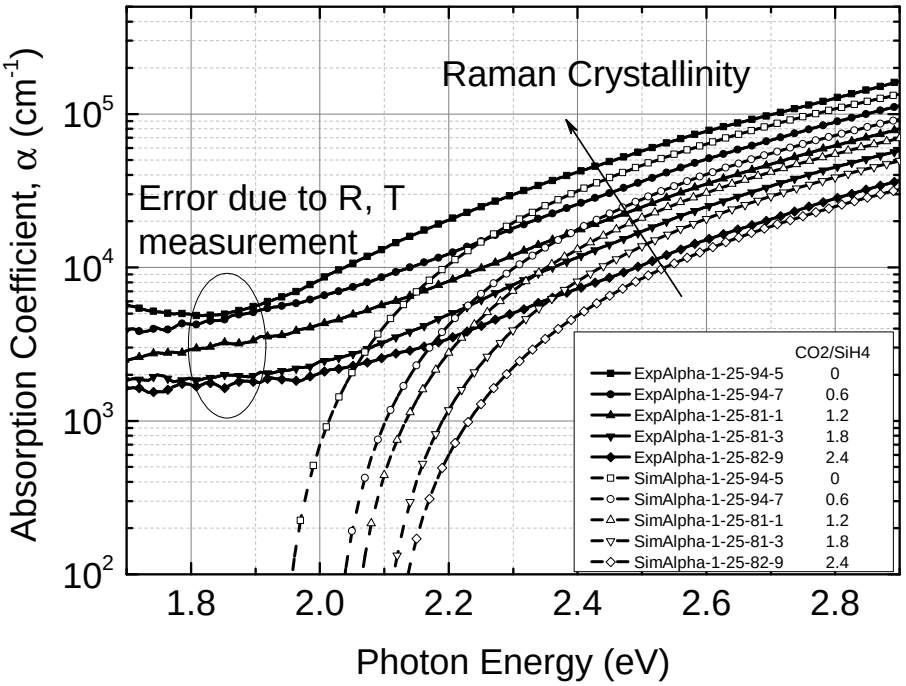

Figure 3.8.: Absorption coefficients as a function of photon energy for μc-SiO_x:H layers deposited with varying CO_2/SiH_4 ratio in the gas phase as indicated, calculated by Lambert-Beer's law (closed symbols) and with TL model (open symbols). Deposition parameters are given in chapter 6.

usually 0.2 eV higher than Tauc's gap E_g [115]. Presumably, due to the contribution of indirect absorption, the spread was found to increase when going from purely amorphous to microcrystalline films, where typical values for intrinsic material yielded values in the range of $E_g = 1.6$ eV and $E_{04} = 2.0$ eV. The mobility gap (see chapter 2.1 for the definition), which is usually closer to Tauc's gap in amorphous silicon, is for microcrystalline silicon not unambiguously reported in literature, with values ranging between 1.19 to 1.59 eV [116–118]. Due to these ambiguities the value E_{04} is therefore preferably to E_g used as a measure for the transparency of the layer.

Electrical Measurements

The standard approach for the electrical characterizations of thin film semi conductor layers on glass substrates is to deposit coplanar metal contacts with varying distances onto sufficiently thick sample (to avoid influence of surface currents) [119]. Due to its high work function and low diffusion into silicon, Ag-contacts were used. Neglecting

current crowding and stray fields, the conductivity σ of the sample can be determined as:

$$\sigma = \frac{j}{E} = \frac{I}{V} \cdot \frac{d}{t \cdot l} \tag{3.4}$$

With j being the current density, E the electric field stregth, I the current, d and l the distance between and the length of the contact stripes, respectively, and t the thickness of the layer. The Ag-contacts were deposited by thermal evaporation through a mask. The resulting contact stripes had a length l of 6 mm and distances d between 0.16 and 0.84 mm. The varying distances were applied to calculate the contact resistance by the transmission line method described in [119]. Examples for this method are given in Fig. 3.9. The measurements were performed in the dark and under vacuum to avoid photogeneration and leakage currents using a Keithley 6517B high-resistivity meter. Prior to the electrical measurements, the samples were annealed at 160°C for 50 minutes under air to reduce the influence of humidity. The μc-SiO$_x$:H samples showed also a greatly enhanced conductivity after annealing, which is described in section 4.5. Due to simplicity, some measurements were performed under air using a hand held contact system connected to the high-resistivity meter that was calibrated before to the above mentioned procedure.

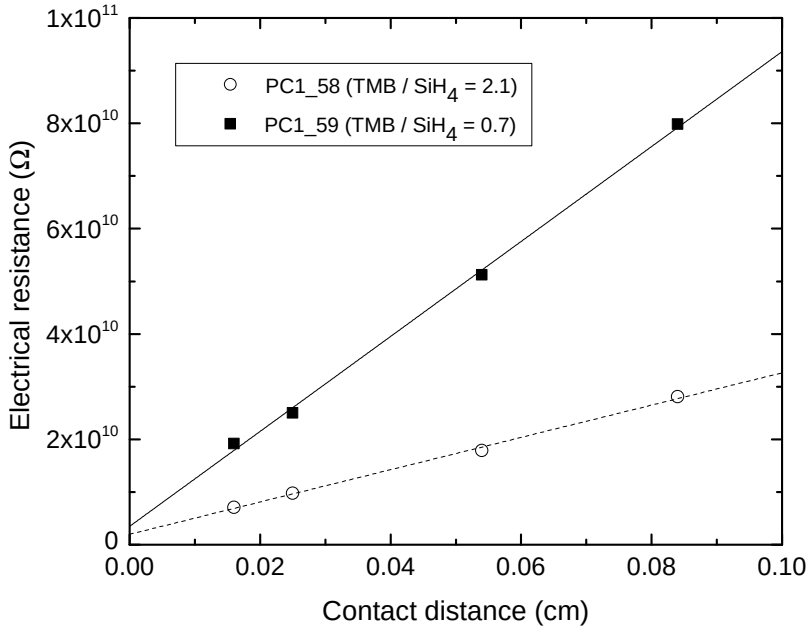

Figure 3.9.: Electrical resistance R as a function of contact distance d for samples and the corresponding linear fits from which the contact resistance could be determined. As examples, two <p> a-SiC:H samples deposited with different TMB flows at the VAAT were used.

Under the assumption of isotropy, one can calculate the distance between the Fermi-level and the valence band E_f - E_v for p- and the Fermi-level and conduction band E_c - E_f for n-type material, respectively, from the activation energy of the temperature dependence of σ, since:

$$\sigma = e \cdot \left(n\mu_e + p\mu_p \right) \tag{3.5}$$

with the charge carrier densities n (electrons) and p (holes) and their respective mobilities μ_e and μ_p. The charge carrier densities are exponentially dependent on the position of the Fermi-level:

$$p = N_v \cdot exp\left(\frac{E_f - E_v}{kT} \right) \qquad \text{and} \qquad n = N_c \cdot exp\left(\frac{E_c - E_f}{kT} \right) \tag{3.6}$$

where N_v and N_c are the densities of states at the valence and conduction band mobility edges, respectively. With equaton 3.5 and 3.6 one can deduce an approximation for the temperature dependence and the position of the Fermi level (here exemplarily given for n-type material):

$$\sigma(T) = \sigma_0 \cdot exp\left(-\frac{E_a}{kT} \right) = \sigma_0 \cdot exp\left(-\frac{E_c - E_f}{kT} \right) \tag{3.7}$$

The temperature dependence of μc-Si:H was found to exhibit a bending (i.e. not following eq. 3.7) in the temperature range between 5-300K, which can be explained by the anisotropy of the material and the existence of grain boundaries [20].

For μc-SiO_x:H optimized for intermediate reflector application, the lateral (or in-plane) conductivity can be several orders of magnitude lower than the transversal (or top-to-bottom) conductivity due to the columnar growth of the μc-Si:H crystals within the a-SiO_x:H matrix [15]. To measure the transversal conductivity, the layers were deposited on non textured ZnO:Al ($t \approx= 1$ μm, $R_{sheet} \approx= 5Ohm$). For contacting, the laser design for the cells depicted in Fig. 3.3 and Fig. 3.4 was used. In such a device the transversal conductivity of SiO_x:H can be evaluated for layers, where $R_{SiO_x:H} >> R_{ZnO:Al}$. If the contribution of the ZnO:Al to the measured resistance should remain below 1%, layers of 200 nm with conductivites of up to $4 \cdot 10^{-8}$ S/cm can be measured in this design. Due to this limited range, difficulties with the P2 laser cut arising from the low absorption coefficient of the SiO_x:H layers and uncertainties of the contribution of current crowding, a more convenient method was found to lie in the investigation of the series resistance determined from illuminated I-V (R_{oc}) of the a-Si:H/μc-Si:H tandem cell as described in the following section 3.2.3.

Raman Spectroscopy

Structural investigations were performed mainly using Raman spectroscopy. Raman spectroscopy is the investigation of inelastic scattering of light on matter (Raman scattering). Part of the incoming photon flux interacts with the phonons of the material and its energy shifts either to higher (Stokes shift) or lower (anti Stokes shift) energies. In the following, only the stokes shift is used. From the resulting *Raman*-spectrum, the phonon density of states can be deduced. From this, quantitative results about the crystalline volume fraction can be drawn due to the differences in the phonon modes of amorphous and crystalline material. An overview of distinct modes in the spectrum of amorphous and microcrystalline silicon and silicon-alloys is given in table 3.2:

For the quantitative analysis of the spectra, a procedure similar to the one presented by Smit et al. was used [124]. In this approach, the Raman spectrum is separated into an amorphous and a crystalline part by subtraction of an amorphous reference spectrum. Then, the ratio of both parts is calculated to obtain the *Raman crystallinity*, F_c as shown in Fig. 3.10. To account for differences in the Raman cross sections regarding phonon excitation between c-Si and a-Si:H, a correction factor y has to be used to determine the exact crystalline volume fraction [128]:

$$F_c = \frac{I_c}{I_a + y \cdot I_c} \tag{3.8}$$

y is known to depend on the grain size and varies between 0.1 and 1 [129, 130]. For the presented work, the Raman spectrum was analyzed using 6 Gaussians and a linear background of which 4 describe the amorphous fraction and the remaining two describe the crystalline (compare table 3.2). The position and the width of the 4 a-Si:H Gaussians were kept at fixed values, which were determined prior from a reference spectrum measured at an intrinsic a-Si:H sample deposited at the same conditions as the top cell i-layer. The cross section correction factor was kept at unity for simplicity and a lack of better knowledge. Thus, the given values for F_c have to be seen as a lower limit for the crystalline volume fraction. The crystalline contribution to the intensity I_c was calculated from the sum of the intensities of Gaussian peaks near 510 and 520 cm^{-1}. While the latter is well known to be the TO mode of c-Si, the former represents the contribution of the TO mode of crystallites of smaller size, as calculations have suggested [131]. For the amorphous contribution to the spectrum, the intensity of the peak at 480 cm^{-1} was used, which is the TO mode of a-Si:H.

Fig. 3.10 shows the measured Raman spectra of three samples deposited with varying CO_2/SiH_4 ratio (as indicated) and resulting differences in Raman crystallinity. To illustrate the described approach all six fitted Gaussians and the fitted linear background are depicted as hairlines for the sample with the lowest F_c. For the sample with the highest

Table 3.2.: Phonon modes of amorphous and microcrystalline silicon and silicon-alloys in the range of 200 to 2500 cm^{-1}. LA, LO, TO and TA denote longitudinal acoustic and optic modes and transversal acoustic and optic modes, respectively.

Wavenumber (cm^{-1})	Assignment	Wavenumber (cm^{-1})	Assignment
300 - 320	a-Si:H (LA)[120]	790	SiC (TO) [121]
340 - 600	a-SiC:H [122]	796	3C-, 4H- or 6H-SiC (TO)
380 - 445	a-Si:H (LO)[120]		[122]
480	a-SiO_x:H (TO)[84, 120]	799	2H-SiC [122]
505	6H-SiC (LA)[122]	888	6H-SiC (LO) [123]
510	c-Si (TO small	960	SiC (LO) [121]
	crystallites)[124]	966	6H-SiC (LO) [122]
514	6H-SiC (LA)[122]	967	3C- or 4H-SiC (LO)
520	c-Si (TO)[125]		[121, 123]
610	4H-SiC (LA) [122]	968	2H-SiC (LO) [122]
630	a-Si:H (LA 2nd overtone)	972	3C-SiC (LO) [122]
	[120]	1332	C (sp^3-hybdization) [126]
760	a-SiC:H [122]	1350	C (D band sp^2
767	6H-SiC (TO) [122]		-hybdization) [126]
777	4H-SiC (TO) [122]	1560	C (sp^3-hybdization) [126]
788	6H-SiC (TO) [122]	2100 - 2150	SiH with C back bonds
			[127]

Raman crystallinity, the three Gaussians contributing to the calculation of F_c are depicted again.

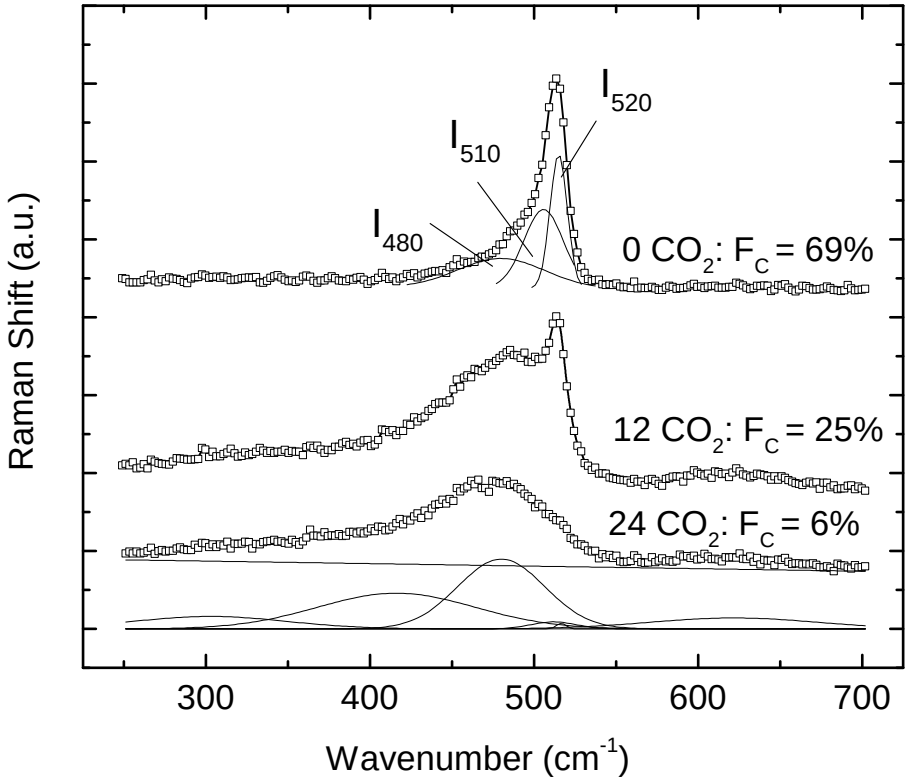

Figure 3.10.: Measured Raman intensities (□) and corresponding fits (thick lines) as a function of wavenumber (stokes shift) for three μc-SiO_x:H samples deposited with the indicated CO_2 flows (in sccm). The hairlines are the corresponding contributions of the Gaussians.

3.2.3. Device Characterization

In this section, the characterization of the solar cell devices is described. Typically, the current-voltage (I-V) characteristics of the cells was measured after 50 minutes of annealing at 160°C. This annealing step improves the adhesion between ZnO:Al and Ag. The measurement was repeated after one week (168 h) of light soaking (one sun, 50°C) to investigate the stability against light soaking. Selected cells were light soaked for a longer period. Additionally, the spectral response and the total reflection as one of the main optical loss mechanisms of the cells were measured before light soaking. An overview about further methods of thin film silicon solar cell characterization is given for example in [114].

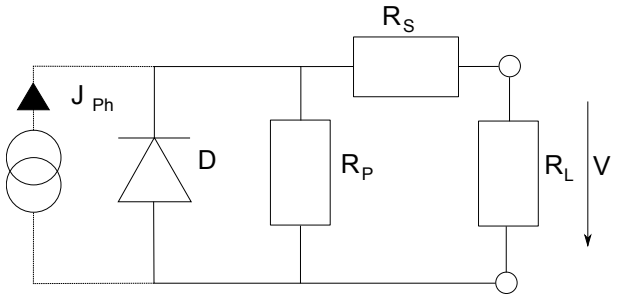

Figure 3.11.: Equivalent circuit of the one-diode model of a solar cell.

Current-Voltage Characteristics

The I-V curves were measured using a Keithley 6517B source meter. The I-V curve of a real thin film silicon solar cell can be described by the one-diode model given in 3.9. Here, a diode D and a shunt resistance are connected in parallel (R_p) and another resistance is connected in series (R_s) as shown in the equivalent circuit given in Fig. 3.11. For the cells in this study, R_p is mainly affected by the laser-structuring of the cells (an exception is discussed in section 6.2). A common problem is for example metal particles remaining in the laser trench ('flaking'). R_p is above $10^4 \Omega cm^2$ for good solar cells. R_s is mainly dominated by the sheet resistance of the TCO and the cell interconnection [104]. Other origins of high series resistance can be the TCO/p-contact [132], the tunnel recombination junction in tandem cells (see section 6.1) and the back contact. It should be in the order of magnitude of 1 Ωcm^2. A discussion of the dark I-V characteristics of a-Si:H/μc-Si:H tandem cells can be found in [133]. In case the solar cell is illuminated, the equivalent circuit can be supplemented by a constant current source providing the photo current J_{Ph}. This is only a simplification as J_{Ph} is voltage dependent in p-i-n cells as the charge carrier separation is mainly driven by the electric field. Analytic expressions for the voltage dependence of J_{Ph} in thin film silicon solar cells can be found in [58, 99, 115].

$$J(V) = J_{Ph} - J_0 \left(exp\left(\frac{V + R_s J}{nkT} \right) - 1 \right) - \frac{V + R_s J}{R_p} \tag{3.9}$$

For the measurements of the illuminated I-V curves a dual-source (Hg and Xe) Wacom WXS-155S-L2 solar simulator (class AAA) was used. The measurements were performed under standard test conditions at 25 °C and 100 mW/cm^2 light intensity (AM1.5g). Prior to the measurement, the sun simulator spectrum was calibrated with respect to the quantum efficiency of the device under investigation. An example of an illuminated I-V curve is given in Fig. 3.12. The power density P as the product of current density and voltage is also indicated together with the main I-V parameters:

- The short circuit current density J_{sc}, which is close to the maximum photo current

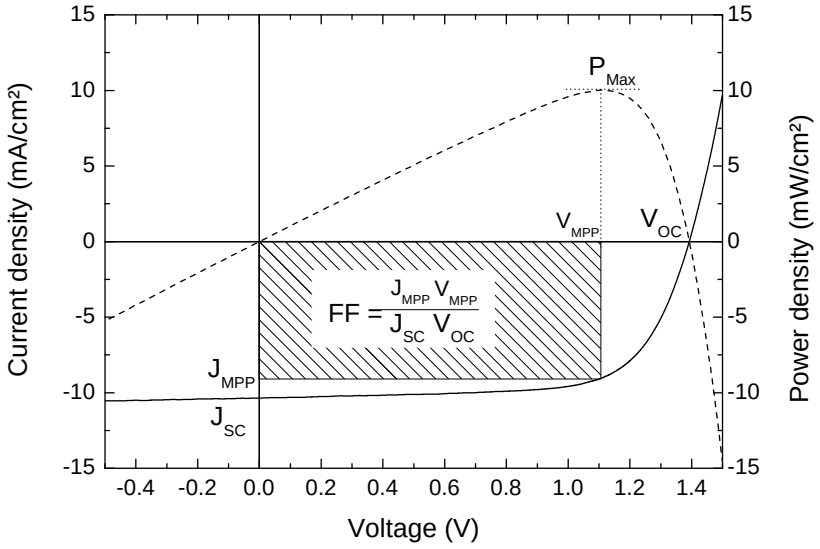

Figure 3.12.: Example of illuminated I-V curve (straight line) of an a-Si:H/μc-Si:H tandem solar cell and the respective I-V parameters. Also indicated is the power density (dashed line)

density in high quality solar cells. It can be limited by the series resistance. Thin film silicon solar cells can have short current densities of up to 28 mA/cm^2 [77].

- The open circuit voltage V_{oc}, the voltage that can be tapped from the solar cell at zero current. It is mainly affected by the band gap of the material and is highly temperature dependent. In multi junction solar cells that are connected loss free, the open circuit voltages of the single cells add up to the total open circuit voltage. It can affected by the shunt resistance R_p.
- The current density J_{MPP} and voltage V_{MPP} at the maximum power point (MPP) and the resulting fill factor FF. The FF is effected by the current matching as described section in section 2.2.1.
- The conversion efficiency can be calculated from this as

$$\eta = \frac{P_{max}}{P_{inc}} = \frac{FF \cdot V_{oc} \cdot J_{sc}}{P_{inc}} = \frac{V_{MPP} \cdot J_{MPP}}{P_{inc}}. \tag{3.10}$$

  where P_{inc} is the power density of the incident radiation.
- Two other valuable parameters that can be extracted from the illuminated I-V curve are the differential resistances at short circuit (R_{sc}) and at open circuit (R_{oc}) condi-

tions,

$$R_{sc} = \left(\frac{\partial J}{\partial V}|_{V=0}\right)^{-1} \; and \quad R_{oc} = \left(\frac{\partial J}{\partial V}|_{J=0}\right)^{-1}. \tag{3.11}$$

The R_{sc} correlates strongly with the R_p and has thus a similar physical meaning. However, it is superimposed by the voltage dependence of J_{Ph}. The R_{oc} consequently correlates with the series resistance. As it is far less affected by the current matching of tandem cells as the FF, it was found to be the parameter most directly related to the functioning of the tunnel recombination junction (TRJ). However, it is affected both by the ideality of the diode and the series resistance. In case non ohmic contact resistances are present in the device (for example at the TCO/p or at the tunnel recombination junction), the IV curve can show an "'s-shape"' behavior. In this case, the one-diode model can be expanded by another diode in blocking direction.

Light Induced Degradation

As solar cells consisting entirely or partially (as a sub cell) of a-Si:H are subject to light-induced degradation, the I-V characterizations of these cells were performed several times during the artificial light induced degradation (LID). The light soaking was performed using a procedure suggested by NREL, which is also described in detail in [99, 115]: In this procedure the cells degrade under open circuit conditions at a temperature of 50 °C. As no current is flowing under these conditions, the recombination rate is (neglecting other influences) higher as under operating conditions were the cells are typically operated close to the MPP. The temperature is set to 50°C to simulate the heating of the devices under operation. The illumination was performed with an AM1.5 similar spectrum at 100 mW/cm^2.

For the LID experiments, two set ups were available at the PVcomB. In the standard light soaker, the temperature was regulated using a ventilation system. In the advanced light soaker, the cell temperature was regulated using a chuck and a water cooling system. Also, the light intensity could be increased up to the value of 3 suns to accelerate the LID process. The cells presented in the following were typically light soaked using the standard light soaker for one week (168h) to confirm the comparability of the results to the baseline and to allow a high throughput of cells. After this period typically >90% of degradation has occured. Selected cells were light soaked for a longer period, to reach the stabilzed values for comparison to literature values, typically obtained after 1000h (compare section 6.4).

Spectral Response and Total Reflection

The spectral response of a solar cell is defined as the current induced per wavelength by an incoming photon flux. It provides valuable additional information to the illuminated I-V curve. The external quantum efficiency (EQE) as a function of wavelength is defined as the ratio of the generated photo current per wavelength $J_{Ph}(\lambda)$ to the incoming photon flux Φ multiplied with the elemental charge e:

$$EQE(\lambda) = \frac{j_{Ph}(\lambda)}{e \cdot \Phi(\lambda)} \tag{3.12}$$

By multiplying EQE with the AM1.5G and integrating over the spectral region of interest, the photo current can be calculated. By applying an external voltage also the bias-dependence of the photo current can be analyzed.

The measurements of single junction solar cells were performed using the differential spectral response method. Here, the difference in the photo current induced by a small monochromatic light source are measured. As the splitting of the Fermi levels and thus the collection in the p-i-n devices is dependent on the irradiation, the measurements were performed under a white light bias. Together with the sample, a monitor solar cell was measured. The spectral response of the sample was then calculated using the ratio of the spectral current of the sample to the monitor cell. This is multiplied with the ratio of the spectral photo current of the monitor cell to the one of a calibration cell and the known spectral response of the calibration cell. The set up and the procedure are explained in the diploma thesis of T. Hänel [134].

For the measurements of the sub cells in multi junction solar cells, filtered bias light is used: To measure a particular sub cell, the stacked cell has to be biased so that the current of the sub cell of interest is the limiting one. For the measurement of the top cell, the white light of the bias halogene lamp is sufficient. The bottom cell was measured by flooding the top cell using a blue filter (Schott BG39). The standard EQE measurements were performed under quasi short circuit conditions. To compensate the voltage generated by the flooded cell, which shifts the cell under investigation away from short circuit conditions, a positive bias is applied of 400 mV for the measurement of the top cell and 500 mV for the bottom cell. Especially, for the development of the IRL (see section 2.2.2), where the EQE allows an exact quantification of the gain in the top cell current, as well as for the matching of the tandem solar cells the spectral response measurements of the devices were of high importance.

Also depicted is the total spectral absorbance of the cell, as calculated from the difference of the spectral reflectance to unity ($1 - R$). The spectral reflectance was measured using the spectrophotometer setup (see the section 3.2.2 for a description) and the integrating

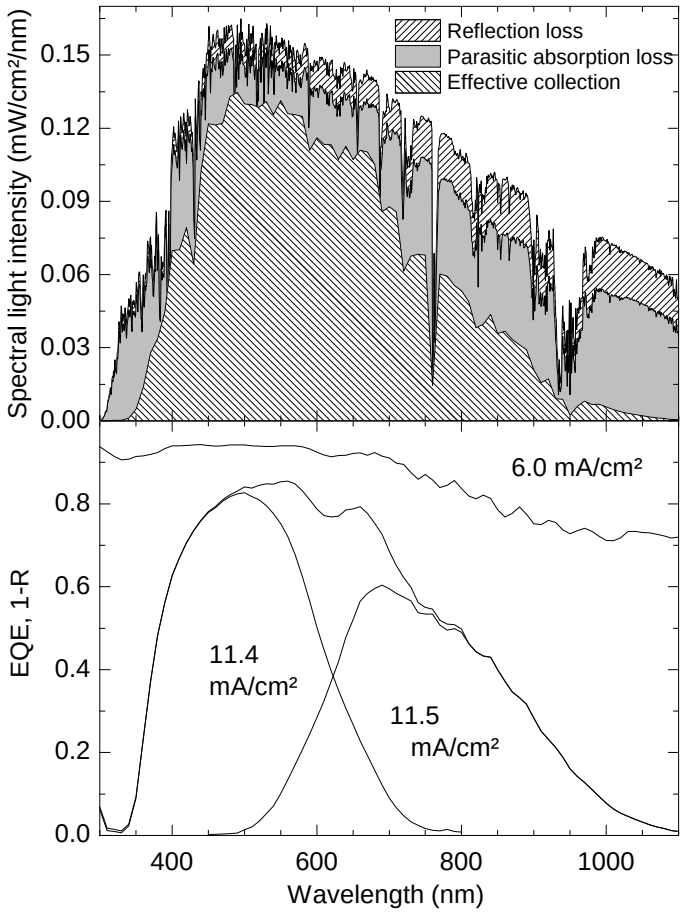

Figure 3.13.: (Top) The AM1.5 standard spectrum for the measurement of solar cells. The indicated areas underneath the curve correspond to the current that is reflected (forward hatch) and converted (backward hatch), respectively. The gray area in between corresponds to the optical loss due to parasitic absorption. (Bottom) the external quantum efficiency of a tandem cell. The EQE of the sub cells (top cell (300-800 nm) and bottom cell (450-1100nm)) are indicated. The total reflection R is plotted as the difference to 1.

sphere. From this the *internal* quantum efficiency (IQE)can be calculated according to

$$IQE = \frac{EQE}{1 - R}. \tag{3.13}$$

It should be mentioned that another definition of the IQE exist, that only considers the probability of the absorption in the *active* layers. As the contribution of the functional layers, such as the glass substrate, the TCO front contact and the back reflector is typically high in thin film silicon solar cells, the difference is high. This so called parasitic absorption can only be quantified using optical modeling (see for example [135]). The total absorbed current, the reflected current as well as the parasitic absorption as part of the AM1.5 are depicted in the top part of Fig. 3.13. As can be seen, the amount of

parasitic absorption is considerable. This is one important motivation for the extensive development of wide band gap materials for the functional layers in thin film solar cells.

During the development of a-Si:H/μc-Si:H tandem cells deposited on thick substrates at PVcomB, significant deviations existed between the short circuit current density as determined by the sun simulator ($J_{SC-SoSim}$) and the currents from the EQE existed. In particular, there was a difference between the $J_{SC-SoSim}$ and the short circuit current density of the bottom sub cell as determined by EQE (J_{SC-BC}) of up to -0.5 mA/cm^2 in case of bottom cell limitation. As the sub cells are connected in series, the $J_{SC-SoSim}$ must be equal to the current of the limiting sub cell (see section sec:multijunctions) and thus the measured values were not physical. A phenomenological explanation for this divergence becomes apparent when comparing nominally same cells: one structured in the cell design and the other in the module design as depicted in Fig. 3.14.

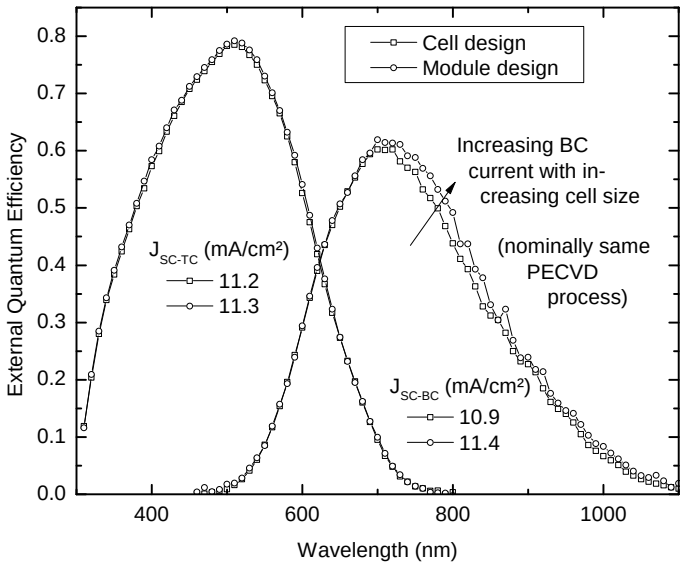

Figure 3.14.: EQE as a function of wavelength for two nominally same cells, one stuctured in the cell design and the other in the module design.

The difference in the bottom cell current that can be observed is assumed to be due to the difference in the cell size. As the devices are deposited on a rough substrate, the light is scattered and part of the light is scattered out of the defined cell area (the spot size of the light beam is 4 x 4 mm^2 compared to 10 x 10 mm^2 cell area). The difference between cells of different size is naturally higher for larger wavelengths due to the decreasing absorption coefficient and therefore the J_{SC-BC} is systematically underestimated in the cell design. Similar conclusions regarding the the divergences between EQE and sun simulator measurements on thin film silicon solar cells in superstrate configuration were drawn by Müller et al. [136].

4. Silicon Oxide

In this chapter, the results of the experiments concerning the hydrogenated microcrystalline silicon oxide (μc-SiO$_x$:H) are presented. In the first part (4.1), the literature about the material as well as its application in solar cells is summarized. In section 4.2 the results obtained on single layers regarding the growth of the material in relation to the gas phase mixture are presented. In the following sections, the results regarding the influence of RF power and pressure (4.3), regarding the doping of the material (4.4) and regarding the stability of the material against annealing are presented (4.5). In the final section of this chapter (4.6), the results are being discussed. The results of the integration of μc-SiO$_x$:H into the a-Si:H/μc-Si:H tandem cells are presented in chapter 6.

4.1. Literature

The first successful incorporation of μc-SiO$_x$:H in silicon thin film solar cells was reported by Fuji company in 1994 [13]. A detailed study of the microstructure was then published by Das et al. [137]. Further studies revealed that the material consists of a microcrystalline silicon phase and an amorphous silicon oxide phase (compare Fig. 2.4 in section 2.1.3). Its application as an intermediate reflector in a-Si:H/μc-Si:H tandem cells was first reported by Yamamoto et al. [9] and the Jülich and the Neûchatel groups in 2007 [10, 89]. Both groups use the precursors SiH_4, CO_2 and PH_3 and high hydrogen dilutions (H_2/SiH_4) of 200-500. In Neûchatel very high frequencies 60-200 MHz are used and a power density of 0.01 – 0.1 W/cm^2 at relatively low pressures of around 70 Pa. Due to the different process regime, these values are less comparable to those of this work as the ones reported by Jülich, who use conventional 13.56 MHz frequency, a power density of 0.3 mW/cm^2 at around 400 Pa.

Since then, many publications have been dedicated to μc-SiO$_x$:H and its application to thin film silicon solar cells. Cuony et al. have shown the first application of the material as top cell [51] and later also in the bottom cell p-layer [15]. If used as the p-layer, the cell gains from reduced parasitic absorption as well as an improved index matching between the TCO and the a-Si:H top cell. Successful integration of p- and n-type μc-SiO$_x$:H into an industrial type process on large area in a conventional 13.56 MHz AKT reactor was shown by Applied Materials [52, 138]. The application as n-type window layer for n-i-p-

μc-Si:H cells was shown by Smirnov et al. [139]. Another positive influence on the performance of silicon solar cells particularly on rough substrates was described by Despeisse et al. [25]: The low in-plane conductivity of the μc-SiO_x:H reduces current drains evoked by shunts (shunt quenching), which appear preferably when microcrystalline silicon is grown on very rough surfaces. An increased current of μc-SiO_x:H/Ag back reflector with an adjusted thickness of the μc-SiO_x:H layer serving both as the n-layer and as part of the reflector over a standard ZnO/Ag reflector has been observed for a-Si:H single junction solar cells by Della Veneri et al. [140] and for μc-Si:H single junctions and a-Si:H/μc-Si:H tandem cells by Janthong et al. [141]. Another field of application outside of the thin film technology is in the emitter fabrication for hetero junction solar cells [142–144].

The influence of μc-SiO_x:H deposition parameters as well as the gas composition of precursors on the film growth has been studied intensively. The main conclusions can be summarized as follows: (1) Through the addition of CO_2 into the gas phase of a μc-Si:H regime, oxygen is built into the amorphous phase and the resulting layers become more transparent and their refractive index n decreases, approaching the value for SiO_2 [10, 11, 137]. At the same time, the Raman crystallinity decreases and the material becomes less conductive. (2) The Raman crystallinity of the material can be increased with an additional hydrogen dilution. However, the influence of H_2 dilution on n shows different trends: Increasing n by Lambertz et al. [11] and decreasing by Buehlmann et al. [10]. (3) p- and n-type doping are possible through the use of standard dopand sources like PH_3 or TMB. n-type doping is typically more efficient than p-type doping, because of the deterioration of the crystallinity through the addition of the p-dopant source TMB, which will be shown in more detail in the section about doping (4.4) and which has also been previously observed by the Neûchatel group [15, 25]. Das et al. reported that the crystallinity increases with higher deposition temperature, which can be attributed to the increased surface diffusion length of the adatoms [145].

4.2. Influence of Gas Phase Composition

The first experiments regarding SiO_x were based on a recipe, which was then standard for the bottom cell n-layer. This layer was the first one consisting of μc-SiO_x:H. The deposition parameters are given in table 4.1. All layers were deposited in chamber B.

Compared to values reported in literature, especially the high pressure of 1.2 kPa is noticeable compared to the mentioned values above from literature. The influence of the pressure is studied in detail in section 4.3. To compare the layers deposited in the AKT1600 at PVcomB with the layer characteristics reported in literature, several variations have been performed: The CO_2 to SiH_4 ratio was varied between 0 and 2 and these variations were combined with a variation of the hydrogen dilution (*HD*) from 200 to 400.

Table 4.1.: Deposition parameters for the study of the gas phase composition of μc-SiO$_x$:H. The explanation for the deposition parameters is given in section 3.1.1.

SiH_4 (sccm)	H_2 (sccm)	CO_2 (sccm)	PH_3 (sccm)	T (°C)	P (W)	p (kPa)	d_{el} (mm)
10	3000	0 – 16	6	185	500	1.2	16.5
	2000	12, 20					
	4000	12, 20					

The top graph of Fig. 4.1 shows the trend of E_{04} versus the CO_2/SiH_4 ratio. With increasing CO_2 flow, more oxygen is incorporated into the layer. The CO_2 molecules get dissociated in the plasma into CO and O. Since the dissociation energy of the residual CO molecule is much higher, no further dissociation of this molecule occurs. As RGA data show, much of this species is found in the residual gas. The contribution of CO to the film growth is negligible. In the amorphous phase, oxygen incorporation leads the building of Si-O-Si complexes as FTIR measurements on a-SiO$_x$:H layers have revealed [137, 146], which lead to an increase of the optical absorption gap (this is also in accordance with calculations of the density of states for a-SiO$_x$:H [147, 148]). The increase in *HD* decreases the effect of an increased band gap.

As can be seen, the deposition rate decreases at first with the addition of CO_2 into the gas phase and then increases again slightly. As expected, the growth rate is lower for a higher H_2 dilution. These trends as well as the observed minimum at around a ratio of $CO_2/SiH_4 = 0.5$ are similar to the values reported by Lambertz et al. [11]. The Raman crystallinity decreases at first only slightly with increasing CO_2 admixture and then more rapidly at a ratio of 1.2. The positive influence of an increased hydrogen dilution on the crystallinity of a film is known from pure μc-Si:H layers as described in section 2.3. The refractive index at a wavelength of 800 nm decreases from a value at around 3.1 down to a value of 1.7 with the increase of the CO_2/SiH_4 ratio from 0 to 2. At the same time, the conductivity drops several orders of magnitude from a value above 100 S/cm to values below the sensitivity of the measurement set-up (10^{11} Ohm). This decrease is sharper then the ones reported by Lambertz et al., where films of a Raman crystallinity of below 10 % still show a conductivity of $10^{-}2$ S/cm. The difference was ascribed to the relatively low doping level used in this series. A PH_3 doping series is shown in section 4.4.

It can also be seen in Fig. 4.1 that the deposition rate decreases with increasing *HD* and the crystallinity increases as it is known from μc-Si:H [11]. Similar to the results reported from Jülich but contrary to the results published by Bühlmann [10], the refractive index

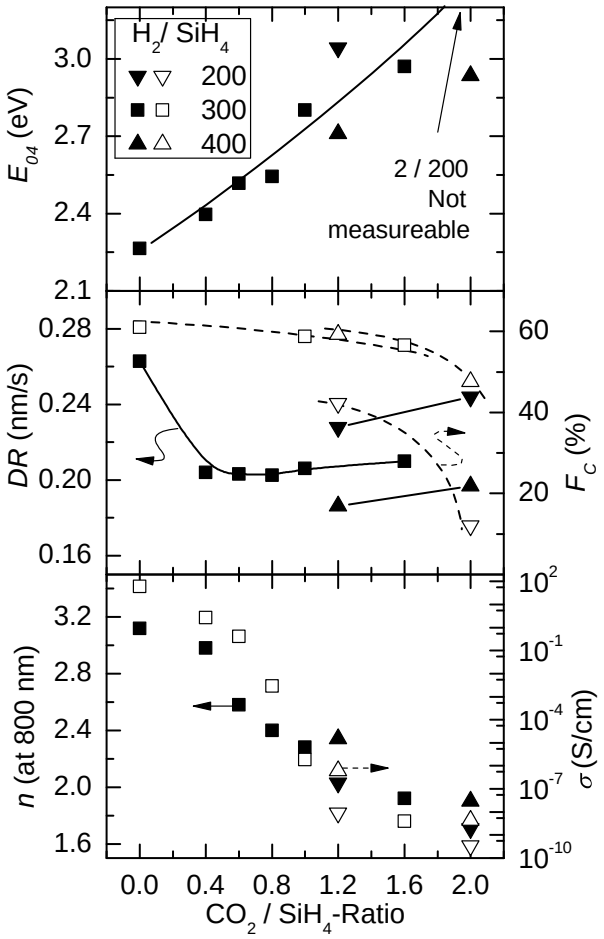

Figure 4.1.: The influence of the CO_2 to SiH_4 ratio onto (top) the E_{04}, (middle) deposition rate, DR and Raman crystallinity, F_c, and (bottom) the refractive index n at 800 nm measured by spectral ellipsometry and the conductivity σ for various H_2 dilutions. The closed symbols correspond to the left and the open symbols to the right axes. Lines are guides to the eye.

n increases with increasing HD (opposite trend to the one of E_{04}). The opposite trend described by Bühlmann et al. is explained by an increased oxygen incorporation into the film, which is in agreement to presented FTIR results. Supporting this argumentation, Iftiquar also observed an increase in oxygen incorporation upon increased hydrogen dilution in a-SiO_x:H layers. On the other hand, Rutherford Back-Scattering results presented by Lambertz et al. show a decreased oxygen incorporation into the film like in the samples prepared for this thesis. This contradiction could be due to the differences in the PECVD regime and in excitation frequency. The conductivity increases with increasing HD following the trend for F_c.

4.3. Influence of Deposition Power and Pressure

In this section, the results of the experiments regarding the influence of the deposition power and pressure on the film properties are presented and discussed. Parts of the results have already been published [149].

Motivation and Experimental Details

These studies have been conducted in more detail, since a complete analysis of this issue was not available in literature. Sarker et al. reported some observations that oxygen incorporation (and therewith n) and F_c is correlated to the power density used [150]. Moreover, as mentioned above, the initially used deposition pressure of 1.2 kPa for n-type μc-SiO_x:H layer differed significantly for the values reported by Lambertz et al. [11]. Furthermore, early experiments with pressure variations for the intermediate reflector layer on the device level showed improvements for medium pressures (0.8 kPa) and then a complete blocking of the cell at small pressures of 0.5 kPa. Whereas the latter trend can be explained by the reduced crystallinity of the layer, the understanding of what happens at high pressures is still under investigation. The studies were accompanied by *insitu* diagnostics of the plasma (OES and RGA). The used deposition parameters are given in 4.2. Compared to the study on the influence of the gas phase composition in section 4.2, only the doping gas flow was increased, which was a result of the cell development, which was on going in parallel.

Table 4.2.: Deposition parameters for the study of the influence of deposition power and pressure on μc-SiO_x:H. Compared to the values in 4.1 mainly the doping-gas flow has increased, which was a conclusion from the cell-development which was on going in parallel.

SiH4 (sccm)	H_2 (sccm)	CO_2 (sccm)	PH_3 (sccm)	T (°C)	P (W)	p (kPa)	d_{el} (mm)
10	3000	12	14	185	500	0.5 – 2.4	16.5
					200 – 600	0.8	
					400	1.2	

Results Film Characterization

Fig. 4.2 shows the dependencies of n, DR and F_c on the deposition power and pressure. As can be seen, DR increases with increasing power and pressure, which is the expected

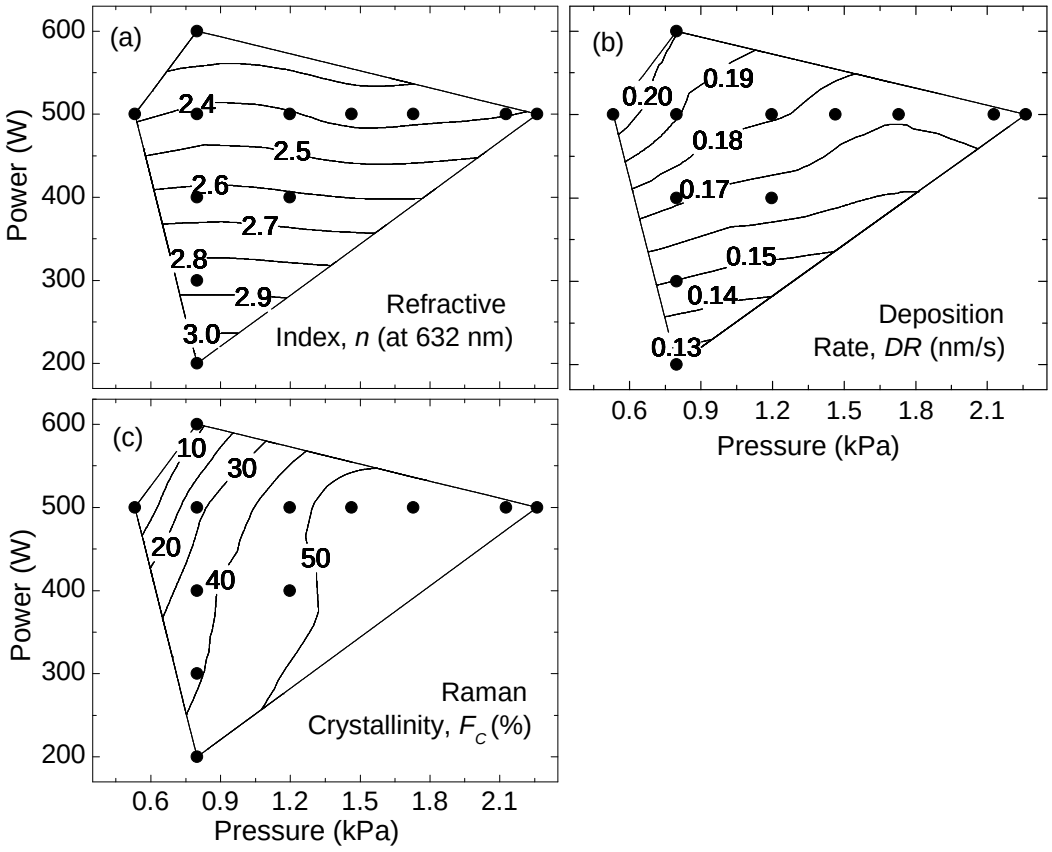

Figure 4.2.: Contour plots of the influence of deposition power and pressure on (a) refractive index n at 632 nm, (b) deposition rate DR and (c) Raman crystallinity F_c of n-type μc-SiO$_x$:H layers.

behavior, as the dissociation rate of SiH_4 and CO_2 increases with the power P. The dependence of DR on the pressure p is less pronounced. It is assumed that with increasing pressure ion bombardment decreases, which can hinder the growth in μc-Si:H plasma regimes [90].

The trends for F_c as function of P and p, however, are different from the behavior reported for μc-Si:H plasmas without CO_2, which are described for example in [90]: Typically, with increasing P the dissociation of hydrogen increases stronger than the one of silane as described in section 2.3. Thus, more atomic hydrogen is available on the surface and can promote the crystalline growth. In the case of the analyzed μc-SiO$_x$:H plasma, the increased power induced (besides the decrease of F_c from 0.4 to 0), also a lowering of the refractive index of the resulting films from 3.0 at 200 W to 2.2 at 600 W (comparable to a change in the precursor gas ratio CO_2/SiH_4 from 0.4 to 1 as described in the previous section). Therefore, indicating that the oxygen incorporation increases due to a relatively higher dissociation of CO_2 with increasing power. An increase of the oxygen incorporation upon increasing power density was previously also observed by Sarker et al. [150].

As can be seen, the F_c of the material increased again with increasing pressure without a major change in refractive index, which is a technologically interesting observation, as a high Raman crystallinity for the conductivity *and* a low refractive index for the reflectivity is desirable for the IRL. For pure μc-Si:H plasmas in the high-pressure depletion regime, an increase of deposition pressure usually leads to a decrease of F_c as the power density per molecule decreases and thus relatively less atomic hydrogen is available on the surface [151]. Furthermore, a decrease of F_c with decreasing pressure (below 0.3 kPa) has also been observed for pure μc-Si:H deposited at high power densities, which was explained by the higher electron temperature and resulting increased ion bombardment [152].

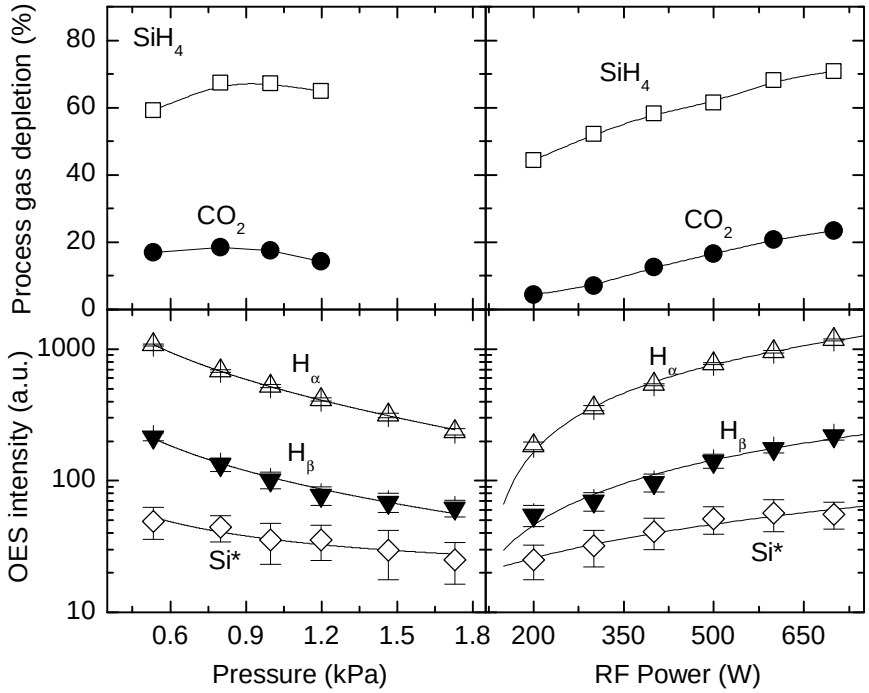

Figure 4.3.: Measured μc-SiO$_x$:H plasma properties as functions of deposition pressure (left) and power (right) for: process gas depletion as determined with RGA (top row - lines are guides to the eye) and OES peak intensities of the denoted lines (bottom row - lines are fits according to P/p).

Results Plasma Diagnostics

To confirm the assumption regarding the oxygen incorporation and to investigate the role of the deposition pressure further, OES and RGA measurements were conducted (see section 3.2.1 for a description). Therefore, the deposition pressure and power were varied in two series within the same parameter room as given in table 4.2 but a slightly increased

electrode gap (17.8 mm), which was necessary to obtain a reasonable OES signal. The results are depicted in Fig. 4.3.

The process gas depletion (see section 3.2.1 for the definition) is not effected much by the pressure variations (due to technical constraints induced by the RGA, higher pressures than 1.3 kPa cannot be measured). In the power series, both, the CO_2 and the SiH_4 depletion increase linearly with the RF power. Due to the constant gas flows, the ratio CO_2/SiH_4 depletions correlates according to equation 3.2 with the oxygen content in the layer $[O/Si]_{layer}$. Fig. 4.4 shows the the refractive index as a function of the calculated ratio $[O/Si]_{layer}$. The data confirm the stated assumption that the higher RF powers increase the O incorporation into the film, which is known to decrease the crystallinity [11] presumably due to hydrogen removal from the surface [100].

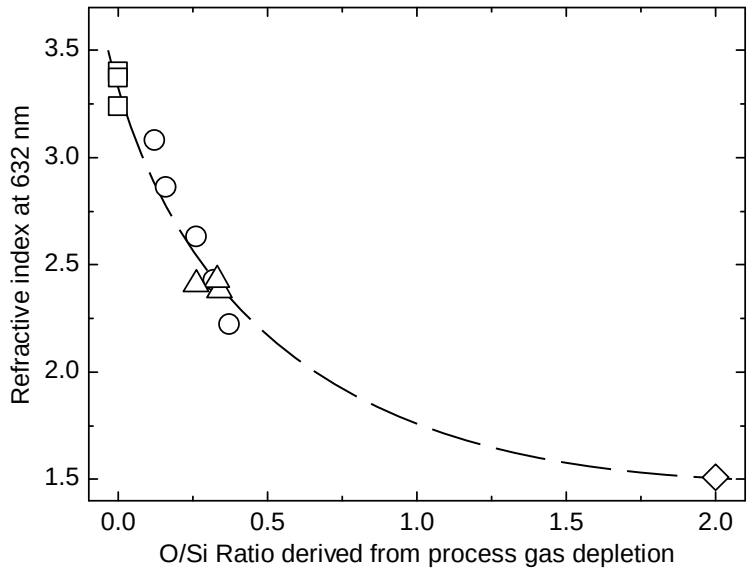

Figure 4.4.: Refractive index against the $[O/Si]_{layer}$ ratio as determined from process gas depletion using RGA. The symbols indicate the same data as in Fig. 4.5, i.e.: power series with CO_2 (○), without CO_2 (△) and pressure series (□). The data point for stoichiometric SiO_2 is also indicated (◊) from literature.

The OES peak intensities of H_α, H_β and Si* shown in Fig. 4.3 have the known linear dependency on P/p as described above. The quantity Si^*/H_α is a measure for the amount of available atomic hydrogen and has a strong correlation to the crystallinity in *intrinsic* μc-Si:H films as was described in [90, 153]. However, looking at Fig. 4.5, where the Raman crystallinity F_c is plotted against Si^*/H_α one can see that the trend is contrary to the one reported in literature for μc-Si:H, i.e. higher Si^*/H_α correlate with lower F_c values. The lower Raman crystallinities are, however, not assumed to be *due* to the higher amount of atomic hydrogen but *despite* this fact. The origin of the reduced crystallinity, which correlates with increasing ratio of P/p in the investigated regime is assumed to be the

result of the increased oxygen incorporation into the film as the trends for the refractive index suggest in the case of increased power. It can be seen that also for the layers without CO_2 admixture the crystallinity decreases slightly with the decreasing Si*/H_α. It could be due to higher ion bombardment or increased phosphor incorporation hindering the growth. It is assumed that eventually F_c will decrease again after a broad maximum for higher ratios of Si*/H_α and following the reported trend in literature. Depositions were performed to investigate this assumptions at lower powers and higher pressures. The crystallinity increased up to a power of 100 W at 0.8 kPa, however, no OES signal can be obtained due to the low molecule dissociation. For very high pressures of up to 2.2 kPa at 500 W, F_c remained around 0.5. The shift of the decreasing flank towards higher Si*/H_α is assumed to be due the higher hydrogen dilution used here compared to Ref. [153] (factor 1.5 and higher). The higher crystallinity for higher pressures can be explained either by increased SiH_4 depletion and, as a consequence, less hydrogen annihilation (Eq. 2.1) or by reduced ion bombardment.

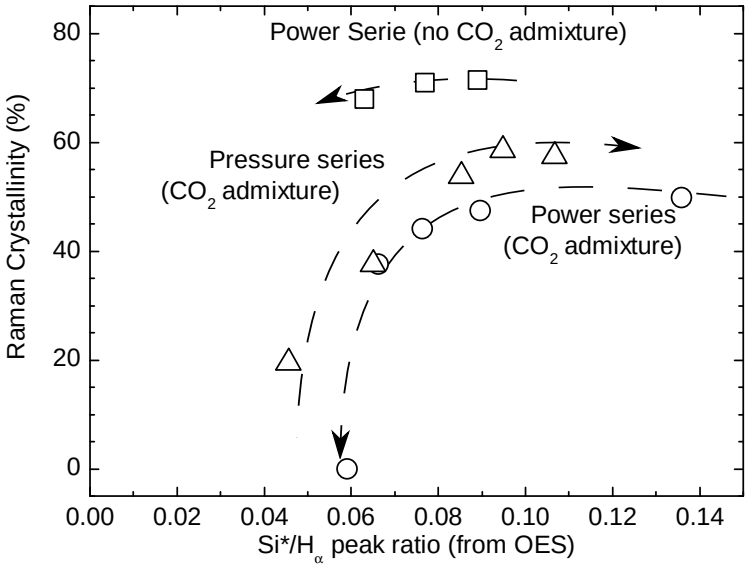

Figure 4.5.: Raman crystallinity as a function of Si*/H_α for the power(○) and pressure (△) series. The arrows indicate the direction of increasing power and pressure, respectively. Values for the same layers without CO_2 admixtures deposited at varying RF powers (□) are given for comparison.

It can be summarized that the power and pressure have a significantly different influence on the microstructure of μc-SiO_x:H films than on pure μc-Si:H films. This difference can be explained by the increased oxygen incorporation upon increased RF power, which hinders the growth. The crystallinity can be greatly enhanced by adjusting the deposition pressure. RGA was found to be a useful tool for predicting the refractive index of the resulting layer.

4.4. Influence of n- and p-Type Doping

Doping of μc-SiO$_x$:H can be achieved via the use of standard dopant gases such as PH_3 for n- [10, 89] or TMB for p-type doping [51, 154]. For a given oxygen dilution, the crystallinity, which can be tuned via the H_2 dilution or the deposition pressure (as shown above), dominates the conductivity and the activation energy.

It was found by the Neûchatel group that higher conductivities can be obtained for n-type than for p-type μc-SiO$_x$:H for a given CO_2/SiH_4 and *HD* [25]. This is presumably to a large extent due to the fact that the crystallinity is hindered by the TMB flow [15]. The conductivity has thus an optimum at low TMB flows with low doping on the one side and low crystallinity on the other side as it has been experimentally observed by Cuony et el. [51]. It should be mentioned that also for a-SiO$_x$:H it was reported that p-type doping is less efficient than n-type doping for low oxygen concentrations up to 20 at. % [45]. Reasons given were the compensation of boron by oxygen, which was previously also observed for a-Si:H [155], as well as a possible passivation of boron acceptors through the accumulation of B-H complexes [156–158]. On the other hand, from μc-Si:H p-layers, it is known that high conductivies of up to 10 S/cm (compared to 100 S/cm for n-type) can be achieved [159]. Although, it was also found that for high dopant gas ratios the crystallinity and consequently the conductivity decreases.

Single Layer Results

To investigate this effect systematically, a series of single layers were deposited with varying dopant source gas flows: based on the deposition parameters at values, which were then standard for the top cell μc-SiO$_x$:H p- and n-layers, varying amounts of PH_3 and TMB were added. All layers were deposited in the same chamber with NF_3 plasma cleaning done between individual depositions. The deposition parameters are given in table 4.3. The results of the optical, electrical and structural characterizations are sum-

Table 4.3.: Deposition parameters for the study on the influence of doping on the properties of μc-SiO$_x$. The dopant gas dilution was 2% in H_2.

CO_2/SiH_4	SiH4 (sccm)	H_2 (sccm)	CO_2 (sccm)	PH_3/TMB (sccm)	T (°C)	P (W)	p (Torr)	d_{el} (mm)
0	10	3000	0	*var*	185	500	0.8	16.5
0.9	12	4800	11	*var*	185	330	0.7	15.2
1.8	10	3000	18	*var*	185	500	0.8	16.5

marized in the plots of Fig. 4.6. For the p-type samples without CO_2 admixture, data taken from Roschek were added [103], which were deposited under similar conditions ($H_2/SiH_4 = 267$, RF power = 175 mW/cm^2 at 0.5 kPa, 2 % TMB in He) and can be considered as state of the art μc-Si:H p-layers, due to a lack of own data.

Looking at the conductivity values, one can observe similar trends as observed in the mentioned literature sources for the p-type material: The conductivity increases with increasing TMB flow up to a maximum, which is for the presented regime at a TMB flow of 4 sccm and then declines again. From the Raman measurements, it is evident that this decline in conductivity is due to a reduced crystallinity. The trend for the deposition rate on dopant gas flow for p-type material was also observed by Roschek et al. and explained by the fact that p-type surfaces increase the growth of μc-Si:H, which is by cationic chemisorption [160]. In the case of the use of B_2H_6 as dopant source, it was also observed that catalytic H-removal occurs due to the desorption of BH_x complexes, which causes an increase in the surface dangling bond density and an increase in the sticking coefficient [161, 162]. It is not clear, weather this occurs for TMB doping, too. The decrease of E_{04} with increasing TMB/SiH_4 ratio could be an indication for increased defect absorption. No clear conclusion could be drawn from the trend of the refractive index (not shown) as the data base is limited and the error due to fitting is most likely high since the comparison of materials with very different crystallinities has a systematic error, as described in section 3.2.2.

For the n-type material, the trends are in general similar: The crystallinity decreases with increasing dopant gas admixture while the conductivity increases. A maximum in conductivity was not clearly reached for the series with a CO_2/SiH_4 ratio of 0.9. Therefore the points of the series with the ratio of 1.8 are added, where one can see that the PH_3 admixture eventually also leads to a reduction in the conductivity, however, at much higher values. The deposition rate as well as the E_{04} are far less affected than in the p-series. Despite the similarity in the trend, the negative impact of the PH_3 admixture onto the crystallinity is far less pronounced, which leads to the highest in-plane conductivity for n-type material of 10^{-2} S/cm. This is four orders of magnitude higher than the maximum of the p-type conductivity at 10^{-6} S/cm. It can thus be concluded that the difference between n- and p-type conductivity is higher with CO_2 admixture.

A technologically important observation, which was found to be far more pronounced within the device (compare section 6.4) is indicated by the slope of the dashed lines connecting the n-type layers with and without CO_2 admixture: The conductivity of the layers without CO_2 admixture is already high for a low PH_3 flow of 8 sccm and remains on a similar level when the flow is increased to 32 sccm. In the series with CO_2 admixture the slope is not as steep, indicating that more PH_3 is needed for a sufficiently high doping when CO_2 is added.

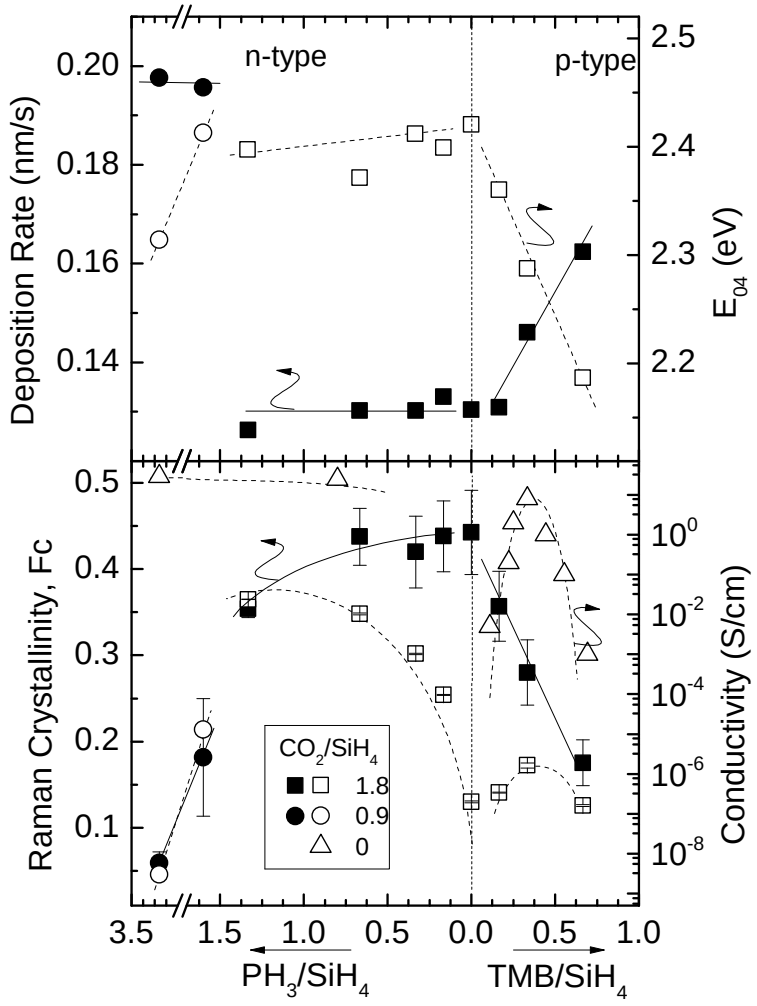

Figure 4.6.: (Top) Deposition rate and optical gap, E_{04} and (bottom) Raman crystallinity, F_c and in-plane conductivity σ as a function of dopant source gas flow PH_3/SiH_4 (left) and TMB/SiH_4 (right). The open symbols correspond to the right and the closed to the left axes. The error bars correspond to the the spread of measurements performed at different locations on the 30 x 30 cm^2 panel. The lines are guides to the eye. The data for the p-type samples without CO_2 admixture are taken from literature [103]. The lower limit of the method for determining the conductivity was reached for the intrinsic sample and the sample deposited at 32 sccm PH_3.

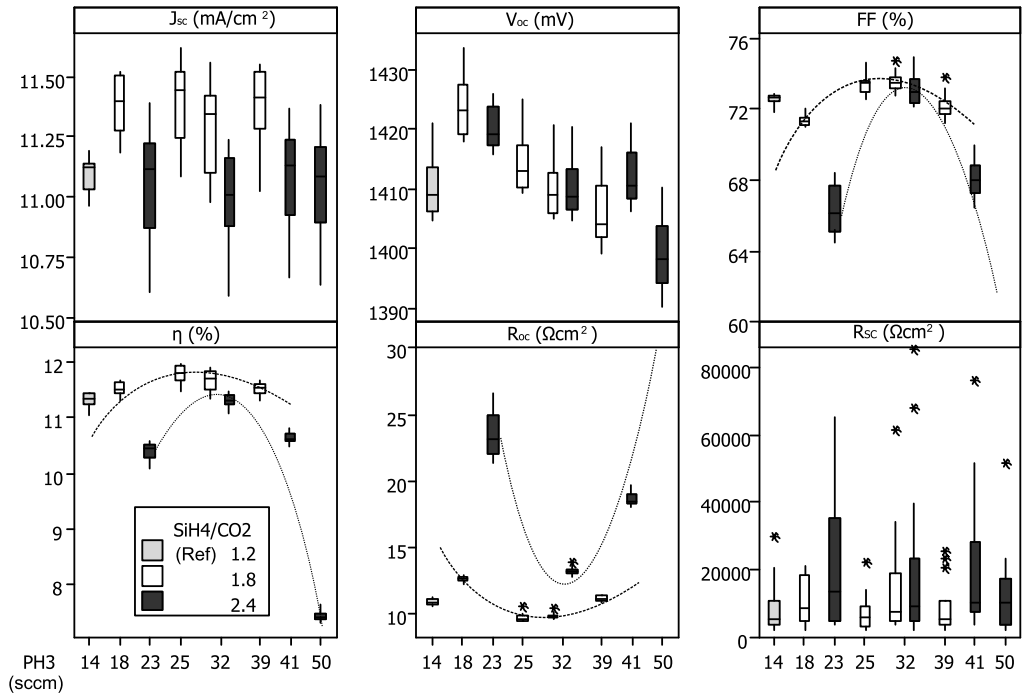

Figure 4.7.: Box plots of the solar cell parameters of two series of tandem cells with varying PH_3 flows in the intermediate reflector layer for two series deposited with a CO_2 flow of 18 and 24 sccm, respectively. The box for the R_{oc} of the sample deposited with 50 sccm PH_3 and 24 sccm CO_2 lies outside of the plot and has a median of 77 Ωcm^2.

Comparison to Solar Cell Results

To emphasize this effect, the solar cell parameters of nine runs deposited with different n-type μc-SiO_x:H intermediate reflector layers (IRL) are depicted in Fig. 6.5. The solar cells belong to two PH_3 series with two different CO_2 flows as indicated. The μc-SiO_x:H deposition parameters are the same as for the single layer series that are given in table 4.3 with variations in the CO_2 flow (12, 18 and 24 sccm) and in the PH_3 flow as indicated. The SiH_4 flow was fixed at 10 sccm. The thicknesses of the top cell, the IRL and the bottom cell are 280, 60 and 1800 nm. The cells were deposited on etched ZnO:Al.

It can be seen that the conversion efficiency is dominated by the FF, which is again dominated by R_{oc}. This can be ascribed to the μc-SiO_x:H IRL. The conversion efficiencies have a maximum, which are located at a PH_3 flow between 25 – 32 sccm for the series with 18 sccm CO_2 and at 32 sccm for the series with 24 sccm CO_2. The cells from the best run were 4% better than the reference baseline cell. After 168h light soaking, this improvement remained.

It is assumed that the contribution of the μc-SiO_x:H IRL in the best tandem cells from this series to the R_{oc} is below 1 Ωcm^2. This assumption is based on comparisons of cells

with IRL, to a cell without an IRL. Comparing the R_{oc} of the solar cells and the in plane conductivities of the layers given in Fig. 4.6 for the layer deposited with 18 sccm CO_2 and 18 and 32 sccm PH_3, we can see that on the single layer basis, the conductivity decreases with the increasing PH_3 flow, whereas the R_{oc} decreases on the cell level. This can be partially attributed to the existence of a seed layer in the tandem cell. When comparing the absolute values of the in-plane conductivity of the 100 nm single layer deposited with 32 sccm PH_3, which was below the sensitivity of the hand held measurement system ($> 10^{11}\Omega$) to the assumed top-bottom contribution of the IRL to the R_{oc} ($< 1\Omega cm^2$), it can be calculated that the top-bottom conductivity in the IRL is more than two orders of magnitude higher than the in-plane conductivity of the single layer.

It can be concluded that a high PH_3 gas flow ratio is necessary for optimized IRL properties. This effect is even more pronounced on the device level than on the single layer level. In case of the optimized μc-SiO_x:H layer, the trends observed on the single layers can even be misleading, as described above. The conductivity of the p-layers is several orders of magnitude lower than the ones of the n-layers. This is ascribed to the more detrimental effect of TMB compared to PH_3 onto the crystallinity. Further potential is thus believed to lie in the optimization of the p-layer by understanding and controlling the crystalline growth during p-type doping.

4.5. Stability Concerning Annealing

The stability of μc-SiO_x:H concerning annealing and storage at ambient pressure has not been discussed in literature so far. From μc-Si:H, which is assumed to be a component of μc-SiO_x:H, it is known that the conductivity is not stable under atmospheric pressure but subject to change related to the incorporation of impurities into the material, such as oxygen acting as an n-dopant or water particularly for very crystalline material with a high degree of porosity [24, 163, 164]. Finger et al. reported a decrease in the dark conductivity for i-type μc-Si:H of more than two orders of magnitude for porous material upon exposer to ambient pressure. This was correlated to an increase in the spin density as determined from electron spin resonance measurements, which was related to oxygen and/or water adsorption. For device grade, dense material the opposite was observed. Here the conductivity increases upon the exposure to air. The change, which is attributed to the incorporation of water, can be recovered through an annealing step at 160°C.

For a-SiO_x:H, the other component of μc-SiO_x:H, it was shown by Janssen et al. that the conductivity increases by more than two orders of magnitude depending on the oxygen content at annealing temperatures as low as $T_{anneal} = 250$°C (films were deposited at $T_s = 250$°C) [45]. However, the observed change was strongly dependent on the type of doping: while the change for p-type material was as mentioned two orders of magnitude,

a slight decrease was observed for the n-type material at the low annealing temperatures. The reason stated for the change in the p-type material was the effusion of hydrogen, weakly bonded to boron atoms and the consequent activation of the boron dopants. No conclusions were drawn regarding the decrease in the conductivity for the n-type material.

To investigate the effect of temperature treatments onto the conductivity of the doped μc-SiO_x:H, a series of single layers with varying PH_3 flows was measured before and after annealing. For the annealing step, the same parameters were chosen as for the cells in the baseline process (160°C for 50 minutes at ambient pressure). The measurements were repeated two month after the annealing step for a second time, to investigate the effect of the storage of the samples at ambient pressure. The results are given in Fig. 4.8.

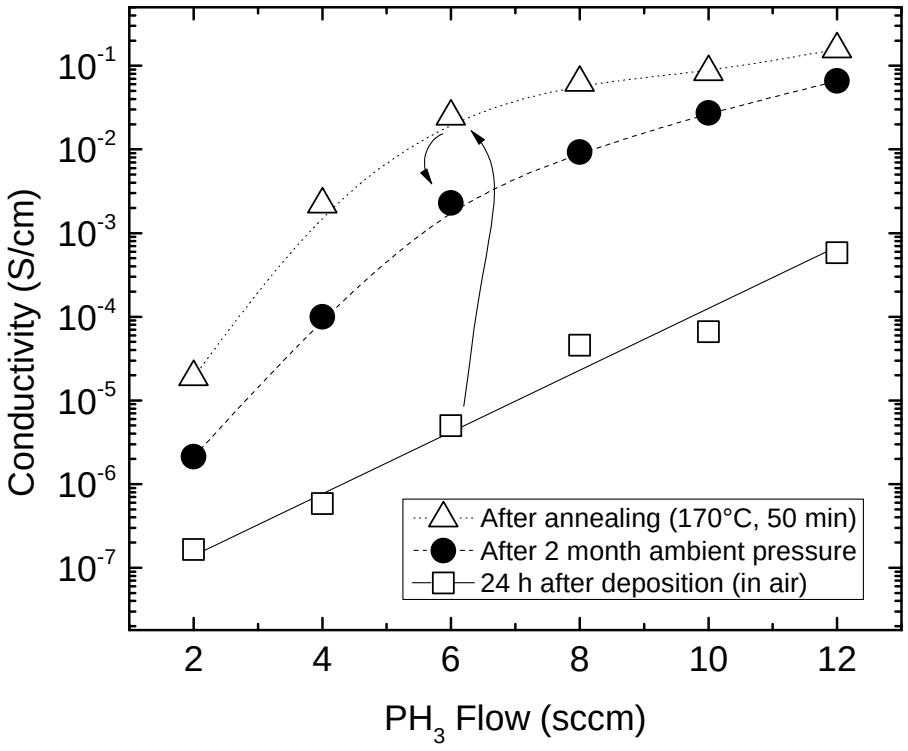

Figure 4.8.: In-plane conductivity of n-μc-SiO_x:H samples deposited with varying PH_3 flow before and after annealing at 160°C for 50 minutes and 2 month storage at ambient pressure. The deposition parameters are the same as in table 4.3.

As can be seen in Fig. 4.8 the conductivity increases by about two orders of magnitude. After two month, the increase compared to the as-deposited measurement is less pronounced, but a significant change remains. This is contrary to the data presented in literature for amorphous n-SiO_x:H [45]. Further observations can be summarized as follows:

- A slight, but far less pronounced effect was observed for μc-Si:H n-layers without

CO_2 admixture (the conductivity increase remained always significantly below a factor of 2).

- The increase in conductivity did not go along with any observable change in the structure as analyzed by Raman spectroscopy.
- Further annealing steps, at 300°C and 400°C showed no further increase in the conductivity. No difference was observed between annealing under air or N_2 atmosphere.
- The gain in conductivity was not affected by the pressure at which the conductivity was measured. Even after 12 h under a vacuum at 1 mPa the gain did not significantly change. Therewith, this effect behaves different than the effects described by Finger et al. for intrinsic μc-Si:H.

So far, the working hypothesis for this phenomenon is an activation of dopants that improve the percolation transport within the layer. The effect described by Finger et al. for very porous intrinsic μc-Si:H (denoted as type I in the reference [164]) is similar and should be considered for further systematic studies on this effect. However, the here observed gain is not reversible upon storage under vacuum as the one reported. The effect of hydrogen effusion reported by Janssen et al. for dpoant activation in a-SiO_x:H seems to be more relevant. Therefore, hydrogen effusion experiments seem to be an appropriate next step combined with studies of the bond distribution (such as X-ray photoemission or infrared spectroscopy) and on the microstructure by for example TEM.

4.6. Summary

Device grade μc-SiO_x:H was deposited by PECVD in the AKT1600 and characterized. The study on the influence of the gas phase composition showed in general very similar results as the ones reported by the Jülich group [11]. Some differences to the influence on hydrogen dilution on material properties reported for layers fabricated by VHF plasmas by the Neûchatel group regarding *HD* were pointed out [10].

The different dependence of the Raman crystallinity of μc-SiO_x:H and pure μc-Si:H on the Si*/H_{alpha} ratio as determined from OES when the RF power is increased were explained by an increasing O-incorporation. The observed improved Raman crystallinity at high deposition pressures is assumingly caused by a lower influence of ion bombardment and/or and increased SiH_4 depletion [149].

The previously reported [25] different influence of the dopant gases PH_3 and TMB on the microstructure and on the conductivity has been systematically analyzed. Here it was shown, that a significant improvement in the conductivity could be reached when the

PH_3/SiH_4 ratio was increased in μc-SiO_x:H by a factor of three compared to <n> μc-Si:H. Based on these findings, a significant increase of the PH_3 flow during the deposition of the IRL at high CO_2 flows yielded a significant improvement on the device level and allowed the fabrication of a-Si:H/μc-Si:H solar cells with stable efficiencies of >11% (compare section 6.4). Comparing the electrical layer properties to the properties in the device, it can be conclueded that the positive influence of a higher PH_3 flow on the device level is even more pronaunced.

A noteworthy change in the conductivity of more than three orders of magnitude of <n> μc-SiO_x:H upon annealing below the deposition temperature was observed that can not be explained by the existing literature on μc-SiO_x:H, μc-Si:H or a-SiO_x:H. Further experiments to investigate the origin of this effect have been outlined.

5. Silicon Carbide

The topic of this chapter are the results regarding the development of microcrystalline silicon carbide (μc-SiC). The chapter is structured as follows: First (section 5.1) a literature overview is given about the material properties, processing and the application in solar cells of a-SiC$_x$:H and μc-SiC$_x$:H. Then, in section 5.2, the experiments and results of the attempts to deposit μc-SiC from SiH_4/CH_4 mixture at high temperatures are being presented. Section 5.3 describes the post deposition crystallization of a-SiC$_x$ layers by means of an electron beam (e-beam).

5.1. Literature

The first report on the deposition of amorphous silicon carbide (a-SiC$_x$:H) was published by Anderson and Spear in 1977 [165]. As mentioned in the beginning, it has a long history in thin film silicon photovoltaics as a window layer with first results published already in the early 1980s [49, 50]. The advantage of a-SiC$_x$:H over a-Si:H is a higher band gap, which can be obtained by carbon incorporation up to a value of $E_g = 2.8\,eV$ [165]. The optical gap usually increases up to $x = 0.5$ and then decreases again for higher carbon content, depending on the deposition method and parameters [166]. Up to today, a-SiC$_x$:H is applied widely as (top cell) p-layer and/or p-i-buffer layer in silicon based p-i-n single and multi junction devices [115, 167]. Typical values for state of the art a-SiC$_x$:H for p-layer application are an optical band gap of $E_{04} = 2.0 - -2.2eV$ and a conductivity of σ = 10^{-6} – 10^{-5} S/cm, the activation energy is usually in the range of 400-500 meV [26].

An overview of the material properties of a-SiC$_x$:H was given by Bullot and Schmidt [166]. Similar to a-SiO$_x$:H, the conductivity drops significantly upon the alloying with carbon and parallel to μc-SiO$_x$:H, the conductivity can be greatly enhanced in materials prepared in such a way that a microcrystalline silicon phase consists in the material [46, 47]. As mentioned in section 2.1.3, two rather different types of materials have to be distinguished here, which are both sometimes referred to as μc-SiC:H in the literature. The one is a mixture of microcrystalline silicon (μc-Si:H) embedded in an amorphous silicon carbide (a-SiC$_x$:H) matrix [46, 47, 168]. The other material contains stoichiometric crystalline silicon carbide and is here denoted as μc-SiC. A schematic diagram of the microstructure of a-SiC$_x$:H, μc-SiC$_x$:H and μc-SiC:H was given in Fig. 2.5. As mentioned

in section 2.1.3, c-SiC has numerous poly types ,depending on its lattice structure, of which the most common ones are 3C-, 6H- and 2H-SiC.

With μc-SiC$_x$:H, n- as well as p-type doping can be achieved with conductivities as high as 10^{-1} for a band gap of $E_{04} = 2.2eV$ (reported for PECVD depositions). With increasing E_{04}, which can be obtained similar to μc-SiO$_x$:H by an increased alloy incorporation (x), the fraction of c-Si diminishes strongly, and the electrical properties approach those of a-SiC$_x$:H [168]. Compared to μc-SiO$_x$:H, μc-SiC$_x$:H is reportedly more difficult to deposit [13], apparently due to the difficulties to further split the precursor radical CH_3 because of its high binding energy. The radical sticks onto the surface and hinders the crystalline growth [169]. Better results for this type of material, have been reported using electron cyclotron resonance (ECR-)PECVD [170, 171]. The advantage here lies in the fact, that the precursor gases are being dissociated in one chamber and are then drawn into the deposition chamber. In this way, higher power densities can be used to dissociate the precursors without harming the growing surface by increased ion bombardment, which inhibits the crystalline growth.

The deposition of microcrystalline silicon containing a crystalline *silicon carbide* phase, denoted here as μc-SiC:H, is desirable for thin film silicon solar cell technology as described in section 2.1.3. c-SiC can be produced for example by the Acheson-process [172] or by sintering [173]. Outside of the thin film technology, c-SiC is widely applied due to its temperature stability and its mechanical strength. Its melting temperature lies above 2300 °C [174]. Epitaxial CVD is possible at temperatures as low as 700°C [175], which is, however, still above the softening temperature of most glass substrates, which are used for thin film silicon solar cells. Another method for the deposition of μc-SiC, which is more applicable and which was already applied in thin film silicon technology is the hot wire (HW-)CVD, which was for example applied by Yu et al. [176], Miyajima et al. [177] or the Jülich group (Klein et al.) [14, 42, 178, 179]. In the first report, conventional precursor gases SiH_4 and CH_4 were used, Miyajima et al. and the Jülich group used monomethylsilane (MMS - SiH_3CH_3) as precursor. Crystallinity was obtained for very high hydrogen dilutions (0.15% MMS in H_2) as Raman spectra and TEM measurements revealed [180]. The resulting material was found to be highly conductive [178] and n-type, which was ascribed to unintentional impurity doping (N, O). The pressure as well as the filament temperature was found to increase the crystallinity, and a minor dependence of the substrate temperature was observed [179]. Microcrystalline silicon n-i-p cells, with a μc-SiC:H n-layer prepared this way, showed reduced parasitic absorption [181]. An overview of μc-SiC:H prepared by HWCVD was given by Finger et al. [42]. The preparation of μc-SiC:H by means of reactive magnetron sputtering in a H_2 atmosphere was also recently reported [182].

The preparation of μc-3C-SiC:H by *PECVD* was also reported by several groups lately:

Rajagopalam et al. described the deposition by the use of diethylsilane ($C_4H_{12}Si$) 0.5% diluted in H_2, He or Ar at varying temperatures with H_2 showing the best results. The crystaline volume fraction as determined from FTIR increased with increasing temperature up to values >0.6 at the highest $T_s = 575C$ with crystallite size in the range of $2 - -10\,nm$ as TEM images indicated. Optical measurements showed remarkably high optical gaps of $E_{04} > 4\,eV$ [183]. Miyajima et al. and the Jülich group showed μc-SiC:H deposition by PECVD using MMS diluted in H_2 with grain sizes in a similar range [184, 185]. Also, the H_2 dilution as well as the deposition temperature was found to be the key parameters for crystalline growth. Optical absorption measurements revealed high optical gaps $E_{04} > 3\,eV$ and enhanced sub-gap absorption for the crystalline material. The sub gap absorption together with the increased dark conductivity up to values of $10^{-3}\,S/cm$ was (similar to the HWCVD layers) ascribed to the unintentional incorporation of O- and / or N-dopants. Also, the existance of hexagonal SiC was reported by Nuys [185].

5.2. SiC Depositions

Based on the presented findings in the literature, it seemed feasible to deposit μc-SiC$_x$:H and/or μc-SiC:H on the VAAT-tool for the possible application as window layer for both the a-Si:H/μc-Si:H and/or the poly-Si cell. The high temperature stability of μc-SiC:H known from applications outside of the thin film technology makes this material especially desirable in view of the crystallization experiments for the poly-Si absorber layers. To contribute to the scientific progress, a deposition using conventional, low-cost precursor gases was chosen to complement the advances achieved using MMS.

5.2.1. Influence of Deposition Power and Pressure (low Temperature)

First experiments were performed on the basis of the best known method for depositing μc-Si:H at the VAAT-tool. From this recipe, small amounts of CH_4 were added to the gas phase to obtain μc-SiC$_x$:H. The deposition parameters are given in table 5.1. Fig. 5.1 shows the Raman spectra of two layers, one deposited with and one without 2 sccm CH_4 admixture (0.3% of the total flow) in the gas phase. As can be seen, the crystalline volume fraction completely vanishes upon the addition of this amount of CH_4.

From literature, it was known, that very high hydrogen dilutions were necessary to cover the growing surface sufficiently with atomic hydrogen and to obtain a crystalline SiC phase [185]. Due to hardware constraints set by the mass flow calibrators (MFCs), no further increase in the hydrogen dilution HD =(H_2)/(SiH_4+CH_4+H_2) was possible for this SiH_4/CH_4 ratio. However, from literature [90] as well as from simultaneously conducted experiments on the deposition of μc-SiO$_x$:H (see section 4.3, it was known that by apply-

Table 5.1.: Deposition parameters for the study of the gas phase composition of μc-SiC$_x$.

SiH4 (sccm)	H_2 (sccm)	CH_4 (sccm)	T (°C)	P (mW/cm^2)	p (kPa)	$d_e l$ (mm)
5	600	2	244	350	0.3	12

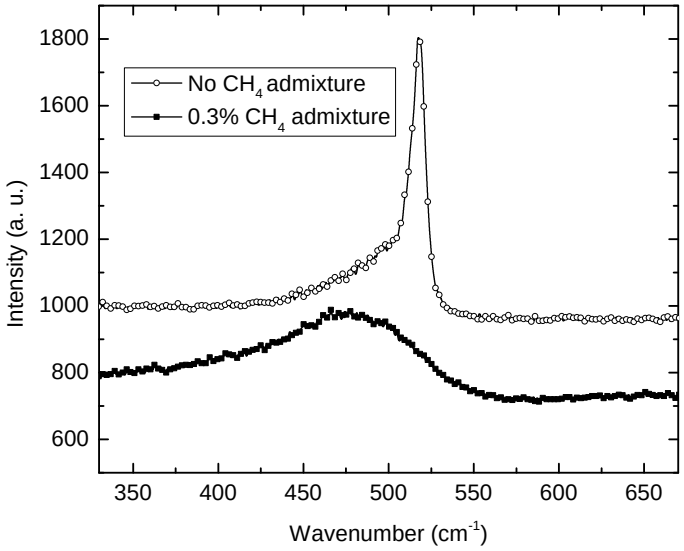

Figure 5.1.: Raman spectra of a μc-Si:H layer deposited at a pressure of 0.7 kPa and an RF power of 350 mW/cm^2 and the same layer with an admixture of 0.3% CH_4 in the gas phase.

ing a high pressure high depletion regime, the amount of available atomic hydrogen on the surface can be greatly enhanced due to the suppression of hydrogen annihilation (see section 2.3). Therefore, variations of the deposition power and pressure were performed, based on the recipe given in 5.1. The layers were characterized by reflection and transmission measurements and by Raman spectroscopy. The results of the optical measurements are given in Fig. 5.2.

It can be seen that with an increasing power to pressure ratio (P/p), the films become more transparent and the refractive index decreases, which indicates an increase in carbon incorporation. This is in agreement with literature [166] and can be explained by the higher binding energy of the CH_4 molecules in comparison to the SiH_4 molecule. The power dependence seems also similar to results obtained from μc-SiO$_x$:H depositions (see section 4.3). When looking at the deposition rate, one can observe that it is almost independent of the RF power and dominated by the pressure up to 0.7 kPa. An explanation for the behavior below 0.7 kPa can be that the residence time of the molecules in the reactor is the limiting factor. Above 0.7 kPa on the other hand, the limiting factor seems

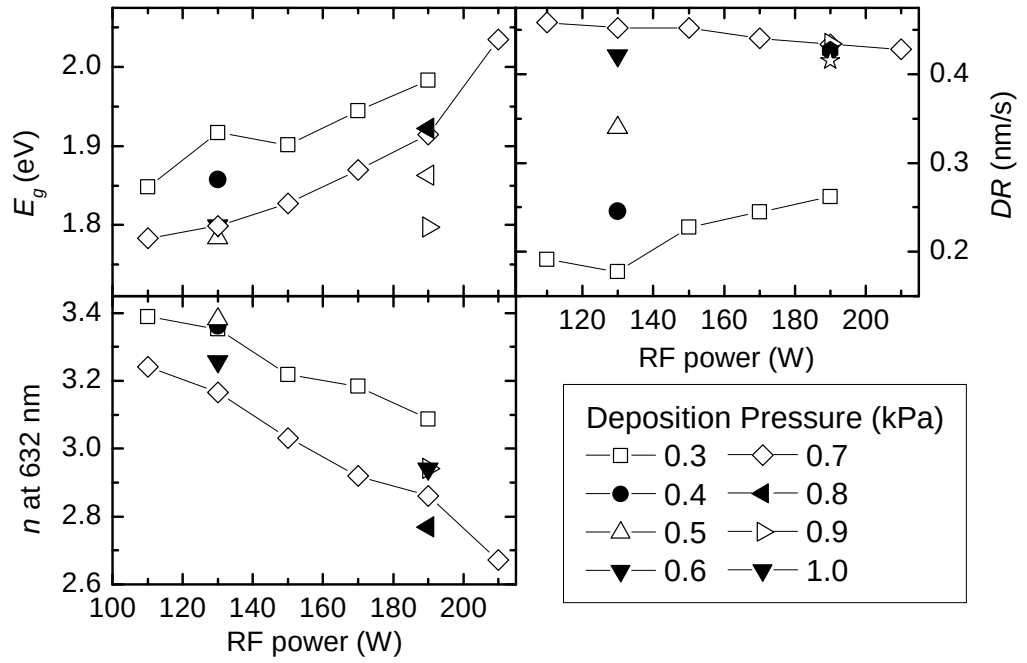

Figure 5.2.: The results of the spectrophotometry measurements of the SiC samples deposited at low temperature under high hydrogen dilution, E_g (top left), deposition rate (top right) and refractive index at 632 nm (bottom left), as functions of deposition power for various pressures.

to be the gas supply as no dependence on either P or p can be observed. Thus, the gas depletion should be high. However, even under these probably favorable conditions for crystalline growth, no significant change in the Raman spectra from the one shown in Fig. 5.1 was observed. No further experiments regarding the deposition of μc-SiC$_x$:H were performed, as the focus was on μc-SiC:H. However, it is believed that a high depletion regime is also favorable for this material, as the HWCVD depositions reported by Klein et al. indicated. Here, also high pressures as well as high dissociation rates (obtained through high filament temperatures) improved the crystallinity, which should be due to the suppression of the hydrogen annihilation [14].

5.2.2. Influence of Gas Phase Composition

To obtain μc-SiC:H, it was a working hypothesis that a stoichiometry of silicon to carbon atoms near unity is favorable. As shown in literature [166], in the previous section and in section 4.3, not only the precursor gas ratio determines the film stoichiometry, but also the power per pressure (P/p) ratio and most likely also the hydrogen dilution ratio, due to selective etching. Therefore, the aim of the next experiment was to deposit films near stoichiometry. As a figure of merit for the C-content, the refractive index was chosen.

As the H_2 as well as the CH_4 flow were constrained by the MFCs, the SiH_4 flow was sys-

tematically altered between 5 and 0.5 sccm based on the parameters given in table 5.1 to alter the stoichiometry. By doing so, not only the precursor ratio Φ_{CH_4} = CH_4/(SiH_4+CH_4) ratio is changed from 31% to 84%, but also *HD* from 75 to 171, which has to be kept in mind. For comparison, the hydrogen dilution reported in literature where transition from amorphous to microcrystalline growth occured lay about a factor of 5 higher at 833 in the data shown in Ref. [185]. To compensate this, the deposition pressure was kept at 0.7 kPa and the RF power density at 350 mW/cm^2 to assure a high degree of gas depletion. For the sample with 0.5 sccm SiH_4, the CH_4 flow was also increased to 3 sccm for later experiments. The results of the parameters extracted from fitting the reflection and transmission spectra of the resulting layers are shown in Fig. 5.3. As can be seen, the

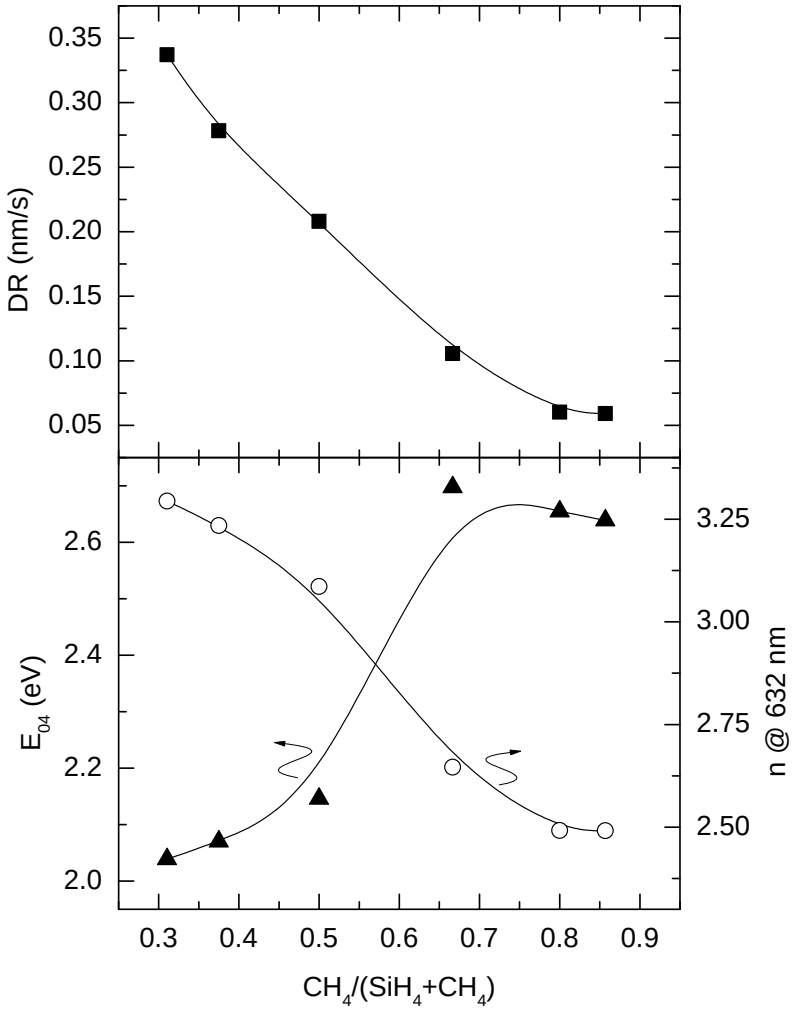

Figure 5.3.: Deposition rate, E_{04} and refractive index n at 632 nm as a function of gas phase composition for the SiC samples deposited at 244°C and high hydrogen dilution.

deposition rate decreases almost linearly with Φ_{CH_4} due to the lower SiH_4 flow, which confirms the high degree of gas depletion. The optical gap E_{04} increases with increas-

ing Φ_{CH_4} up to a value of 67% and then decreases again slightly. In the a-SiC$_x$:H review given by Bullot and Schmidt, the maximum optical gap as a function of carbon content can differ from 50% depending on the deposition method used [166]. The refractive index decreases monotonously down to values near 2.5.

The Raman spectra of three different samples prepared with Φ_{CH_4} = 31%, 38% and 50% are depicted in Fig. 5.4. With increasing Φ, one can observe the development of two broad features at 767 cm^{-1} and 950 cm^{-1}, which indicate an increasing amount of Si-C bindings and might be related to the TO and LO mode of SiC. However, compared to the Raman spectra reported in literature, where a high degree of crystallinity was confirmed by more direct measurements such as transmision electron microscopy or x-ray diffraction spectroscopy, it is expected that only little amounts of small crystallites are present in the layers. For higher Φ_{CH_4} values, the Raman spectra were superimposed by a broad feature of what seemed to be photoluminesence and no conclusions on the types of bindings in these sample could be drawn. This superimposition of the Raman spectra for SiC samples was also observed by M. Nuys [185].

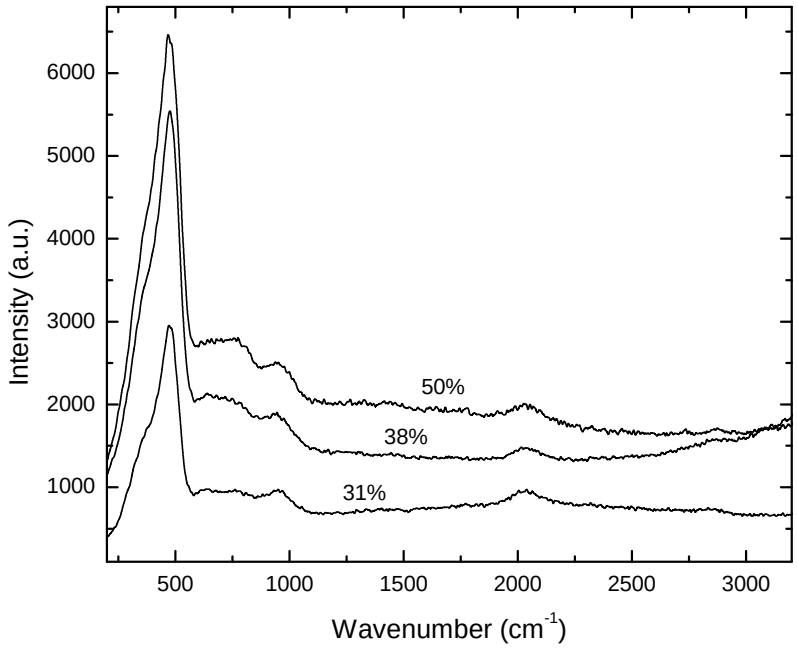

Figure 5.4.: Raman spectra of three different SiC samples deposited with varying Φ_{CH_4} flow at 244°C and high hydrogen dilution.

5.2.3. Influence of Substrate Temperature

In the previous section, the influence of the gas phase composition on the SiC layers was studied. Raman spectra indicated an increased amount of Si-C bindings at high hydrogen

dilutions and low Φ_{CH_4} ratios. However, no or only a little degree of crystallinity was achieved. From literature it was known that high substrate temperatures can increase the crystallinity of the layers by enhancing the surface diffusion length [185]. Therefore, in the next step, SiC layers were deposited at varying substrate temperatures from 244 – 400°C. The results of the optical analysis are shown in Fig. 5.5.

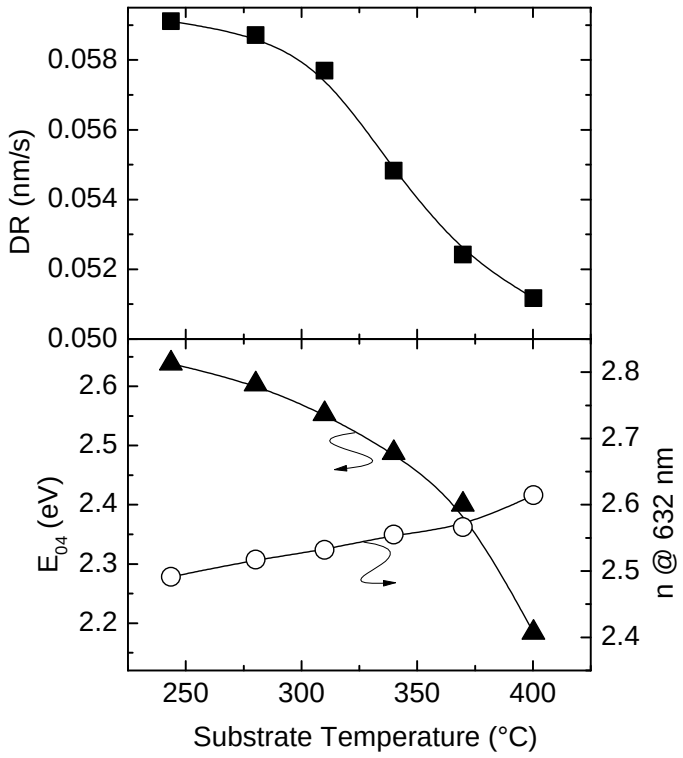

Figure 5.5.: Deposition rate, E_{04} and refractive index n at 632 nm as a function of substrate temperature.

With increasing substrate temperature, it can be observed that the deposition rate decreases. This is in agreement with data shown by [185] and can be explained by an increasing desorption from the surface. The optical band gap E_{04} decreases with increasing temperature, which is usually ascribed to a lower hydrogen content of the layers. As the refractive index increases, also a variation in the stoichiometry towards higher carbon contents could be imaginable. Fig. 5.6 shows the Raman spectra of the temperature series. A broad feature arises near 1500 cm^{-1}, which can be attributed to existence of graphite in the layer. The feature at 767 cm^{-1}, which can be attributed to Si-C bonds and which can be seen in the inlet of Fig. 5.6, did not increase significantly, assumingly due to the low Si content at this precursor ratio.

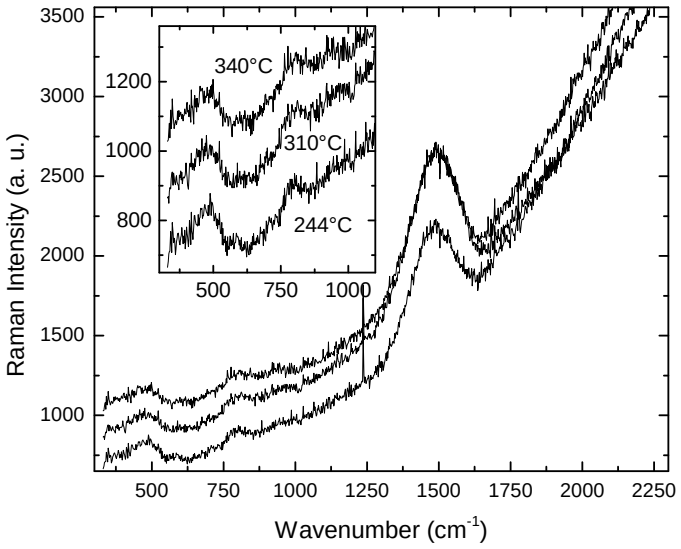

Figure 5.6.: Raman spectra of the temperature series deposited at maximum hydrogen dilution

5.2.4. Influence of Deposition Power and Pressure (high Temperature)

The increase of temperature, which was presented in the previous section, did not yield a significant gain in the amount of SiC in the layer as the Raman spectra indicated. A further variation of the deposition power and pressure was performed in the next step. Fig. 5.7 shows the evolution of E_{04}, n at 632 nm and the DR as power density increases from $0.25 - 0.73\,\mathrm{W/cm^2}$.

At 0.7 kPa, the deposition rate increases with increasing RF power up to $0.55\,\mathrm{mW/cm^2}$ and then remains at a value near 0.06 nm/s. At the same time decrease E_{04} and n. Under the assumption that the layers are already carbon rich at the lowest power density, the trend can be explained by an increase in carbon incorporation. A decrease in pressure at $0.73\,\mathrm{mW/cm^2}$ yields an increase in the deposition rate, which is a surprising behavior. Compared to the power and pressure variations performed earlier at a similar range but a lower substrate temperature and higher SiH_4 flows, the observed trends are fundamentally different: The deposition rate and its dependence on the RF power does not indicate the high depletion observed in the low temperature experiments. This can be partially attributed to the high degree of desorption from the surface due to the high temperature.

Fig. 5.8 depicts the Raman spectra of exemplarily layers from this series. The spectra are dominated by the peak at $1560\,\mathrm{cm^{-1}}$, which can be attributed to the existence of C-C bonds in the graphite structure. The shoulder at $1350\,\mathrm{cm^{-1}}$ can be attributed to the existence of C-C bonds in a diamond structure.

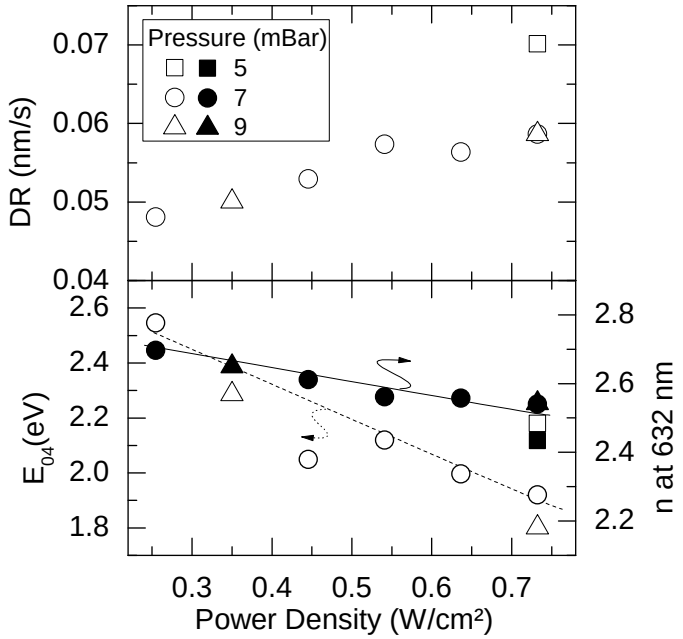

Figure 5.7.: Deposition rate, E_{04} and refractive index n at 632 nm as a function of RF power for varying pressures at 400°C. Layers were deposited with high hydrogen dilution.

5.2.5. Summary

It can be summarized that the presented experiments regarding the fabrication of μc-SiC:H by the high pressure high depletion method did not lead to the desired high crystallinities. In the presented experiments, a large parameter room were characterized using Raman spectroscopy and spectrophotometry. The presented data might be useful as a basis for further experiments. The previous chapter about the deposition of silicon oxide layers, has shown that rather small variations in the deposition parameters can change the film properties significantly. It is believed that the presented approach using high pressures to increase the residence time and high power densities to reach a high degree of dissociate can lead to successful deposition of μc-SiC, also from SiH_4/CH_4 gas mixtures. The last experiments suggest that the layers were carbon rich. A decrease of the methane flow combined with an increase in hydrogen dilution could be a next step. Also the influence of the reactor volume (by varying the electrode distance) and further increase the residence time seems to be interesting. Upcoming experiments should be accompanied by further characterization methods including infrared spectroscopy on the films as well as *insitu* plasma diagnostics.

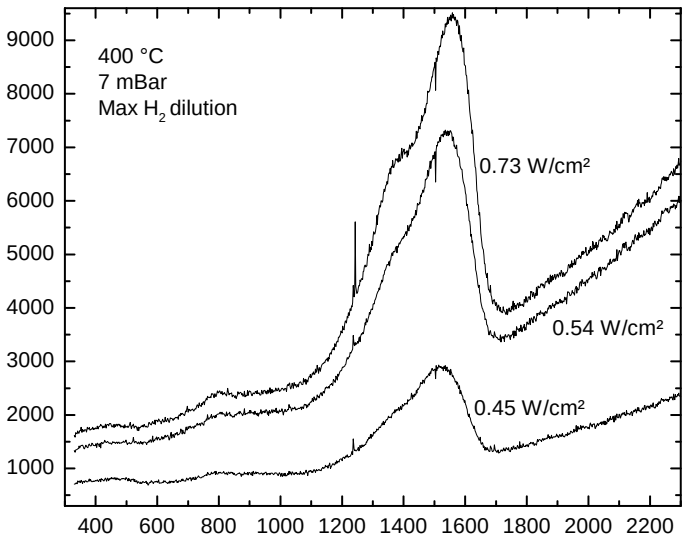

Figure 5.8.: Raman spectra of the SiC power variation series at 400°C substrate temperature.

5.3. E-Beam Crystallization

Parallel to the experiments presented in the last section regarding the deposition of μc-SiC by PECVD, the crystallization of a-SiC$_x$:H layers by means of an electron beam (e-beam) were investigated. The crystallization of a-SiC$_x$:H layer by means of *laser* were previously shown by Palma et al. [186, 187] and Urban et al. [188]. It was found that depending on the as deposited stoichiometry, the crystallization experiments resulted either in the formation of c-Si, for Si-rich samples, c-C for C-rich samples or c-SiC for films close to stoichiometry ($x = 0.48$). Thus, for the experiments conducted for this thesis, layers with varying stoichiometry were deposited with a thickness of 60-80 nm, at a high substrate temperature ($T_s = 400C$) to minimize hydrogen incorporation into the film. The layers were characterized as-deposited using optical measurements and Raman spectroscopy. The deposition parameters and the results of the optical measurements are summarized in table 5.2. The refractive index can be used as a measure for the stoichiometry.

Prior to the crystallization with the e-beam the samples were annealed at a temperature of 400°C under nitrogen atmosphere for 4h to reduce the remaining hydrogen content. The crystallization was performed on $1 \times 5\,\mathrm{cm}^2$ sample sizes in steps using varying energy fluxes as depicted in Fig. 5.9. For the coupling of the e-beam, the edges were prepared with a conductive graphite solution as explained in section 3.1.3. The constant movement speed and the step wise increased energy flux of the e-beam resulted in 9 areas of differently crystallized material of the same size (approximately $6 \times 10\,\mathrm{mm}^2$). After the crystallization, the layer thickness was determined using the optical procedure described

Table 5.2.: Deposition parameters for the E-Beam crystallization experiments, other parameters remained fixed at $T_s = 400C$, $p = 0.3\,kPa$, $d_{el} = 15\,cm$, no H_2 dilution was used.

SiH_4 sccm	CH_4 sccm	P density W/cm^2	DR nm/s	E_{04} eV	n at 632 nm
20	**40**	0.13	1.14	1.75	3.55
15	**60**	0.13	1.02	1.76	3.28
12	**72**	0.13	0.92	1.90	2.95
12	72	**0.19**	1.10	2.40	2.45
12	72	**0.26**	1.13	2.49	2.40

in section 3.2.2 at the different areas. The thicknesses were normalized to the as deposited values and plotted against the energy flux in Fig. 5.9.

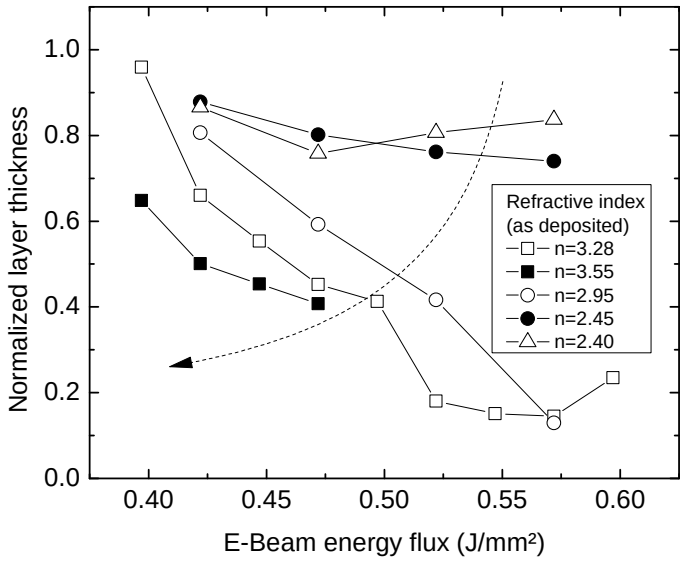

Figure 5.9.: Normalized thickness of the e-beam crystallized samples versus the e-beam energy flux.

In all cases the thickness was reduced. The layers with a low refractive index in the as deposited state (i.e. carbon rich) showed macroscopic cracks, but in general a lower thickness reduction than the silicon rich samples. The cracks could be related to a high degree of stress in the layer upon crystallization. For these samples, the energy flux steps were clearly visible by eye as the areas were obviously more transparent, which was ascribed to the lower thickness. Raman measurements were performed on the different areas. Selected spectra are depicted in Fig. 5.10 for three exemplarily samples: Si-rich

($n = 3.55$), near stoichiometry ($n = 2.45$) and C-rich ($n = 2.40$) (compare table 5.2).

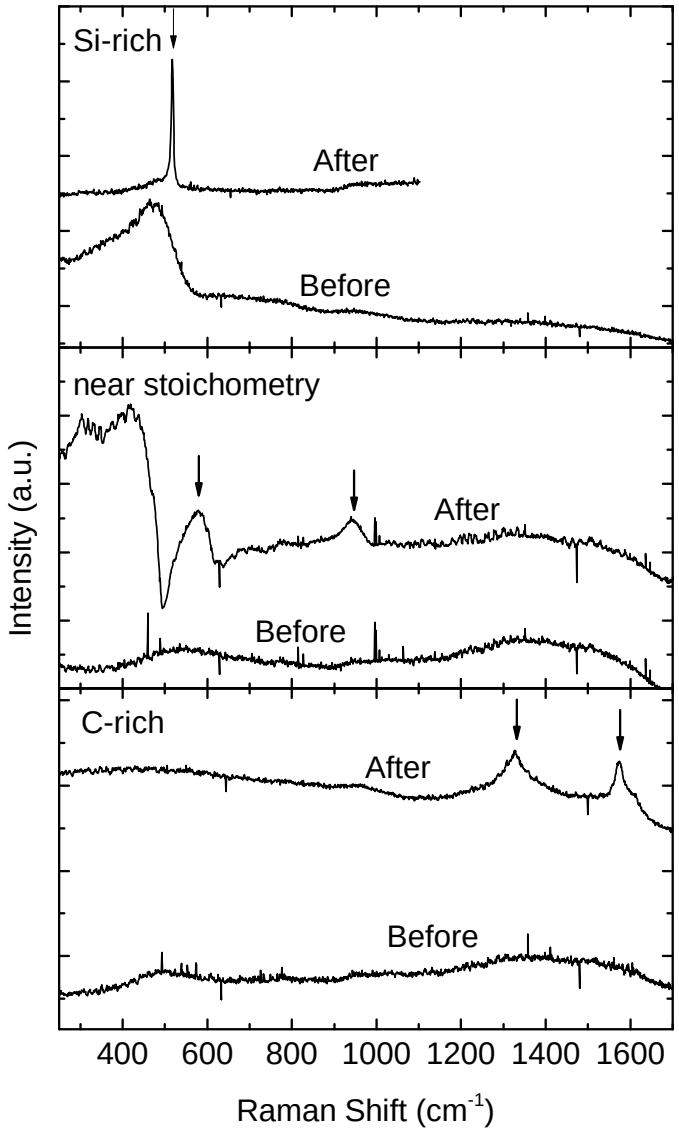

Figure 5.10.: Raman spectra of selective samples before and after e-beam crystallization. The spectra are shifted in altitude to allow a better presentation.

The Si-rich sample (top part Fig. 5.10) shows a clear change after the crystallization from amorphous to crystalline silicon. The presented sample was crystallized with $0.4\,\mathrm{J/mm^2}$, for higher e-beam energies, the signal vanished, assumingly due to the lower sample thickness. The sample with n=2.45 as deposited (middle part Fig. 5.10), revealed the most promising Raman spectra with a peak at $942\,\mathrm{cm^{-1}}$ wavenumber, which could be the longitudinal optic mode of SiC (nominally $950\,\mathrm{cm^{-1}}$). The peak at $580\,\mathrm{cm^{-1}}$ could not be clearly assigned yet. The area from which the spectra was measured was crystallized using a higher energy flux of $0.55\,\mathrm{J/mm^2}$. For other energy fluxes in this range, similar

peaks were found, partly shifted to higher wavenumbers, which could be an indication of 4H-SiC, which has its longitudinal acoustic mode at 610 cm^{-1}. The peak shift is another indication for the high degree of stress in the layer. It can be said, that these peaks were only observed in samples that were crystallized using high energy fluxes >0.5 J/mm^2. Due to the cracking of the material at these high energy densities, the material appeared to be very heterogeneous with amorphous and crystalline regions close to each other. The C-rich sample (bottom part Fig. 5.10) exhibited the existence of a crystalline carbon phase with peaks at 1330 cm^{-1} and 1560 cm^{-1}.

5.4. Summary

First experiments regarding the deposition of crystalline silicon carbide were conducted at the VAAT using the high pressure depletion method combined with high temperatures. The resulting films showed no signs of a high c-SiC fraction. However, the collected data can be a basis for further experiments, which were outlined in section 5.2.5.

The first experiments regarding the crystallization of a-SiC_x:H layers by means of an e-beam showed promising results, which are in accordance to results published by Palmer et al. on the crystallization behavior of a-SiC_x:H layers using an excimer laser. They can be summarized as follows: Si-rich samples ablate with increasing e-beam energy flux and show already for low energy fluxes purely c-Si Raman spectra. With increasing C-content, the ablation decreases but the formation of cracks appear, which are probably related to a high degree of stress induced by the partial crystallization of the layer. The appearance of crystalline SiC phases occurred only in the samples that were near stoichiometry. The SiC phase seems to be very strained, which results in shifted Raman modes and macroscopic cracks. The appearance of SiC crystallites has to be eventually confirmed by TEM imaging. A second series (not shown) aiming to reproduce the shown results and increase the resolution concerning this apparently rather narrow process window, gave similar results. A third series, aiming to test the influence of the substrate, the layer thickness and the influence of a wetting layer has already been started.

6. Solar Cells

In this chapter the development of a-Si:H/μc-Si:H tandem solar cells with μc-SiO$_x$:H intermediate reflectors layer (IRL) is described. The first solar cells, which were deposited with an IRL suffered from an increased series resistance due to a poor performance of the tunnel recombination junction (TRJ), which is a fundamental limitation to the functioning of the IRL. Therefore, the first section (6.1) is dedicated to the development of a low ohmic TRJ. The theoretical background of tunnel contacts is briefly summarized and a model for the quantitative description of the transport in tandem and multi-junction solar cells with TRJs incorporating IRLs based on semi conductor principles is presented. For the simulations, the program AFORS-HET was used, which is a tool specifically designed for the simulation of hetero junctions. The code was extended by two models that will be described in the text to account for the tunneling process in the TRJ [189, 190] Based on this model, an Ansatz was proposed how to improve the solar cells. The second section (6.2) is dedicated to the implementation of a μc-SiO$_x$:H bottom cell p-layer and its influence on the open circuit voltage (V_{oc}). As soon as a working TRJ was implemented into the device, the optimization of the IRL itself was possible. Therefore, in section 6.3, the optimization of the IRL with respect to the TCO topography and light trapping is analyzed. In the final section 6.4, the stability of the solar cells with IRL is described and the best stable solar cells are presented. The evolution of the layer stack, of which the TRJ consists, and the connotation used in the following is shown in Fig. 6.1. Part of the results regarding the optimization of the tunnel recombination junction were published in [190].

6.1. Improved Tunnel Junctions with μc-SiO$_x$

The functioning of the tunnel recombination junction (TRJ) in amorphous silicon based multi-junction cells is a fundamental necessity to achieve high efficiencies. Experimental evidence that tunneling is the dominant transport mechanism at the n-/p-junction in tandem cells has been given by Hegedus et al. from temperature dependent conductivity measurements on tunnel devices [191]. A complete theoretical model for the transport in the n-/p-junction and in tandem devices has been first given by Willemen and Zeman et

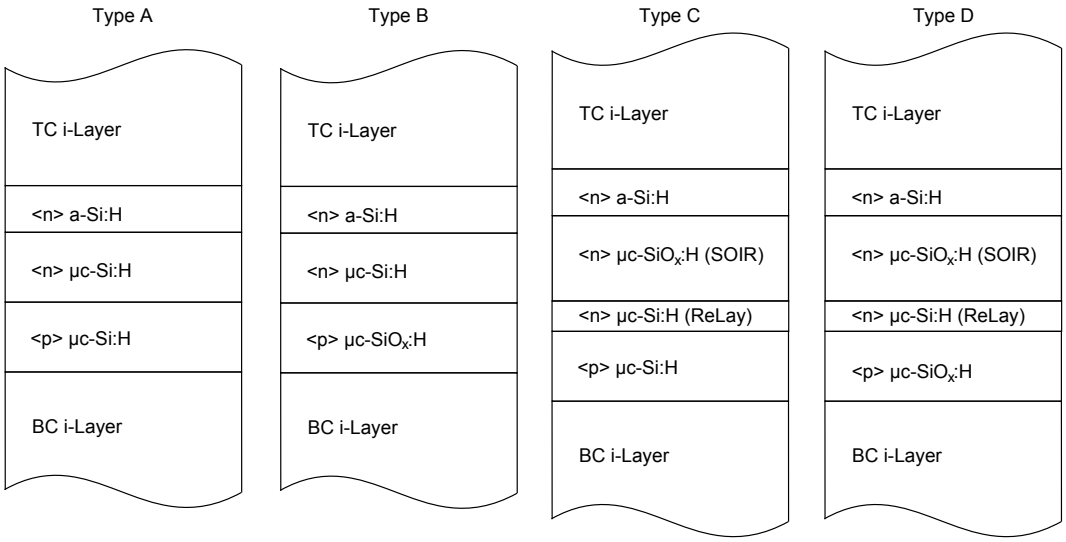

Figure 6.1.: Evolution of the Tunnel Recombination Junction (TRJ) during the Cell Optimization

al. [60, 192, 193]. The model uses the trap-assisted tunneling (TAT) model, also known as the Hurkx-Model [194, 195]. In the simulation of devices based on amorphous and microcrystalline silicon, it is common to assume that recombination is predominantly via trap states, so called Shockley-Read-Hall recombination (SRH) [26]. The basic idea of the TAT is that electrons from the conduction band of the n-layer and or holes from the valence band of the p-layer tunnel into trap-states close to the n-/p-junction. At the trap state, the probability for recombination is much higher and thus the recombination rate increases significantly [196, 197]. However, a good description of the I-V characteristics of tandem cells with realistic values for amorphous silicon was only possible with either the implementation of a recombination layer with a high defect density and graded band gaps in the adjacent doped layers, which was proposed by Hou et al. [198], or by the implementation of the so called field and temperature dependent mobility model (FTM) suggested by Willemen et al. [192]. The FTM model is based on findings by Juska et al. that the mobility increases under heavy electric fields by several orders of magnitude following an exponential dependency [199] according to

$$\mu_{eff} = \mu_0 \cdot exp\left(\frac{|F|}{F_0} = \mu_0\right) = \mu_0 \cdot exp\left(\frac{eAF}{kT_F}\right)^{1}. \tag{6.1}$$

Here, μ_{eff} and μ_0 are the initial and effective mobilities, F is the local electric field, F_0 is a constant describing the field dependence (typically assumed to be in the order of $10^5\ V/cm$) and A and T_F are alternative values describing the field and temperature de-

[1] The first expression is the mere field dependence as proposed by Willemen et al. [192] and which is implicated in AFORS-HET, the second is a generalization presented in [196], which includes the temperature dependence

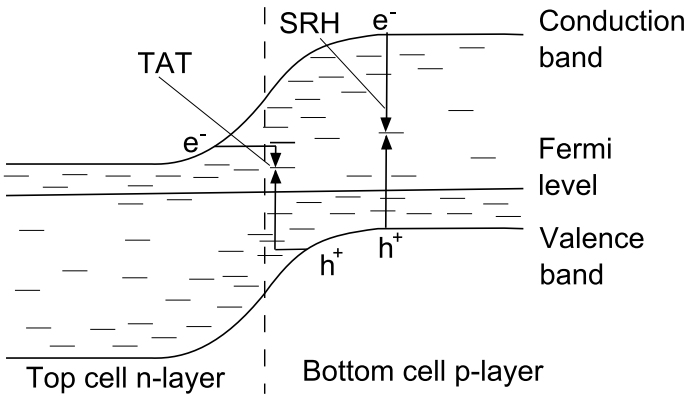

Figure 6.2.: A schematic band diagram of a tunnel recombination junction. The trap-assisted tunneling (TAT) as well as the conventional Shockley-Read-Hall mechanisms are denoted.

pendence (a further explanation is given in ref. [196]. A detailed overview of tunneling in a-Si junctions including the described models and further mechanisms such as Poole-Frenkel barrier lowering is described in [200]).

With respect to the material properties, this model suggests that the activation energies E_a of the both adjacent doped layers are ideally close to zero. This (a) increases the band bending, which (a_0) reduces the way the charge carriers have to tunnel and therewith the tunnel probability and (a_1) increases the effective mobilities according to equation 6.1 and (b) reduces the energetic loss through recombination (iso-energetic recombination). For, μc-Si:H doped layers E_a is low, resulting in a potential difference at the n-/p-junction of around one electron volt assuming a band gap of 1.1 eV. Assuming this potential drop is across less than 10 nm the electric field can be in the order of 10^5 V/cm and thus the application of the FTM model seems justified.

6.1.1. First Experimental Results

Before the development of μc-Si:H doped layers, the main problem in the technical realization of low ohmic tunnel contacts in a-Si:H based multi junction cells was the low doping efficiency and the resulting high activation energy of the amorphous material. Much research had been conducted in the 1980s and 1990s regarding this topic. The possibility to improve the tunnel recombination junction by the implementation of metal-oxides was proposed by Sakai et al. [201]. Alternatively, the use of μc-Si:H doped layers has proven to considerably reduce the series resistance of the devices [191, 202] and has led to the first stable efficiencies of above 12% for an a-Si:H/a-SiGe:H/a-SiGe:H triple cell [39].

In a-Si:H/μc-Si:H tandem cells without an intermediate reflector or one consisting of a TCO such as ZnO:Al, the problem is not severe due to the low activation energy of layers

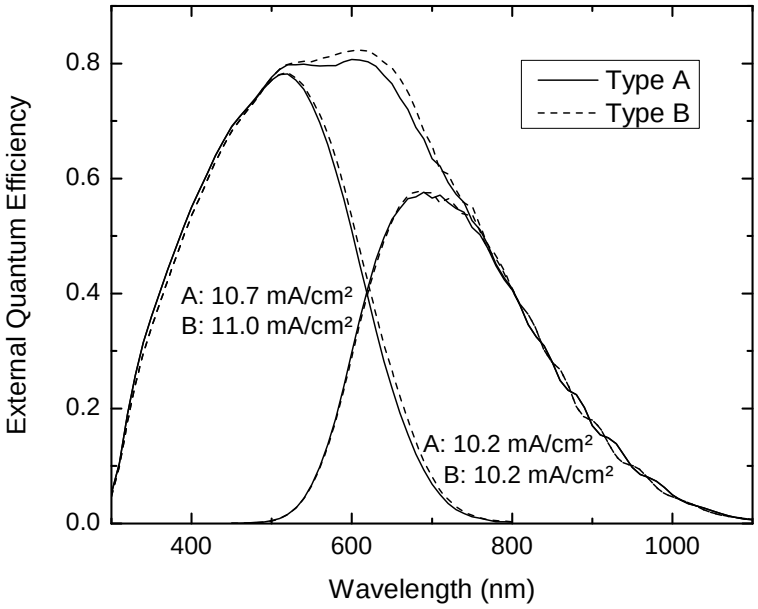

Figure 6.3.: The external quantum efficiency of two representative cells with tunnel recombination junctions of type A and type B, i.e. the introduction of μc-SiO$_x$ in the bottom cell p-layer. The cells were deposited on SnO$_2$:F. The i-layer thicknesses were 300 and 1600 nm.

adjacent to the TRJ. However, the use of μc-SiO$_x$:H within the TRJ as a material for the *in situ* IRL or just to reduce parasitic absorption has renewed the interest in the TRJ, as one can typically observe that the TRJ suffers with high O-contents in these layers [10, 89]. In the following it will be shown that the implications of the described models developed for a-Si:H/a-Si:H tandems can be transferred to a-Si:H/μc-Si:H cells with μc-SiO$_x$:H doped layers in the TRJ as well.

From the model point of view, the replacement of an amorphous with a microcrystalline doped layer at the TRJ leads to a sharper n-/p-contact: The distance between the Fermi-energy E_f and the conduction band energy E_c (for <n> μc-Si:H) or valence band energy E_f(<p> μc-Si:H), respectively, is in microcrystalline layers several 100 meV lower than in amorphous materials [20]. Thus, the potential difference between n- and p-layer becomes higher and the electric field, which is equivalent to the gradient of the potential, is higher, which leads to the described positive effects.

First experiments dedicated to the implementation of the silicon oxide intermediate reflectors were conducted after the implementation of the μc-SiO$_x$:H p-layer (TRJ type B). This p-layer can, strictly speaking, also be considered as an intermediate reflector [154]. However, as shown in section 4.4, boron doped μc-Si:H films achieve systematically lower crystallinities than phosphorous doped films and, accordingly, lower refractive indices can be reached for optimized n-type μc-SiO$_x$:H films. In the experiments changing the TRJ from type A to type B, i.e. the introduction of μc-SiO$_x$ bottom cell p-layer, the top cell

current increased by about 0.3 mA/cm^2 as presented in Fig. 6.3, (the cells were deposited on SnO_2:F). The increase in top cell current can be attributed to the intermediate reflector effect induced by the p-layer. In this configuration, the p-layer has a refractive index of 2.7 at 632 nm wavelength. Layers with lower refractive index fabricated with a higher CO_2 dilution in the gas phase resulted in cells with increased series resistance. A further optimization was not performed since more potential was believed to lie in the implementation of the μc-SiO$_x$:H n-layer for the mentioned reasons. As can be seen in Fig. 6.3 the increase in top cell current does not coincide with a decrease of total current. That means the additional current originated from a reduction of parasitic absorption in the p-layer, which can be attributed to the increased band gap (E_{04} of the p-layer increased from 2.0 to 2.2 eV). Besides these optical improvements, the cells fabricated with type B TRJ also show an increased open circuit voltage (V_{oc}) of typically 10 – 20 mV. This point will be discussed in the next section.

To further increase the top cell current, the implementation of a μc-SiO$_x$:H n-layer acting also as intermediate reflector with an accordingly increased thickness and with a refractive index much lower than the one of the new bottom cell p-layer (BCp) was desirable. The advantage of such a highly reflecting layer is, as it should be pointed out and was described in section 2.2.2, usually only an increase in top cell current. The effect of the total current is highly dependent on the topography of the used TCO (see section 6.3). Lambertz et al. and Pellation Vaucher et al., however, also mention cases where the total current increases, due to the fact that the light trapping is improved with an IRL [11, 76]. In all cases, the bottom cell current is reduced by the implementation of the IRL, which has an effect on current matching and thus the fill factor. Typically, the bottom cell has to be increased to completely profit from the IRL. However, since slightly bottom limited cells are typically more stable against LID than initially matched or top limited cells [99], the *stable* efficiency can profit from the IRL also without a thickness increase of the bottom cell i-layer.

The TRJ with the IRL and the problem with the R_{oc}

As mentioned in the beginning, the first experiments with the IRL showed a significant increase in the series resistance as determined from light I-V *(R_{oc})* and thus in *FF* and conversion efficiency. The R_{oc} was found to be the best parameter to quantify the electrical quality of the TRJ as it is less dependent on the current matching than the *FF*. Representative I-V curves of cells with different TRJs are shown in Fig. 6.4. The typical characteristics of a cell with a TRJ that is not working properly can be seen in the case of the I-V curve of the cell with the two oxidic layers deposited right on top of each other: The curve shows an s-shape, which is a clear indication for the formation of a potential barrier at the TRJ. Several measures were tested to improve the TRJ including an increase of dopant

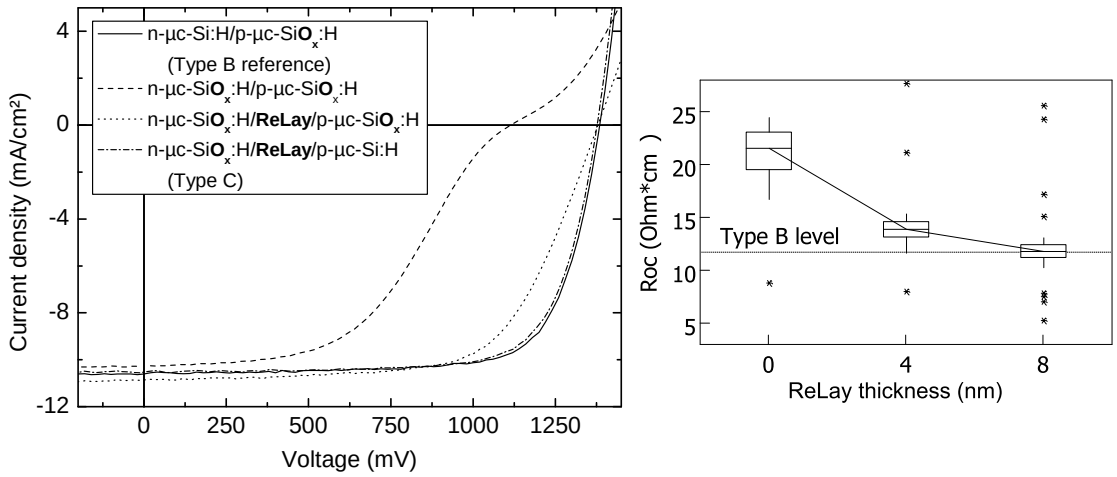

Figure 6.4.: (Left) The I-V curves of four cells with different TRJs: type B (straight line), μc-SiO$_x$ n- and p-layer without μc-Si:H recombination layer (dashed line), with ReLay (dotted line) and type C TRJ (dashed-doted line)(i.e. μc-SiO$_x$ p-layer replaced by the non oxidic μc-Si bottom cell p-layer). (Right) Box plots (based on 20 cells) of the R$_{oc}$ as a function of ReLay thickness. The dashed line indicates the reference R$_{oc}$, with type B TRJ for comparison.

dilution, an increase of H_2 dilution, a lower deposition pressure, an increased seed layer thickness and the deposition of an additional <n> μc-Si:H recombination layer (from now on referred to as *ReLay*) of varying thickness, of which the most successful measure was the introduction of the ReLay and the lower deposition pressure. The deposition of the ReLay was motivated, as mentioned, from ideas published regarding the improvement of a-Si:H/a-Si:H tandem cells [191, 196]. The curve of a cell with the ReLay deposited between the two oxidic layers is also shown in Fig. 6.4. As can be seen, the s-shape characteristic vanishes and the R$_{oc}$ decreases significantly. However, only the replacement of the μc-SiO$_x$ with the non-oxidic p-layer (this is equal to type C TRJ) gave an R$_{oc}$ similar to cells with TRJ of type B. In the following section 6.1.2, the role of the ReLay and the BCp will be discussed in the perspective of the model Ansatz in more detail.

Cells were deposited with the new TRJ of type C with a thicker bottom cell i-layer of 1850 nm instead of 1600 nm (top cell i-layer thickness was 270 nm) to compensate the optical losses due to the higher total reflection induced by the new TRJ. The IRL had a thickness of 60 nm. The results of the best runs of each type are shown in Fig. 6.5. As can be seen, the cells with TRJ of type C are initially slightly worse than the type B cells. This is mainly due to a lower V_{oc} of about 10 – 20 mV, which was found to be typical for type C cells as well as type A cells, as mentioned above, and therefore is ascribed to the oxidic bottom cell p-layer (see section 6.2 for a discussion of this problem). J_{sc} is higher for the cells with the IRL (type C), which can be ascribed to the higher top cell current, as cells with type B TRJ were top limited as can be seen from the EQE for the given i-layer thicknesses. The higher top cell current is clearly due to the reflectivity of

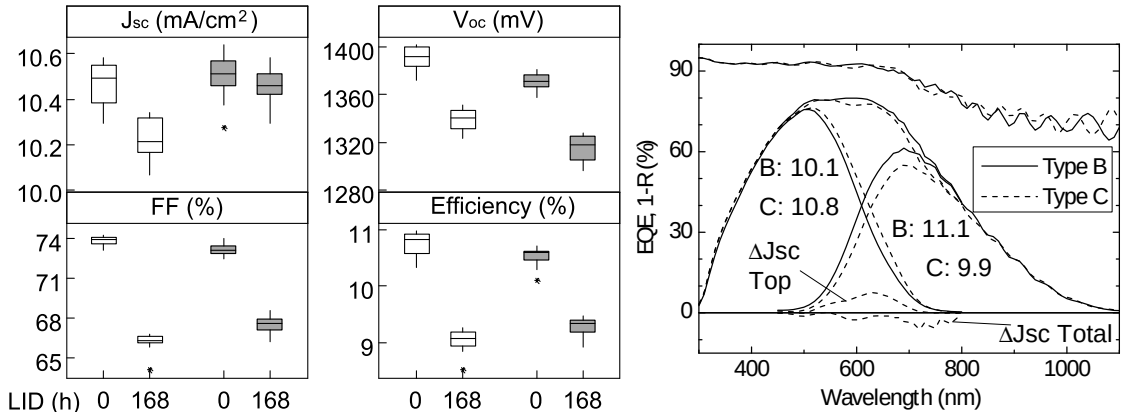

Figure 6.5.: (Left) figure: Box plots of the cell characteristics of 20 representative cells of the best runs of cells deposited with type B and type C TRJ respectively. Right figure: Corresponding EQE and 1-R plots. The corresponding currents are denoted as well as the differences in top- and total current.

the IRL. The discrepancies between the J_{sc} determined from the sun simulator and the one determined from the EQE measurements are due to the mentioned problems of the EQE measurements of the bottom cell on thick glass substrates (see section 3.2.3). The initial *FF* is higher for the cells deposited with the type B TRJ only because of the higher mismatch. The R_{oc} of both runs was similar (see Fig. 6.4). After 168h of light soaking, however, the cells of type C showed less degradation and a higher conversion efficiency than cells deposited with type B TRJ. Thus, it can be concluded that the IRL improved the stable efficiency of the device. A mere variation of the i-layers of the device with type B TRJ on the other hand is believed to bring no further improvements.

6.1.2. AFORS-HET Simulation Results

As mentioned above, the use of the ReLay concept was motivated by model considerations, which were motivated by results published regarding the optimization of the TRJ in a-Si:H/a-Si:H tandem cells [191, 196]. In the following, the role of the ReLay is illustrated using a 1D semiconductor model and the software tool AFORS-HET. A simplified layer stack (<p> a-SiC:H/<i> a-Si:H/<n> μc-Si:H/<p> μc-Si:H/<i> μc-Si:H/<n> μc-Si:H was used to calculate JV-curves of the tandem cells. The implementation of these models into AFORS-HET and applications can be found in [189, 203]. The program solves the semi conductor equations and a description of the density of states as well as transport properties are input parameters. The above mentioned models: TAT and FTM were applied to describe the transport across the TRJ. The input parameters were taken from literature: from Ref. [26] in the case of the amorphous and from [118] in the case of microcrystalline layers. The parameters are given in the appendix. The generation rate, which induces

the photo current, was calculated by a Lambert-Beer model with an adjusted light-path enhancement factor to match the experimentally obtained short circuit current density roughly. The error induced by the inappropriate description of the light trapping was assumed to be neglectable for the electrical calculations.

The simulation of solar cells incorporating μc-SiO$_x$:H-layers has not been discussed in literature in detail and no complete set of input-parameters are given. As described previously, the material is very heterogeneous and thus a 1-D description of such a layer must be based on an effective medium approximation. Due to the large number of parameters describing one layer, many different measurements must be combined to reduce the ambiguity in the description of the effective density of states. In the frame of this thesis, a simple approach is used for the differences of μc-SiO$_x$:H to the literature parameters for μc-Si:H. Based on the experimental finding, that the transversal conductivity and its thermal activation energy decreases with increasing CO_2 flow in the gas phase, the activation energy, E_a, in the layer was increased between 120 – 160 meV by decreasing the number of active dopants (N_d) in the simulation. The experimentally determined activation energies from top-bottom conductivity measurements are shown in Fig. 6.6. It can be seen that the experimentally obtained values for E_a change more than assumed in the simulation.

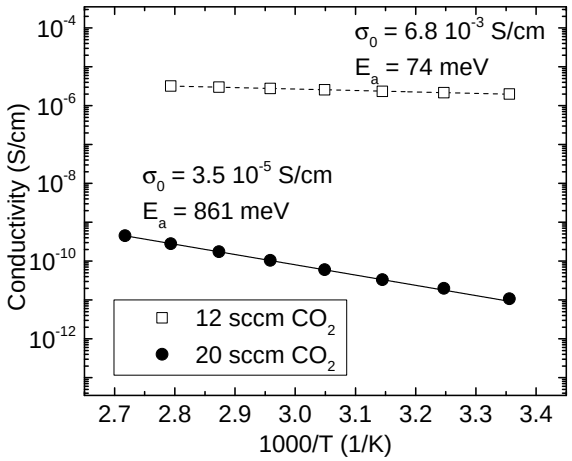

Figure 6.6.: Experimental determination of the top-bottom activation energy of the μc-SiO$_x$:H layers for IRL application, deposited with two different CO_2 flows. The layer thickness was 200 nm. The other deposition parameters are given table 4.1. The fit values according to equation 3.7 are indicated. [2]

The band diagrams of the TRJ with increased E_a (decreased N_d) are given in Fig. 6.7 for a design with and without the ReLay. The ReLay was simulated as a pure, n-doped μc-Si layer (i.e. N_d remained at the same value). It can be seen, that the space charge region (SPC) increases, i.e. the slope of the bands at the TRJ decreases, when E_a increases (which would translate into an increase of oxygen incorporation in reality). Due to Poisson's

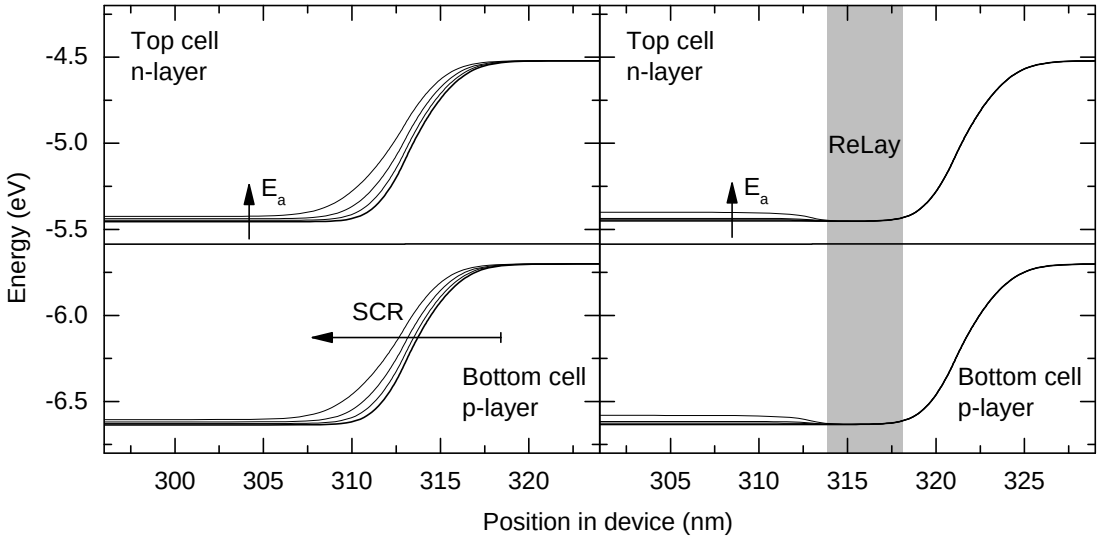

Figure 6.7.: Calculated energetic position of the conduction and valence band as well as the Fermi-level as a function of the position within the device (i.e. band daigrams) at the TRJ for varying activation energies, E_a, in the IRL. Left: without the ReLay; right: with the ReLay.

equation, also the electric field at the TRJ is reduced when the slope of the bands decrease. Since both used TRJ models (TAT and FTM) depend heavily on the electric field, the simulated tunneling rates and therewith the recombination at the TRJ decreases.

Illuminated I-V curves were calculated for devices with and without ReLay and are shown in the top part of Fig. 6.8. [3] The series resistances as determined from calculated illuminated I-V (R_{oc}) as a function of E_a are given in the bottom part of Fig. 6.8.

As can be seen, the I-V curves of the cells calculated without the ReLay show an s-shape and the R_{oc} increases dramatically as the activation energy increases. This can be ascribed to the less efficient tunneling at the TRJ. On the other hand, no significant change in R_{oc} can be observed when a ReLay is used because the n/p-junction was successfully shifted outside of the IRL and the rectifying characteristic of the inner n/p-junction diminishes. Both trends are similar to the experimentally observed behavior (compare Fig. 6.4. It should be mentioned at this point that the model seems to overestimate the positive influence of the ReLay, as it was experimentally observed during later optimizations that despite the ReLay the R_{oc} depends on the activation energy stronger than suggested here. Furthermore, the model is very sensitive to the defect density of states and the capture cross sections of the adjacent layers, which are parameters that are not very well known.

[3] It should be mentioned that the analysis of the dark I-V characteristic would be the more direct way, however, due to the fact that the experimental determination of the series resistance from dark I-V is difficult for tandem devices (for the reasons given in section 3.2.3), the light I-V curve was used.

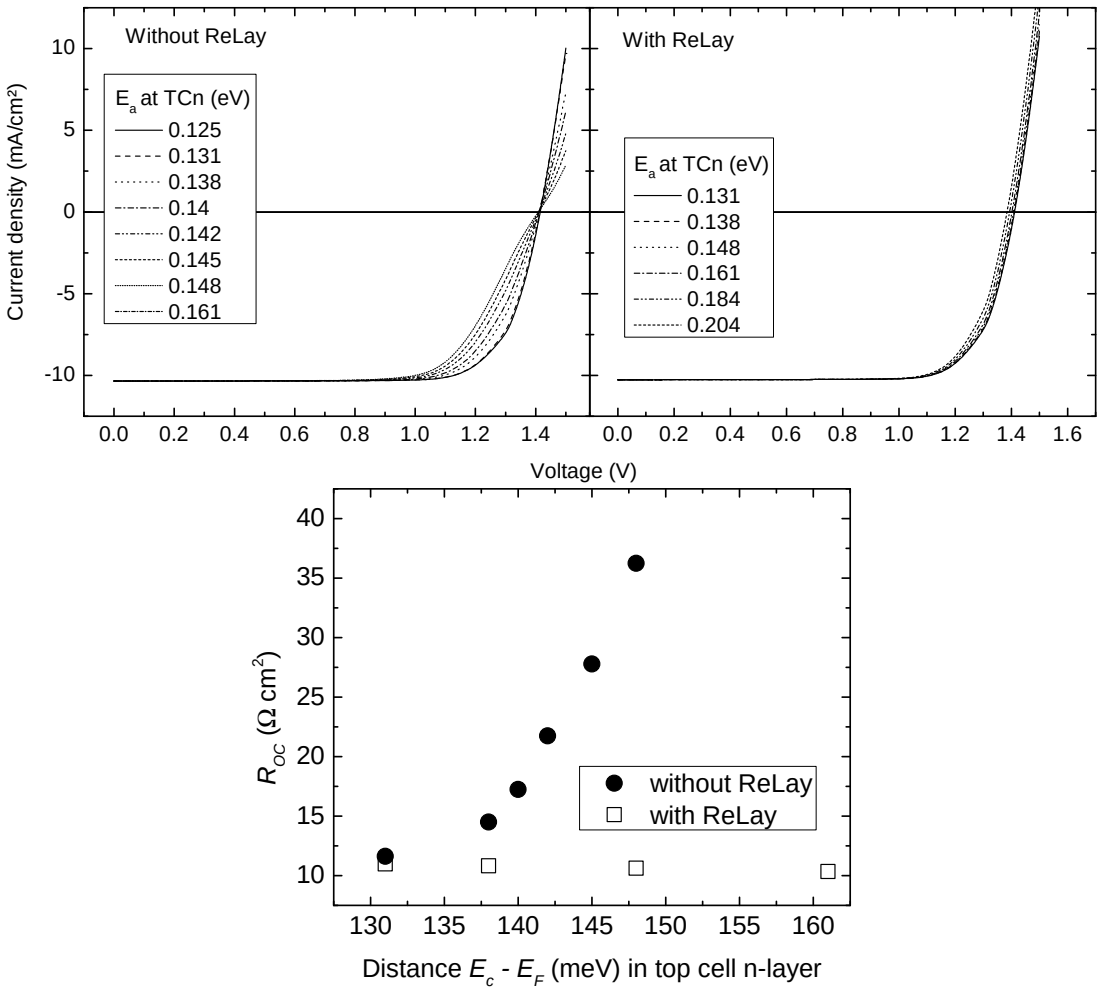

Figure 6.8.: Calculated series resistances from illuminated I-V curves, R_{oc} versus the activation energy, $E_a = E_f - E_c$, in the IRL, for a TRJ with and without the ReLay.

6.1.3. Summary

It can be summarized that the tunnel recombination junction was significantly improved by the implementation of an <n> μc-Si:H recombination layer behind the <n> μc-SiO_x:H IRL, up to a level where the stable efficiency of the type C TRJ was higher than the reference made with type B TRJ. It was shown by other groups that this layer is not always necessary for efficient TRJs if the appropriate conditions for the deposition of the IRL are chosen [10, 11]. However, it is believed that the ReLay-approach had not only a positive influence on the not yet optimized IRL shown in this section, but helped also in later experiments and allowed the deposition of material with a lower refractive index without electrical losses. The electronic function of the ReLay was explained by use of a model for the incorporation of oxygen into the IRL layer and the device simulator AFORS-HET. Here it was shown that the oxygen incorporation in the IRL, which leads both to a measurable reduction of conductivity and increase of activation energy, induces a widening of the space charge region at the TRJ. This decreases the tunneling probability and the electric field, which reduces the amount of necessary recombination at the interface, due to less tunneling currents. This leads to the increase of the series resistance (here represented by the R_{oc}) on the device level. If the ReLay concept is used, the effect of the widening of the space charge region is avoided.

6.2. Influence of CO_2 dilution in p-layer on V_{oc}

6.2.1. Ansatz

The introduction of the type C TRJ shown in the last section gave an increase in the short current density in the top cell. However, it made it necessary to replace μ-SiO_x:H bottom cell p-layer (BCp) by the non-oxidic BCp. This reduced the open circuit voltage, (V_{oc}), by 10-20 mV. The reasons for this behavior is believed to be due to one or more of the following identified reasons:

1. A *reduced crystallinity* of the bottom cell i-layer: As the BCp is deposited directly before the i-layer, the crystallinity of the BCp can have an influence on the nucleation and the crystallinity of the bottom cell. It is known that the V_{oc} depends on the crystalline volume fraction of the bottom cell (see section 2.2.1 or Refs. [33, 99]) and it was shown in section 4.2 that the crystallinity of the μc-Si:H doped layers decreases with the incorporation of oxygen.
2. The *quenching of shunts*: Due to the non-isotropy of the material, μc-SiO_x:H has a conductivity that is several orders of magnitude higher in the transversal (top-bottom) direction than in the lateral direction (as shown in chapter 4 and in ref.

[15]). This heterogeneity has the positive influence, that potential short circuits introduced by shunts are more localized and thus loose their negative influence (i.e. current drain) on the entire area [25].

3. The formation of a *hetero-emitter* at the p-i interface: It is known that a hetero-contact at the emitter consisting of a material with a larger band gap such as μc-SiO$_x$:H and one with a smaller bandgap such as c-Si can increase the V_{oc} as in wafer based hetero emitter cells. This is due to a higher selectivity of the emitter in case the resulting band offsets are tuned appropriately [204–206]. It was also found that the V_{oc} of single junction solar cells deposited in a n-i-p-configuration can be increased through the incorporation of oxygen into the p-layer [207]. This effect was not ascribed to the shunt quenching since the effect was also observed for samples on smooth substrates. Rather, it was ascribed to the differences in work function introduced through the oxygen in the p-layer: The activation energy increases slower than the band gap for moderate oxygen contents and then faster than the band gap. At this inflection point, a maximum in the work function is induced, which coincides with the maximum increase in V_{oc} (an illustration of the band diagram is given in the reference [207]).

6.2.2. Experimental Results

To reintroduce the oxidic BCp and to investigate this question further, two series were conducted in which the oxygen content of the BCp was systematically altered keeping the rest of the solar cell process the same. The first series consisted of a-Si:H/μc-Si:H tandem cells, the second one of μc-Si:H single junctions. The deposition parameters are based on the recipe for the BCp, which are given in table 4.3 with a TMB flow of 3 in the case of $0-8$ sccm CO_2 and 4 in the case of the other CO_2 flows. In case of the μc-Si:H single junctions, a non-oxidic seed layer (the same as for the TCp) was deposited prior to the μc-SiO$_x$:H layer to improve the TCO/p-contact and to assure fast incubation of the p-layer. The deposition time for the μc-SiO$_x$:H p-layer was adjusted according to the deposition rate, which was measured before on single layers of about 100 nm thickness.

To test the first thesis attributing the increase of V_{oc} in tandems cells with oxidic BCp to a lower crystallinity of the BCi, induced by the lower crystallinity of the BCp, Raman measurements were performed on the tandem cells. The Raman excitation was applied through the BCn after removal of the AZO/Ag back-contact by means of HCl etching. This method was suggested by Droz et al. [36] and was found to have a strong correlation to the V_{oc} of the solar cells. Fig. 6.9 shows the Raman spectra of two μc-Si:H sub-cells deposited on top of an oxidic (type C TRJ) and non-oxidic bottom cell p-layer (type B TRJ). All other deposition conditions were nominally the same. As can be seen, there is no

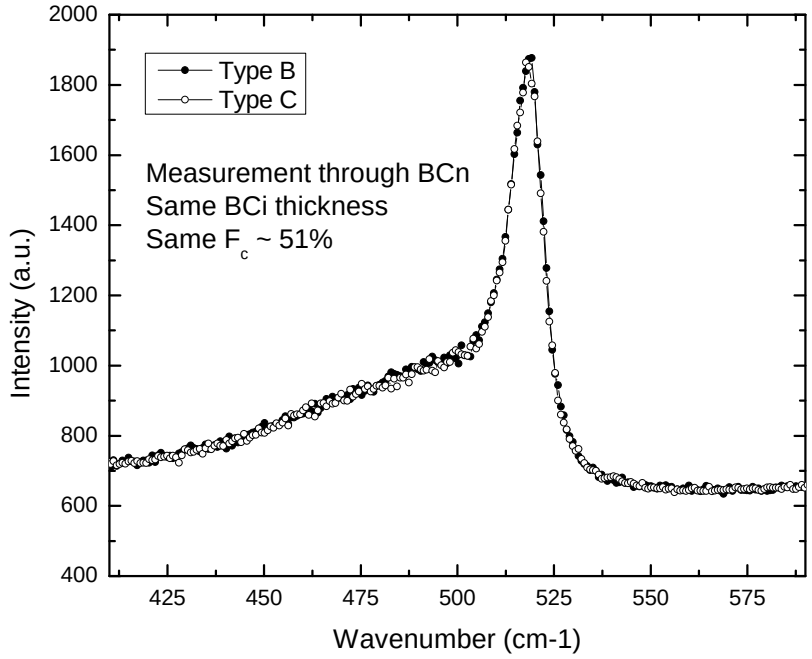

Figure 6.9.: Raman spectra of two μc-Si sub-cells deposited on top of an oxidic (type C) - (○) and non-oxidic bottom cell p-layer (type B) - (●). The measurement was performed through the BCn after removal of the back-contact by HCl etching.

difference between the crystallinity of the cell deposited on the oxidic BCp. Both F_c values were close to 51%, (for comparison, the F_c value for the BCp as determined from a 100 nm single layer decreases from 74% to about 53% when 4 sccm CO_2 is added to the gas phase). As a matter of fact, the numerical deconvolution yielded slightly higher F_c values, but with the difference below 1%. From the data given by [36], one can quantify a slope of -1.5 mV (and higher) per percentage Raman crystallinity for Raman measurements performed through the BCn. Although, the comparison of Raman crystallinity ratios are typically biased due to differences in the apperature and the deconvolution method, the evidence is high that the impact of the different BCp on differences in nucleation is in this case negligible.

Fig. 6.10 gives illuminated I-V parameters of the two series. A clear trend can be observed in the conversion efficiency (Eta) with increasing CO_2 flow from a median value of 6.5% at 0 sccm CO_2 to a value of 8%. This is due to an increase in V_{oc} and in FF. V_{oc} increases from a median value below 460 mV by 13% to values just below 520 mV. Here it is noticeable that the increase occurs almost entirely during the step from 0 to 4 sccm CO_2, althoug this conclusion should be confirmed by a larger base of data. A comparable gain of 60

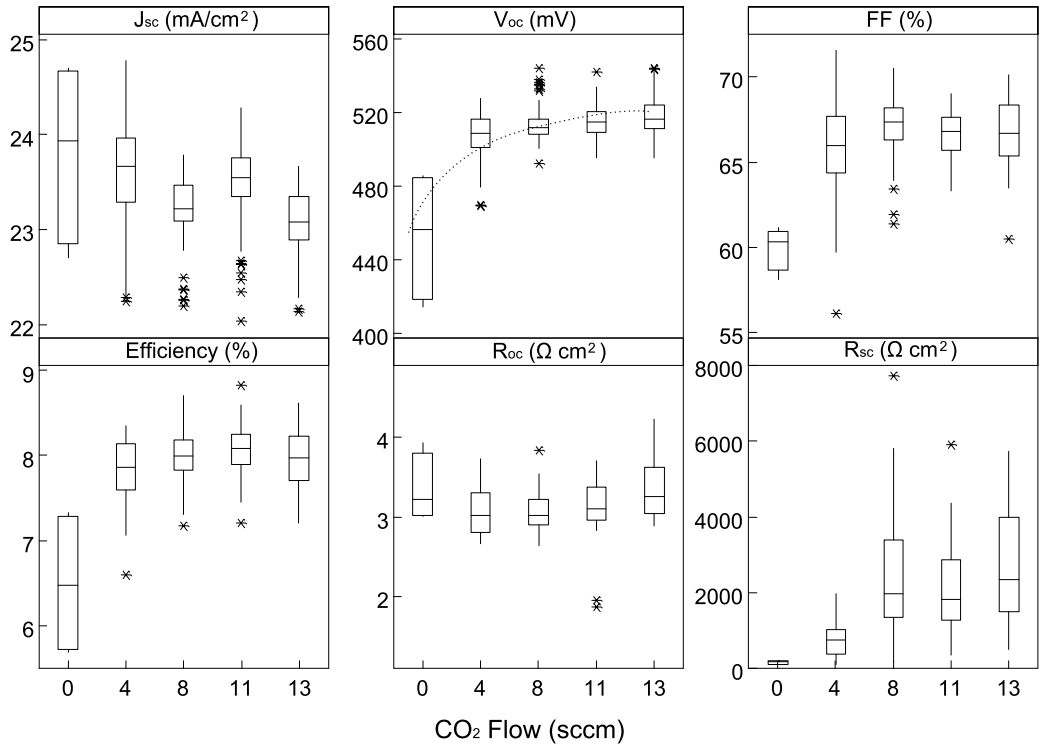

Figure 6.10.: Illuminated I-V parameters of the μc-Si:H single junction cell series with varying CO_2 flow used for the BCp. Note that the x-axis is not to scale. The statistics are taken from 20 representative cells.

mV was observed for μc-Si:H single junction cells deposited on un-etched ZnO:Al (not shown) for cells with and without μc-SiO_x:H p-layer. The FF improves by 13% from a median value of just above 60% to a maximum value of 68% at 8 sccm. When looking at the resistances, this can be attributed to a strong increase in shunt resistance as obtained from illuminated I-V at short circuit conditions (R_{sc}) during the same change in CO_2 flow. The slight decrease in FF for 11 and 13 sccm CO_2 could be partly due to the slight increase in series resistance as obtained from illuminated I-V near open-circuit conditions (R_{oc}), which could be attributed to the decreasing conductivity of the p-layer. The change in short circuit current density (J_{sc}) is less than 4% and is most likely due to slight differences in the p-layer thickness.

The I-V results of the tandem cell series are summarized in Fig. 6.11. In this experiment three tandems were deposited with varying CO_2 flows in the BCp. The cells had an IRL and were therewith of type D TRJ where both doped layers consisted of μc-SiO_x:H. As a reference, a device with a TRJ of type B was used (no IRL). Thus, the current of the cells with type D TRJ was considerably higher. Within the series, the top cell J_{sc} increased with increasing CO_2 flow from 10.1 mA/cm^2 to 10.3 mA/cm^2 indicating that the incorporation of the oxidic BCp further increases the intermediate effect. Furthermore, also the total

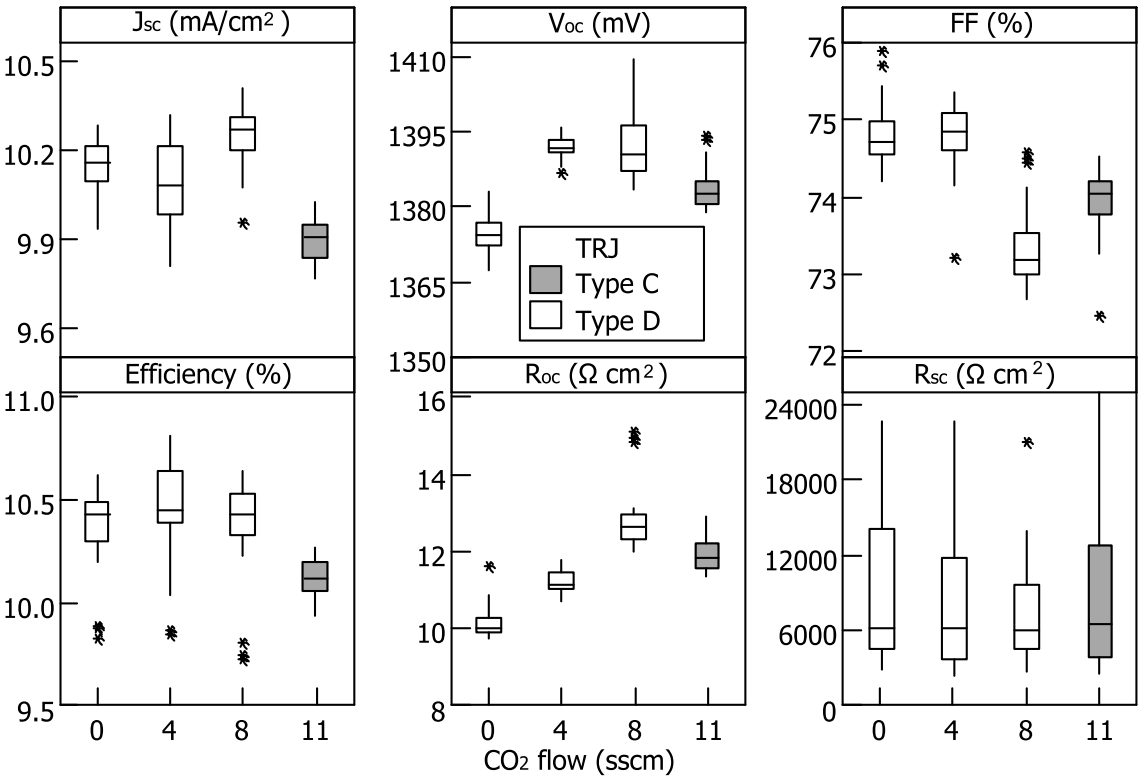

Figure 6.11.: Light IV parameter results of the tandem cell series with varying CO_2 flow used for the BCp. The cells represented by the open boxes have a IRL (type D TRJ) the cells represented by the gray boxes do not have it (type B). Note that the x-axis is not to scale. Statistics were taken from 20 representative cells.

current increased by 0.16 mA/cm^2, which can be ascribed to lower parasitic absorption in the BCp or an increased selectivity of the intermediate reflector due to the effect of a Bragg reflector. For the V_{oc}, similar trends can be observed for this series as for the μc-Si:H single junctions. However, the change of about 30 mV in the TJ is less pronounced than in the SJ, where about twice as much gain was reached. This could be attributed to a lower contribution of the *shunt-quenching* effect in the μc-Si:H sub cell as it is in case of the tandem cell deposited on top of the a-Si:H top cell, which reduces the roughness of the substrate. The *FF* is higher for cells with 0 and 4 sccm CO_2 due to a lower R_{oc}, which increases with CO_2 flow due to the higher activation energy in the BCp. The role of the matching can not be quantified due to the problems with EQE measurements on cells deposited on thick substrates mentioned in section 3.2.3. The currents are given in table 6.1.

Table 6.1.: Short current densities of the tandem cell series with varying CO_2 flow in the bottom cell p-layer.

CO_2 (BCp) (sccm)	TCn	$J_{sc,Top}$ (mA/cm^2)	$J_{sc,Bottom}$ (mA/cm^2)	δ_{top} (mA/cm^2)	δ_{total} (mA/cm^2
0	μc-SiO_x:H	10.1	10.0	0.1	-0.4
4	μc-SiO_x:H	10.2	10.1	0.2	-0.2
8	μc-SiO_x:H	10.3	10.0	0.4	-0.2
11	μc-Si:H (Reference)	9.9	10.5	-	-

6.2.3. Summary

In conclusion, it can be said that the desired type D TRJ configuration could be successfully integrated into the device. From the presented cell results and the parallels with data from literature, one can say that both the *shunt quenching* as well as the *hetero contact* hypotheses both contribute to the increase in V_{oc} of cells with oxidic BCp. A rather low CO_2/SiH_4 dilution of 0.3 for the deposition of the BCp was necessary to assure a low series resistance in the device. Further room for improvement is believed to lie in μc-SiO_x:H layers deposited at higher H_2 dilutions. Highly transparent μc-SiO_x:H p-layers ($E_{04} > 2.6\,eV$) with sufficient conductivity were reported for H_2 dilutions as high 2000 [154]. For comparison, the shown layers were deposited at a H_2 dilution of 400. The implementation of a non-oxidc p-type recombination layer could be another alternative for the use of μc-SiO_x:H material with a higher oxygen content. The fact that the series resistance in the tandem cell increases much faster with increasing CO_2 than in the single junction supports the in section 6.1 declared theory that the series resistance is more dominated by the interface and tunneling properties of the TRJ than by the bulk resistance of the μc-SiO_x:H layer, for the layers analyzed here.

6.3. Interplay between TCO Morphology and IRL Performance

The successful implementation of the type D TRJ with the oxidic μc-SiO_x:H BCp allowed a detailed thickness optimization of the IRL to maximize the top cell current. Parts of the results were published in Ref. [208].

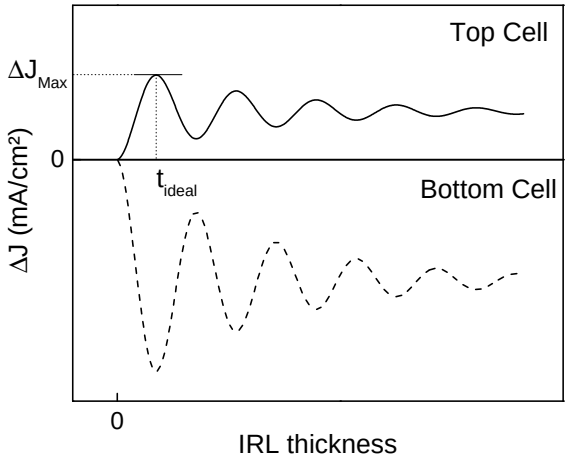

$$t_{ideal} = \frac{\lambda_0}{4 * n} \tag{6.2}$$

Figure 6.12.: Illustration of the dependency of the change in current as a function of IRL thickness for the flat case according to calculation performed by Pellation Vaucher et al. [76]. The quantities, ideal IRL thickness t_{ideal} and maximum top cell current gain ΔJ_{Max} are depicted.

6.3.1. Theoretical Background

For a flat layer stack the light propagation in the solar cell can be calculated using geometrical optics. Here, the intermediate reflector can be seen as a layer with a low refractive index put in between two layers with higher refractive indices, which are the top cell i-layer on the one hand and the bottom cell p-layer (or the ReLay) on the other hand. Due to the differences in refractive indices, reflection occurs on both interfaces. As the desired wavelengths (450-800 nm) which should be reflected are in the same order of magnitude as the optical thickness $n \cdot t$ of the layers, interference effects have to be considered. The phase shift at the first interface is 0 and the one at the second is equal to π due to the differences in the refractive index. The ideal thickness (t_{ideal}) of the intermediate reflector for a particular wavelength (λ_0) can be calculated by equation 6.2. To maximize the top cell current with respect to the whole spectrum, the integrated absorption has to be considered. Depending on the achievable refractive index n and the quantum efficiency of the cell, t_{ideal} is in the range of 60-80 nm for the flat case [76] (t_{ideal} is defined as the IRL thickness, where the first Fabry-Perot interference has its maximum). A schematic illustration of the dependency between reflected current and t_{IRL} is shown in Fig. 6.12.

6.3.2. Literature Review

A detailed comparison of geometrical optic theory and experimental tandem cell results deposited on SnO_2:F with ZnO:Al intermediate reflectors (ZIR) was published by Pellaton-Vaucher et al. [76]. It was found that the amount of reflected light is much higher for cells deposited on rough substrates than predicted by calculations for the flat case. Also, it was found that the ideal IRL thickness increased only slightly on rough substrates. A maximum at 75 nm was observed from the experimental data (roughly as predicted by the used flat model). The gain in top cell current was clearly linked to the roughness of the top cell/IRL interface. Also it was observed that for cells deposited in the substrate (i.e. deposition order n-i-p) configuration, the total current could increase with the implementation of the IRL (i.e. the sum of the gain in the top and the loss in the bottom cell was positive). Regarding the calculation, it was concluded that the exact quantification of the magnitude of the reflected current on *rough* substrates can not be done by models based on flat interfaces.

Rigorous models based on wave optics can solve this issue but are computationally very intensive. Hybrid models based on geometrical optics, scalar scattering theory and Monte Carlo tracing of light were therefore suggested for optical calculations on thin film silicon solar cells by Springer et al. [41] and Krc et al. [209] and allow very good reproduction of the experimentally obtained quantum efficiencies, also for cells deposited on rough substrates. A hybrid model was also used for the theoretical determination of the ideal IRL thickness by Domine et al. [210]. Due to the roughness of the substrate used ($\sigma_{rms} = 80\,nm$) which is in the same order of magnitude as the IRL thickness, the layer was split into two or three effective medias depending on whether the IRL thickness was greater than the roughness or not. The optical constants were then partly the ones of the, in this case ZIR, and the adjacent layers, a-Si:H and μc-Si:H. This model could reproduce the presented experimental data very well up to the thickness of 80 nm, where the model suggested no further improvement but a flat dependency of current gain to IRL thickness. The approximated top cell current gain per nm ZIR was calculated to be $0.03 mA/cm^2$ and the corresponding loss in bottom cell current was $-0.04 mA/cm^2$. Experimental results presented in the same study, however, showed further improvements in top cell current up to a value of 110 nm ZIR thickness (factor 1.4 thicker), where the maximum current gain was $2.8 mA/cm^2$. The divergence between the theoretical predictions of the scalar scattering model for the IRL and the experimental values were discussed in [77].

An investigation of the ideal t_{ideal} based on wave optics is given in [78] for wavelengths of 658 nm and 780 nm. The refractive index of the intermediate reflector was set to $n = 2$. The resulting ideal thickness based on the two calculated wavelengths was between 100-150 nm, which is in agreement with the *experimental* results published by Domine. Also, for higher IRL thicknesses, the reflected current followed Fabry-Perot interferences.

Rockstuhl et al. point out that the oscillations on rough substrates must have a larger period than in a flat case since it is determined by the z-component of the wave vector, which decreases with increasing TCO roughness, i.e. the rougher the substrate the thicker the intermediate reflector should be in order to achieve the maximum top cell current gain. A finding which is in contradiction to the suggestion of geometrical optic theory, which would lead to smaller t_{ideal} due to a larger effective light path on rougher substrates. This can explain the malfunction of the hybrid models.

It can be summarized that the interplay between the IRL and the TCO roughness was discussed in literature. The observation that the ideal thickness remains at the same value for smooth and rough substrates, as predicted by hybrid optical models could not be confirmed during the work of this thesis. In fact strong differences were observed depending on the type of TCO use, which will be shown in the next section. As literature revealed that hybrid models could not explain these observations, the experiments were accompanied by rigorous optical simulations.

6.3.3. Experimental Results

To analyze the exact dependence between the roughness of the front TCO and the effectiveness and ideal thickness of the IRL, nominally identical cells were deposited on three different front TCOs: LPCVD ZnO:B, APCVD SnO_2:F and sputter-etched ZnO:Al (see section 2.2.2) with different IRL thickness. No μc-SiO_x:H was used for the bottom cell p-layer to avoid the influence of a second reflecting interface. The standard top cell n-layer stack was used consisting of a 10 nm seed layer, the IRL with varying thickness and an 8 nm ReLay. For the cells with 0 nm IRL, the stack consisted of one 30 nm thick n-layer (same deposition parameters as for the seed and the ReLay).

The nominal top and bottom cell i-layer thicknesses were 270 and 1750 nm respectively (the actual values are probably slightly lower and dependent on the TCO roughness). Prior to the cell deposition, the TCOs were characterized using atomic force microscopy (AFM), transmission haze and angular resolved scattering. The results of the AFM experiments are given in Fig. 6.13 together with the external quantum efficiencies and the total absorption ($1 - R$) curves. The transmission haze and ARS measurements are discussed in section 6.3.5. For reasons given in section 2.2.2 the top cell p-layer had to be adapted to the TCO to assure a low Ohmic contact: the SnO_2:H p-layer consists of a thin, highly doped a-SiC_x:H layer and a thicker and more transparent a-SiC_x:H layer. The p-layer for ZnO:B is similar to this, but the first layer is deposited without CH_4 admixture. The p-layer used on the ZnO:Al consists of μc-SiO_x:H.

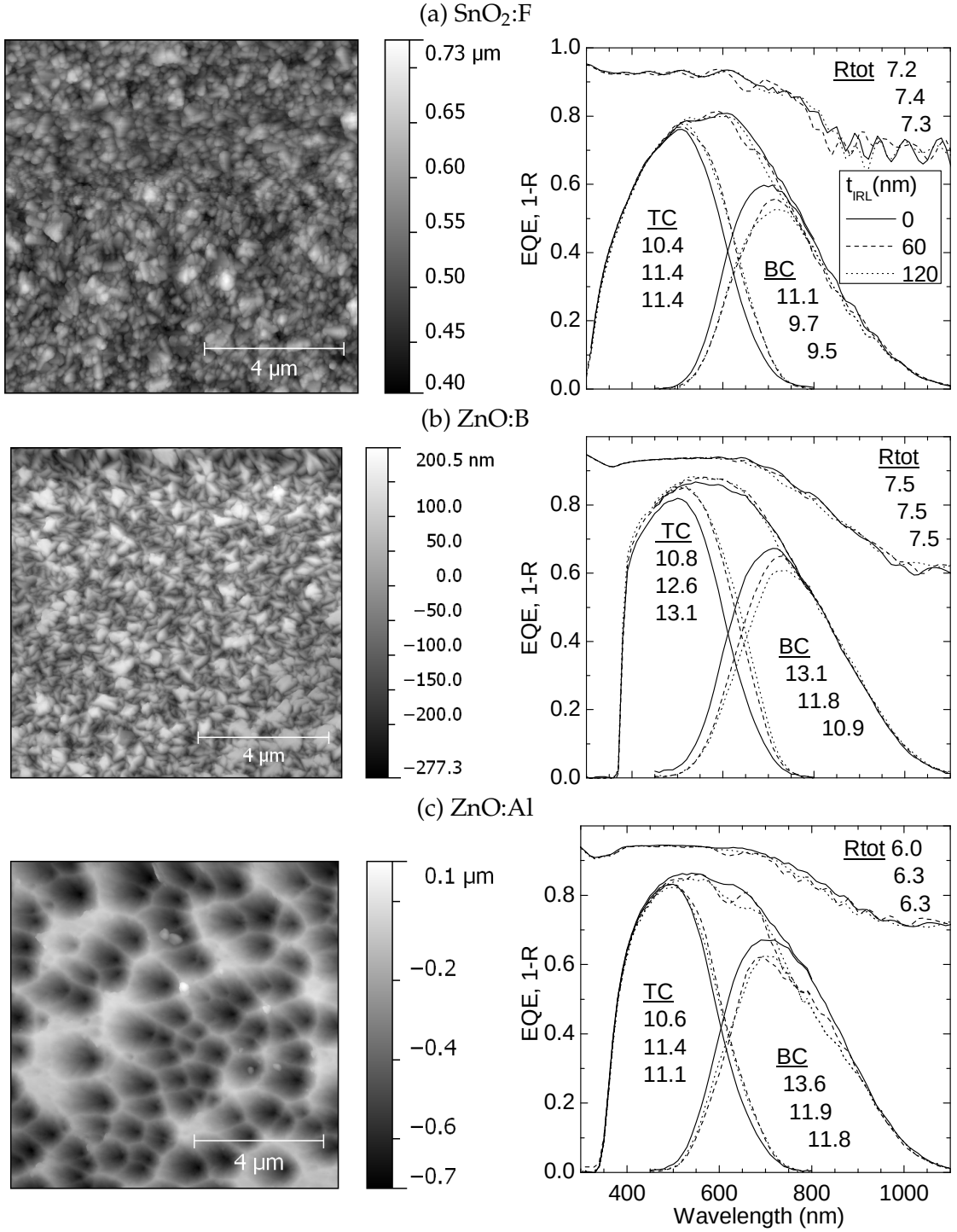

Figure 6.13.: AFM images of the three different TCOs used (left column) and selected *EQE* and $1 - R$ curves as a function of wavelength for three different IRL thicknesses (right column). The numbers indicate the corresponding integrated current densities.

AFM Characteristics

As can be seen in the left column of Fig. 6.13, the topographies of the TCOs are significantly different. The AFM data can be quantitatively analyzed regarding the average height- and period-distribution, which is e.g. described in [211]. The former is described by the root mean square deviation of the height distribution σ_{RMS} and the latter by the autocorrelation length l_{AC}. The value l_{AC} can be determined from the autocorrelation function ACF, which is defined as the convolution of a function with itself,

$$\begin{aligned} ACF(\tau_x, \tau_y)(\tau_x, \tau_y) &= \int_{-\infty}^{\infty}\int z_1 z_2 w(z_1, z_2, \tau_x, \tau_y) dz_1 dz_2 \\ &= \lim_{S\to\infty} \frac{1}{S} \iint_S \xi(x_1, y_1) \cdot \xi(x_1 + \tau_x, y_1 + \tau_y) dx_1 dy_1. \end{aligned} \tag{6.3}$$

Where z_i is the height value for (x_i, y_i), $\tau_i = x_1 - x_2$ and $w(z_1, z_2, \tau_x, \tau_y)$ is the probability density of the random function $\xi(x, y)$ for the points $(x_1, y_1), (x_2, y_2)$ and the distance between the points τ. If the function is not normalized, one speaks of the autocovariance function, an example of the autocovariance function, which was calculated from a ZnO:B AFM scan [4] is given in the left part of Fig. 6.14.

From the ACF one can deduce i.e. the period length for periodic structures. The periodicity of the randomly structured TCOs is close to zero. Under the assumption of isotropy, which is reasonably well fulfilled for the given TCOs, one can define a 1D radial ACF, which describes the 2D ACF. This has the advantage that the function is easier to analyze quantitatively. According to the in Ref. [211] described procedure, the 1D radial ACF was fitted using a Gaussian function in the form

$$ACF(x) = exp\left(-\frac{1}{2}\left(\frac{d}{\sigma_{AC}}\right)^2\right). \tag{6.4}$$

Where σ_{AC} is the standard deviation of the Gaussian. The autocorrelation length l_{AC} of a random surface is not clearly defined in the literature. According to [211], l_{AC} was defined ín the context of this work as

$$ACF(l_{AC}) = 0.05 \Rightarrow l_{AC} = \sqrt{6}\sigma_{AC}. \tag{6.5}$$

The fitted values for the l_{AC} for the three investigated TCOs are listed in table 6.2 together with the values for the σ_{RMS}. Comparing these values to the in plane views of the AFMs given in Fig. 6.13, one can see that the l_{AC} correlates with the mean period size of the topography. It should be pointed out that this is not a theoretical necessity, though. The

[4] By means of the software tool Qwyddion

Table 6.2.: σ_{RMS} and l_{AC} of the different TCOs SnO_2:F, ZnO:Al and ZnO:B.

TCO (Type)	σ_{RMS} (nm)	l_{AC} (nm)	ratio -
SnO_2:F	45	621	0.07
ZnO:B	70	323	0.22
ZnO:Al	140	800	0.18

resulting 1D autocorrelation functions together with the corresponding fits for all three TCO types are given in the right plot of Fig. 6.14.

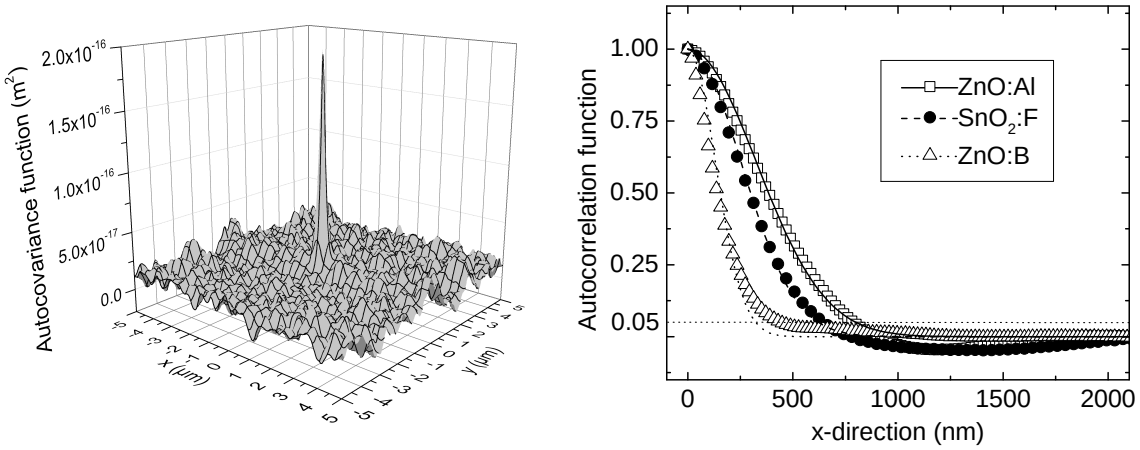

Figure 6.14.: Autocovariance function of ZnO:B (left) and 1D-Autocorrelation functions of the three different TCOs (right). The 5% criteria is indicated by the line.

From the values given in table 6.2 one can see that the features of the SnO_2:F are rather small in height and have a relatively large average period. The ZnO:B is characterized by a high σ_{RMS}/l_{AC} ratio through high features with a low l_{AC} and the etched ZnO:Al has wide, crater-like features, which result in a high σ_{RMS} and high l_{AC}. As calculated by Lipovsek et al. [73] for periodic structures, the size and the period of the light scatterer has a very high influence on the light absorption of a particular wavelength. Thus, it was shown that the ideal values differ for a-Si:H single junction (300/300) and μc-Si:H single junction cells (1000/1000).

6.3.4. Discussion of the Experimental Results

When looking at the absolute currents depicted in Fig. 6.13 without an IRL ($t_{IRL} = 0\,nm$), one can see that there are slight differences in the top cell currents, which may

be explained by the differences in the p-layer and by differences in the transparency of the TCO. It is also noticeable that the bottom cell currents differ significantly, which can not be explained by differences in the p-layer, the TCO transparency or slightly different thicknesses induced by the topography. The differences are clearly due to the differences in the light scattering. Taking into account the surface parameters given in table 6.2, the trend for the bottom cell current as a function of σ_{RMS} is qualitatively in agreement with the predictions made by Lipovsek et al. for the μc-Si:H solar cell [73]. It is also in agreement with the transmission haze and ARS measurements, which are discussed in the following section.

In Fig. 6.15 the absolute change in current $J_{sc}(t_{IRL})$ - $J_{sc}(t_{IRL} = 0\,nm)$ for the top cell, the bottom cell and the reflected current is plotted against the IRL thickness for the different TCOs. In this plot, also the data for an un-etched ZnO:Al TCO is shown. This dependency is particularly interesting because the highest total currents, which were obtained in the devices deposited on etched ZnO:Al ($24.8 mA/cm^2$ when $t_{IRL} = 0$ nm), can not be distributed evenly onto the sub cells using the IRL, as shown in Fig. 6.13. On the other hand, the top cell currents obtained on the ZnO:B, show that the IRL has the potential to reflect more than 2 mA/cm^2 if the TCO topography is appropriately.

It can be seen that the ideal thickness on ZnO:B is the highest with a value of about 120 nm. Also, for lower thicknesses the gain is higher compared to the other TCOs. The SnO_2:F shows a maximum between 75 and 90 nm. The maximum of the etched ZnO:Al is lower than the one of the SnO_2:F but at a higher thickness. The unetched ZnO:Al has, as expected, the lowest t_{ideal} and the lowest IRL performance. The differences between ZnO:B and etched ZnO:Al in the absolute currents in the case with an IRL are also in agreement with a similar comparative study done by Rockstuhl et al. [72].

Fig. 6.15 shows that the ideal IRL thickness and its effectiveness is strongly dependent on the type of TCO used. Assuming that the differences in absorption behavior due to the different TCO/p-layer stacks and due to differences in the i-layer growth is negligible, this must be due to the fact, that the light propagation is different in the cell due to the differences in the topography. As Fig. 6.15 shows the *changes* in current, the assumptions seem justified, although there is a theoretical dependence of the IRL effectiveness on the top cell thickness. This dependence however is low as 2D rigorous calculations have revealed [212]: An assumed change in top cell thickness from 270 to 200 nm reduced the effectiveness of a 60 nm IRL by not more than 10%. When we compare the ideal IRL thickness of the unetched ZnO:Al (60 nm) and the ZnO:B (120 nm), we see that there is a difference of a factor 2. This is an astonishing quantity, which has not been reported before in the comparable experimental studies [76, 210]. However, it is qualitativly in agreement with theoretical predictions made by Rockstuhl et al. [78]. The differerences to the observations made by Pellation-Vaucher, which observed more or less the same ideal

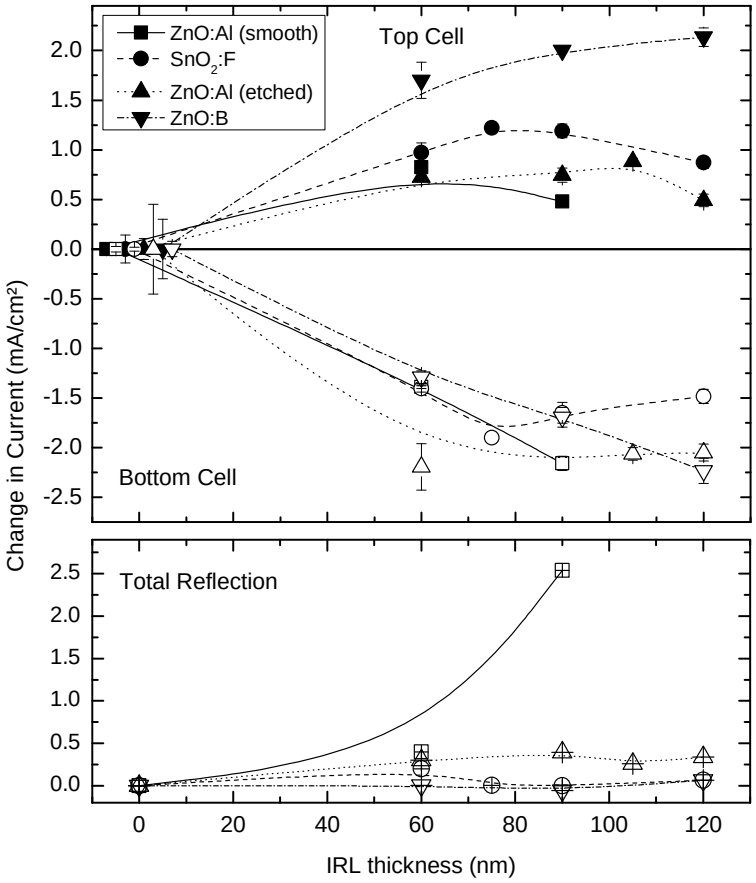

Figure 6.15.: The change in top (top - closed symbols) and bottom (bottom - open symbols) cell current as a function of IRL thickness for a-Si:H/μc-Si:H tandem cells deposited on various TCOs. The symbols and the error bars are the mean and the standard deviation respectively of several EQE measurements performed on different cells on the same panels (same runs). The data is partly the same as shown in Fig. 6.13. The bottom plot shows the integrated total reflectance of the same cells.

thickness on rough and flat cells, and Domine et al., that observed about a factor of 1.4, can be explained by the different TCOs used. The ARS measurements were performed for a wavlength of 635 nm, which is relevant for the IRL. The procedure, the set up and the definition of the CC BDTF is given in the master thesis by C. Nock [213].

6.3.5. Comparison to TCO Characteristics

The previous section confirmed the theoretical suggestions that the topography has a significant influence both on the ideal thickness and the TCO. It is desirable, to understand these differences and relate them to other TCO characteristics. Transmission haze and angular resolved scattering (ARS) measurements give direct information about the light

scattering properties of TCOs. The transmission haze curves as a function of wavelength and the cosine corrected bidirectional transmission function (CC BDTF) as a function of angle as extracted from angular resolved scattering measurements for the used TCOs are given in Fig. 6.16. The procedures, the experimental set ups and the determination of the quantities transmission haze and CC BDTF are discussed in the master thesis of C. Nock [213].

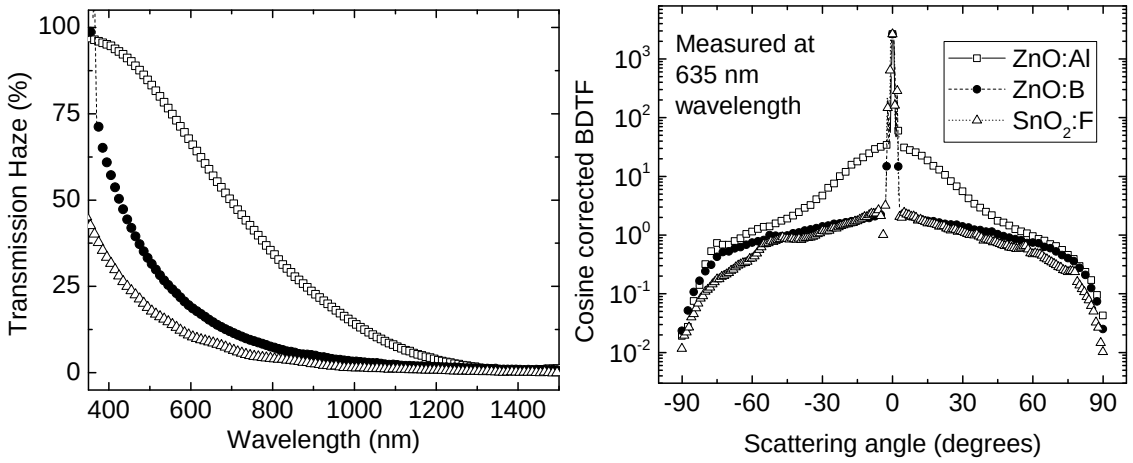

Figure 6.16.: (Left) The transmission haze curves as a function of wavelength and (right) the cosine corrected bidirectional transmission function (CC BDTF) as a function of angle as extracted from angular resolved scattering measurements for the used TCOs.

It can be seen that the presented light scattering properties do not explain the differences in the effectiveness of the IRL, which are thought to be due to light scattering, neither quantitatively nor qualitatively. In particular, the properties indicate that the ZnO:Al scatters more light and in wider angles than the ZnO:B in the relevant wavelength region, but the cell results indicate the opposite. This discrepancy is attributed to the fact that these measurements are performed in air and are thus not fully comparable to the conditions in the cell. This discrepancy between solar cell results and optical measurements of the light scattering in this wavelength region has been previously reported also by Rockstuhl et al. [72].

6.3.6. Optical calculations

Besides the presented optical measurements, another method to correlate TCO properties to light scattering is, as mentioned in the beginning of this chapter, optical modeling. As 1D hybrid models have shown to be not appropriate to simulate the the effect of the IRL appropriately, we choose rigorous optical modeling. due to the computational intensiveness of these calculations, two approaches were followed. 2D calculations, which are less computational intensive, were performed for the first models by C. Schwanke in

the frame of his diploma thesis [212]. As these calculations were found to be not fully accurate due to the missing dimension, selected calculations were repeated at the Zuse Institute Berlin (ZIB) in collaboration with M. Hammerschmidt, which are currently ongoing. Fig. 6.17 shows the dependency of the gain in EQE at 600 nm in dependence of the IRL thickness (left plot) and the autocorrelation length of the TCO (right plot). The gain in EQE at 600 nm is defined analogously to Fig. 6.15 as the difference in EQE between a device with no IRL ($t_{IRL} = 0$ nm) and one with 60 nm IRL.

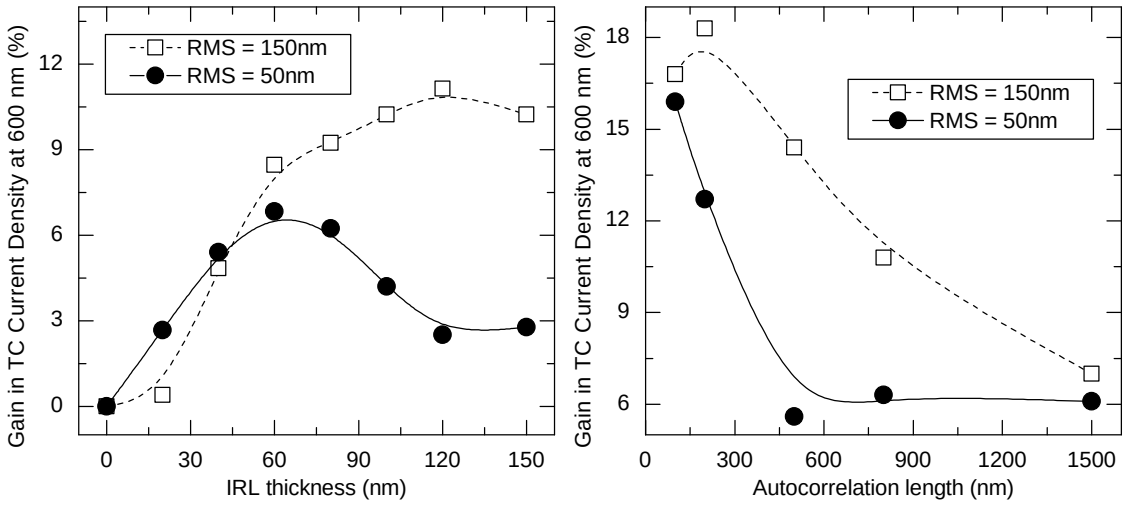

Figure 6.17.: Simulated gain in top cell current as a function of IRL thickness (Left) and the gain in top cell current of 60 nm IRL compared to 0 nm IRL for different autocorrelation length (right) for 50 and 150 nm σ_{RMS}.

The left plot of Fig. 6.17 confirms again that an increase in the σ_{RMS} can increase the ideal thickness of the IRL theoretically by a factor of 2. The right plot gives an explanation for the superior IRL performance on the ZnO:B, as it shows that a small l_{AC} significantly improves the effectiveness of the IRL. [5]

6.3.7. Summary

It can be summarized that both the experimental and the theoretical studies indicate that the topography of the TCO gives important implications for the design of the IRL. This can result in a difference of a factor of 2 in the ideal thickness and in the amount of current that is being reflected depending on the TCO topography. Both, experimental and theoretical studies, indicate that a small autocorrelation length is desirable for a good

[5] The reader is referred to Ref. [212], for a discussion regarding the representativeness of a single wavelength to the whole top cell current as well as for an error analysis regarding the calculation procedure, the design of the optical modeling and surface generation and regarding the limitations of 2D calculations. The results were being reproduced by 3D calculations for several representative wavelengths at the ZIB during the end of this thesis.

IRL effectiveness. When this finding is related to other studies regarding the *growth* of a-Si:H and μc-Si:H depending on the TCO topography (i.e. Python et al. [75]), this is not advantageous, as it is likely that the electrical properties diminish on such a TCO. Regarding further improvements in the IRL on the etched ZnO:Al, which showed the best overall solar cell results, the findings indicate that there is a fundamental limitation to the reflectivity of the IRL due to the large feature size of this TCO. Here, the fabrication of another scattering interface is desirable. This could either be obtained via a double structure at the front electrode, or a light scattering structure at the IRL itself. In this perspective, the deposition of spheric crystals between the top and the bottom cell could be an alternative to a one layer IRL, as it was proposed by Bielawny et al. and Fehr et al. [214, 215].

6.4. Stability of a-Si:H/μc-Si:H solar cells with IRL

The conversion efficiency of solar cells incorporating a-Si:H layers decreases upon illumination for the first hours until it equilibrates. The time and amount of this light induced degradation (LID) depends mainly on temperature, light intensity and spectral distribution as discussed in section 2.1 and 3.2.3. Also, the design of the device has an important influence on the LID. Therefore, all optimization experiments were ultimately evaluated based on the stabilized I-V characteristic values.

During the TRJ optimization in the course of this thesis, a clear interplay between the R_{oc} in the state before light soaking and the LID factor was observed. The LID factor is here defined as the ratio of the difference in conversion efficiency between before and after 168h of light soaking ($\eta_{0h} - \eta_{168h}$ to the initial efficiency (η_{0h}). This dependency was systematically analyzed in the frame of an experiment targeting the optimum dopant gas flow ratio ($PH_3/(SiH_4 + CO_2 + PH_3)$ for two different CO_2 (18 and 24 sccm respectively). The initial cell results were already discussed in section 4.4. The LID factor against the R_{oc} in the initial state for these cells is shown in Fig. 6.19.

When looking at the data presented in Fig. 6.19, there is a clear trend observable, indicating that cells that have a high R_{oc} before light soaking degrade more. An explanation for this behavior could be as follows: The series resistance induced by the IRL causes a reduction of the potential difference across the i-layer. This increases the amount of recombination events due to a lower electric field during the light soaking. The recombination events lead to an increased number of dangling bonds, which increases the LID factor.

The inlet in Fig. 6.19 shows that with an adapted PH_3 flow, a similar LID factor with a higher CO_2/SiH_4 ratio and a resulting lower refractive index of the IRL could be reached.

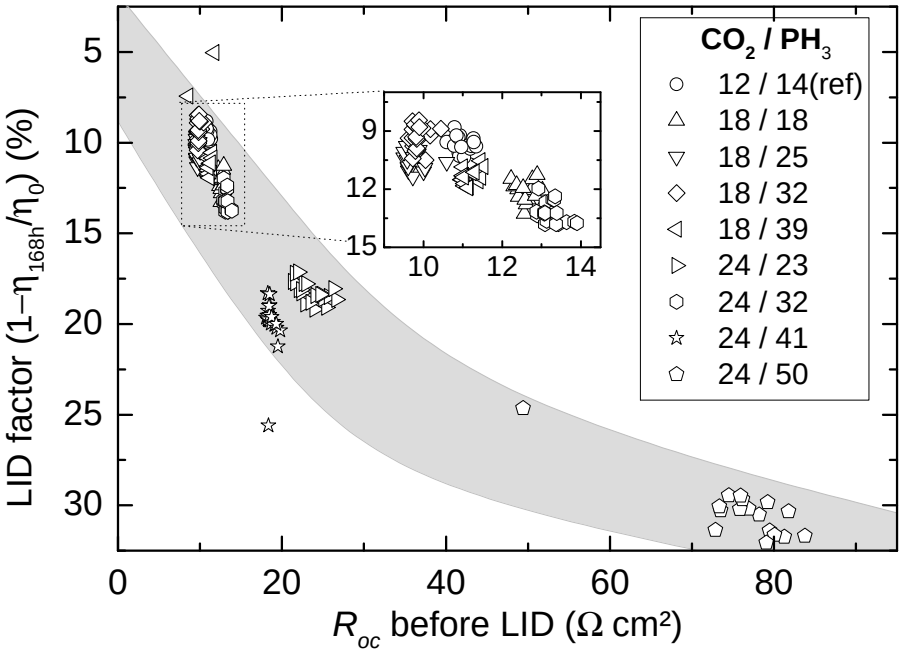

Figure 6.18.: The relation between series resistance determined from light I-V (R_{oc}) before LID and the LID factor in solar cells with varying quality of the TRJ. The cells are from an experiment where the CO_2 and PH_3 flows were varied as indicated in the legend. The deposition parameters are described in section 4.4.

Due to the lower refractive index and the increased thickness of the IRL, the resulting cells were all bottom limited. Based on these positive results, the bottom cell thickness was increased from the standard value of nominally 1750 nm to 2800 nm. The device was then deposited on annealed ZnO:Al. The annealing of the ZnO:Al improves the optical *and* electrical properties of the TCO front electrode so that higher current densities and fill factors can be obtained as mentioned in section 2.2.2 and in Ref. [87].

The resulting cells reached the then highest solar cell efficiencies for thin film silicon solar cells at the PVcomB. After the application of an anti reflection (AR) foil, the conversion efficiency before LID was 13.0%. The anti reflection foil is described in [216]. The top and bottom cell current densities as measured by EQE (without the AR) were 11.9 mA/cm^2, same for the top and the bottom cell, respectively. Due to the problems related to the measuring of the bottom cell when deposited on a thick substrate desribed in section 3.2.3, the cells are mostlikely top limited. A further increase of the IRL thickness to 80 nm and 100 nm, respectively, did not bring a significant improvement. This is most likely related to the low light scattering of the relevant wavelengths on the etched ZnO:Al, which was discussed in the previous section 6.3. The illuminated I-V curve of the cell in the inital and state and after 668h of light soaking and its conversion efficiency as function of light soaking time are shown in Fig. 6.19.

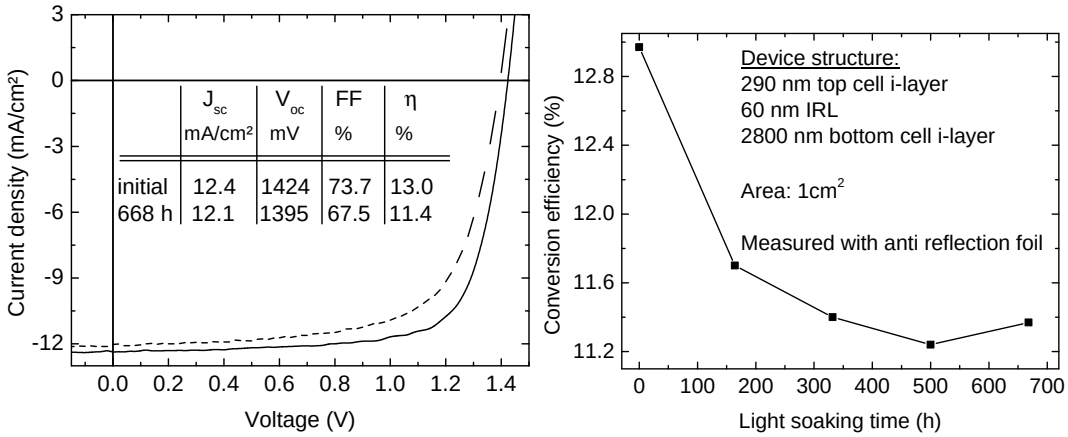

Figure 6.19.: Current density as a function of applied voltage before light soaking and after 668 h of light soaking (left) and the conversion efficiency as a function of light soaking time (right) of the best solar cell prepared in the course of this work. The device was deposited on annealed ZnO:Al and has TC/IRL/BC thicknesses of 290/60/2800 nm. For the I-V measurements, an anti reflection foil was put in front of the glass, which increased the conversion efficiency by 0.4% absolute.

It can be summarized that the optimized IRL led to high stable efficiencies. The best cell results were obtained on the ZnO:Al TCO. The TRJ with the improved IRL showed no effect on the series resistance. High top cell current gains of more than 2 mA/cm^2 were measured on ZnO:B. However, due to the difficult growth conditions on this type of TCO, the high top cell currents have not led to high efficiencies.

7. Conclusions and Outlook

The topic of this thesis was the development of wide band gap materials for the application in thin film silicon solar cells. The goal of this thesis was on the one hand to establish and control the μc-SiO_x:H deposition process and to gain a deeper understanding of the role of the deposition parameters for the film growth. Also the integration of these layers into the a-Si:H/μc-Si:H solar cell process was a goal. On the other hand, the investigation of μc-SiC:H as a possible alternative to μc-SiO_x:H was a topic of this thesis. Regarding the μc-SiO_x:H development, the following points can be summarized:

1. The variations of the gas phase composition showed similar results as previously reported by other groups. This can be summarized into the following points: The admixture of CO_2 to the gas phase of a μc-Si:H layer allows an increase of the optical gap E_{04} and a decrease of the refractive index n, which makes the material applicable as wide band gap window layer and particular applicable as an intermediate reflector layer (IRL) for a-Si:H/μc-Si:H tandem cells. The reduced crystallinity can be increased by an additional hydrogen dilution. The phase separation between a-SiO_x:H and μc-Si:H, which was already reported by other groups, has been confirmed on samples made for this thesis by TEM EDX measurements.

2. The variation of RF power and deposition pressure and the conducted plasma diagnostics revealed interesting differences between a conventional μc-Si:H regime and one with a CO_2 admixture. The increase in RF power increases the CO_2 dissociation proportionally more than the SiH_4 dissociation, which leads (other than in a conventional μc-Si:H regime) to a strong reduction in crystallinity. An increase in deposition pressure enhances the crystallinity significantly. This increase is explained by a reduced ion bombardment and/or an increased SiH_4 depletion. The optimization of the deposition pressure led to the successful implementation of the first IRL into the a-Si:H/μc-Si:H baseline at PVcomB.

3. The optimization of the doping gas flow, which was simultaneously performed in the device and on single layers, revealed that with an increase in CO_2 admixture, the PH_3 flow has to be increased as well. For μc-SiO_x:H n-layers, which perform best in the device, this translates into precursor gas composition ($SiH_4/CO_2/PH_3/H_2$) of 10/18/25/3000 as opposed to 10/0/6/3000 for the best performing μc-Si:H layer. This is presumably due to a preferable P-incorporation into the amorphous a-SiO_x:H

phase than into the μc-Si:H phase. This is a working hypothesis, which is currently still under investigation. The in-plane conductivity of the optimized μc-SiO_x:H layer is more than five orders of magnitude lower than the transversal conductivity of a nominally same layer in the device, as estimated from the I-V curve of the device. Direct comparison of μc-SiO_x:H p- and n-layers revealed a difference of more than three orders of magnitude for optimized dopant gas flows. Raman measurements revealed that this is due to the more detrimental influence of the TMB p-dopant gas on the crystallinity compared to the n-dopant gas PH_3. As this is widely known for pure μc-Si:H layers, the admixture of CO_2 seems to enhance this effect. This was also previously presumed by other groups.

4. An interesting increase in the conductivity of μc-SiO_x:H n-layers has been observed of more than three orders of magnitude upon annealing at low temperatures. This is currently ascribed to an activation of dopants in the amorphous silicon oxide phase by hydrogen effusion. Unlike a similar increase in conductivity, which was observed for μc-Si:H, this effect could not be reversed upon exposure to vacuum.

Regarding the μc-SiO_x:H development, it can therefore be concluded that a state of the art process for the film deposition for application as IRL in a-Si:H/μc-Si:H tandem cells was developed. The variation of the deposition parameters contributed to the general knowledge about this material.

Regarding the deposition of μc-SiC:H by PECVD from CH_4 and SiH_4, it can be concluded that the presented approach bore no immediate success. However, the presented data can be a basis for further developments. Possible next experiments have been outlined. Precisely, an increased hydrogen dilution combined with the presented high pressure high depletion approach seems to be a promising direction for further experiments.

The e-beam crystallization of a-SiC_x:H samples showed interesting first results, which are in agreement with crystallization experiments performed using a laser previously reported by other groups. A composition near stoichiometry seems to be fundamental for the formation of crystalline SiC. Carbon rich samples showed lower film ablation upon e-beam crystallization than Si rich samples. However, C-rich samples showed cracks upon crystallization. E-beam crystallized SiC films are believed to have the potential for increasing the efficiency of poly-Si solar cells.

Regarding the a-Si:H/μc-Si:H tandem cell development with IRL, the following conclusions can be summarized:

1. The deposition of a thin μc-Si:H n-layer behind the IRL showed a significant improvement in the series resistance, which can be attributed to an improved tunnel recombination junction (TRJ). Electrical modeling using 1D semi conductor theory and the simulation tool AFORS-HET, indicated that this recombination layer im-

proves the TRJ due to a narrower space charge region and resultantly higher tunnel currents.

2. The development of an 'all μc-SiO$_x$:H TRJ' by incorporating a μc-SiO$_x$:H p-layer behind the IRL, showed a positive influence on the open circuit voltage of the device by 10-20 mV. This gain was discussed and can be explained by an increased shunt resistance and/or the formation of a μc-SiO$_x$:H/μc-Si:H hetero contact, which improves the p-i-interface. The latter explanation is supported by the observation that an introduction of a μc-SiO$_x$:H p-layer resulted in an improvement of 40 mV also non textured (smooth) ZnO:Al compared to the same p-layer without CO_2 admixture.

3. The variation of the IRL on different types of TCO revealed a severe dependence of the effectiveness and the ideal thickness of the IRL on the TCO topography. In numbers, both the maximum reflected current and the ideal thickness vary by a factor of two from the TCO where the IRL performed worst (unetched ZnO:Al) to where it performs best (ZnO:B). Optical simulations revealed that this is presumably due to the low autocorrelation length of ZnO:B. This finding is not in agreement with optical measurements characterizing the light scattering properties in the relevant wavelength region such as transmission haze or angular resolved scattering measurements. The discrepancy is ascribed to the fact that these measurements are conducted in air.

The best a-Si:H/μc-Si:H solar cells manufactured in the course of this work had an efficiency of 13.0% before light soaking and a LID factor of 12.3%. After the implementaion of the optimized top cell p-layer, the initial efficiency was further increased to 13.4%. This record cell was deposited on etched and annealed ZnO:Al. As mentioned above, the high currents that are possible on this type of TCO can not be appropriately matched at the moment by the IRL. A further increase in top cell i-layer thickness is assumed to increase the LID factor. On the other hand, the high top cell currents on ZnO:B of more than 13 mA/cm^2 did not lead to record efficiencies due to the not optimized cell design for this type of TCO.

Outlook

From this starting point, assumptions for further improvements can be made, based on the experiments made during this thesis and advances presented in literature. Two approaches are distinguished: (A) Improvements on annealed ZnO:Al for a-Si:H/μc-Si:H tandem cells and (B) the quadruple junction approach. It is assumed that all individual improvements can be combined. Improvements to the substrate or TCO topography are therefore neglected. Improvements to the light trapping are believed to be able to in-

crease the spectral response significantly, but they most often also lead t compromises that have to be made regarding in the electrical performance of the solar cell. It is furthermore assumed that the LID factor remains at 12.3%. The influence of matching on the FF is neglected. The estimated advances on annealed ZnO:Al are summarized in table 7.1.

Table 7.1.: Predicted improvements for a-Si:H/μc-Si:H tandem cell on annealed ZnO:Al. The given I-V parameters are the *initial* values. The stable efficiency is calculated assuming a constant LID factor of 12.3%.

Assumption	$J_{sc,top}$	$J_{sc,bot}$	V_{oc}	FF	stable η
starting point with AR	12.7	13.0	1432	73.0	11.6
μc-SiO_x:H layers (1.)	13.2	12.7			11.9
annealed ZnO:Al (2.)	13.4	12.8			12.3
bottom cell i-layer (3.)		13.4	1440	75.0	12.7
laser design (4.)	13.4	13.4	1440	76.0	12.9

The indicated assumptions are as follows:

1. Further improvements in the μc-SiO_x:H layers: Increase in the total current by 0.2 mA/cm^2 by increasing the band gap of the top cell p-layer (currently E_{04}=2.2 eV). E_{04}=2.6 eV at a conductivity of 10^{-5} S/cm was shown by Lambertz et al. by merely optimizing the gas phase composition [154]. Increasing the top cell current by further optimizing the refractive index from now 2.1 to 1.8 as shown by the Neûchatel group [210] would increase the top cell current gain by 0.3 mA/cm^2 as calculations suggest [212].

2. Optimization of the ZnO:Al layer through the adjustment of the annealing procedure and though thickness reduction. As the thickness of the ZnO:Al is not optimized on the annealing procedure, a further increase in total current of 0.3 mA/cm^2 through a mere optimization should be possible.

3. Optimizations of the bottom cell i-layer should increase the FF by 2% absolute and the V$_{oc}$. This assumption is motivated by comparing the best μc-Si:H sub cell results deposited at PVcomB (J_{sc}=23.9 mA/cm^2 V_{oc}=540 mV, FF=68.9%) with world record results [62]. For simplification, it is further assumed that the bottom cell i-layer(s) can be increased arbitrarily to match the top cell current without electrical losses.

4. At last, it is assumed that improvements in the laser design reduce the series resistance so that the FF increases by 1% absolute.

The conversion efficiency in the tandem cell design is thus expected to be limited to below 13% on this type of TCO, mostly due to limitations related to the top cell current.

Keeping the above mentioned assumptions, the addition of further junctions is therefore now considered. This way, the limitations of a low top cell current can be circumvented. The following approach is based on a-Si:H/a-Si:H/μc-Si:H results, which are indicated as the starting point in 7.2. The layer thickness for this device were 70/320/60/700 nm for top cell i-layer/middle cell i-layer/IRL/bottom cell i-layer. The LID factor for this device, which was measured to be 10%, is assumed to remain at this value. The following further assumptions are made:

5. The introduction of the meanwhile optimized IRL yields an improvement of 0.3 mA/cm^2 in the middle cell.
6. The change from SnO_2:F to annealed ZnO:Al improves the a-Si:H/a-Si:H/μc-Si:H triple junction similarly to the change observed for a-Si:H/μc-Si:H tandems, which resulted in a gain of 0.4 for the top and 0.8 mA/cm^2 for the bottom cell, 8 mV in V_{oc} and -0.6% absolute in FF. The gains in top and bottom cell currents in the tandem cell are assumed to distribute evently above all a-Si:H and μc-Si:H sub cells.
7. By introducing a wide band gap top and a low band gap bottom cell, it is possible to shift 0.2 mA/cm^2 from the top to the middle cell. This approach is outlined in [115]
8. Through the deposition of a second μc-Si:H sub cell, the V_{oc} can be increased by another 500 mV without affecting the other parameters. The μc-Si:H sub cells are then increased arbitrarily to set the desired high mismatch in current to increase the FF. The rather low 500 mV shall already indicate that thick μc-Si:H sub-cell will be needed.

Table 7.2.: Predicted improvements for triple and quadruple cells on annealed ZnO:Al. The given I-V parameters are the *initial* values. The stable efficiency is calculated assuming a constant LID factor of 10.0%.

Assumption	TCO	$J_{sc,top}$	$J_{sc,mid}$	$J_{sc,bot}$	V_{oc}	FF	stable η
starting point (no AR)	SnO2:F	7.7	5.7	6.3	2224	78.7	9.0
BKM IRL (5.)			6	6			9.5
annealed ZnO:Al (6.)	an. ZnO:Al	7.9	6.2	7.1	2232	78.1	9.7
(1.-3.)		8.4	6.7		2240	80.1	10.8
wide gap/low gap (7.)		8.2	6.9			80.7	11.2
AR+Laser		8.4	7.1	7.5		81.7	11.7
2nd μc-Si:H sub cell (8.)		8.4	7.1	7.5	2740	81.7	14.3

It is thus believed that conversion efficiencies above 14% can be achieved for a-Si:H based multi junction solar cells. The total absorbed current would have to be well above 30 mA/cm^2, which however seems featheable for the high total silicon thickness. As the number of doped layers increases with the number of sub cells, the further optimization of wide band gap materials is a necessary prerequisite for these high efficiencies.

A. Appendix

Table A.1.: Simulation input parameters a-Si:H/μc-Si:H tandem cell

Parameter	TCp	TCi	TCn	BCp	BCi	BCn
Thickness (nm)	18	250	30	30	1600	25
Dielectric constant (-)	7.2	11.9	11.9	11.9	11.9	11.9
Electron affinity (eV)	3.9	4	4.05	4.05	4.05	4.05
Band gap (eV)	2	1.75	1.18	1.18	1.18	1.18
Effective DOS in CB(cm^{-3})	$1{\cdot}10^{20}$	$1{\cdot}10^{20}$	$1.4{\cdot}10^{21}$	$1.4{\cdot}10^{21}$	$1.4{\cdot}10^{21}$	$1.4{\cdot}10^{21}$
Effective DOS in VB (cm^{-3})	$1{\cdot}10^{20}$	$1{\cdot}10^{20}$	$5.2{\cdot}10^{20}$	$5.2{\cdot}10^{20}$	$5.2{\cdot}10^{20}$	$5.2{\cdot}10^{20}$
Electron mobility (cm^2/Vs)	20	20	50	50	50	50
Hole mobility (cm^2/Vs)	5	5	15	15	15	15
Field dependent mobilities	off	off	on, F_0=$2{\cdot}10^5$	on, F_0=$2{\cdot}10^5$	off	off
Doping concentration acceptors (cm^-3)	$5.5{\cdot}10^{18}$	0	0	$\cdot 10^{19}$	0	0
Doping concentration donators (cm^-3)	0	0	$3{\cdot}10^{19}$	0	0	$5{\cdot}10^{19}$

Parameter	TCp	TCi	TCn	BCp	BCi	BCn
Tail state parameters						
DOS at VB mobility edge (cm^{-3})	$9.00 \cdot 10^{19}$	$1.92 \cdot 10^{20}$	$3.22 \cdot 10^{20}$	$3.22 \cdot 10^{20}$	$3.22 \cdot 10^{18}$	$3.22 \cdot 10^{20}$
DOS at CB mobility edge (cm^{-3})	$3.60 \cdot 10^{20}$	$1.92 \cdot 10^{20}$	$8.68 \cdot 10^{20}0$	$8.68 \cdot 10^{20}$	$8.68 \cdot 10^{18}$	$8.68 \cdot 10^{20}$
$E_{U,VB}$ (eV)	0.09	0.037	0.031	0.031	0.031	0.031
$E_{U,CB}$ (eV)	0.05	0.02	0.031	0.031	0.031	0.031
$c^{zero}_{neutral}$ (cm^2)	$1 \cdot 10^{15}$	$1 \cdot 10^{15}$	$1 \cdot 10^{15}$	$1 \cdot 10^{15}$	$1 \cdot 10^{15}$	$1 \cdot 10^{15}$
$c^{zero}_{charged}$ (cm^2)	$1 \cdot 10^{15}$	$1 \cdot 10^{15}$	$1 \cdot 10^{15}$	$1 \cdot 10^{15}$	$1 \cdot 10^{15}$	$1 \cdot 10^{15}$
TAT	off	off	on, m_{eff}=0.1	on, m_{eff}=0.1	off	off
Dangling bond states						
Model	Gaussian distribution					
Position of E_V-$E^{+/0}_{db}$(eV)	1	0.775	0.49	0.49	0.49	0.49
Position of E_V-$E^{0/-}_{db}$(eV)	1.2	0.975	0.69	0.69	0.69	0.69
Standard deviation	0.144	0.144	0.15	0.15	0.15	0.15
$c^{zero}_{neutral}$ (cm^2)	$1 \cdot 10^{15}$	$1 \cdot 10^{15}$	$1 \cdot 10^{15}$	$1 \cdot 10^{15}$	$1 \cdot 10^{15}$	$1 \cdot 10^{15}$
$c^{zero}_{charged}$ (cm^2)	$1 \cdot 10^{15}$	$1 \cdot 10^{15}$	$1 \cdot 10^{15}$	$1 \cdot 10^{15}$	$1 \cdot 10^{15}$	$1 \cdot 10^{15}$
TAT	off	off	on, m_{eff}=0.1	on, m_{eff}=0.1	off	off

List of Figures

List of Tables

List of Symbols and Acronyms

Physical quantities	Name	Unit
α	Absorption coefficient	cm^{-1}
d_{el}	Electrode gap	mm
E_{04}	Optical band gap (Photon energy where α>10^4)	eV
E_a	Activation energy	eV
E_g	Band gap	eV
E_{Mob}	Mobility gap	eV
E_{Tauc}	Tauc gap	eV
EQE	External quantum efficiency	%
F_c	Raman crystallinity	%
F_0	FTM factor	$\left(\frac{\mathrm{V}}{\mathrm{cm}}\right)$
f_total	Total gas flow	sccm
FF	Fill factor	%
l_{AC}	Autocorrelation length	nm
k	Boltzmann constant	$\left(\frac{\mathrm{eV}}{\mathrm{k}}\right)$
LID	Light induced degradation factor	%
σ	Conductivity	$\left(\frac{\mathrm{S}}{\mathrm{cm}}\right)$
σ_{RMS}	Root mean square roughness	nm
P_{RF}	RF power	W
p	Deposition pressure	Pa
R	Reflection	%
R_{oc}	Differential resistance near open circuit conditions	$\Omega\,\mathrm{cm}^2$
R_p	Parallel resistance	$\Omega\,\mathrm{cm}^2$
R_s	Series resistance	$\Omega\,\mathrm{cm}^2$
R_{sc}	Differential resistance near short circuit conditions	$\Omega\,\mathrm{cm}^2$
R_{sc}	Differential resistance near short circuit conditions	$\Omega\,\mathrm{cm}^2$
R_{sheet}	Sheet resistance	$\Omega/\square$
T	Transmission	%
T	Temperature	K
V_{OC}	Open circuit voltage	V
η	Conversion efficiency	%

Acronyms and chemical descriptions

AFM	Atomic force microscopy
a-Si:H	(Hydrogenated) amorphous silicon
a-SiC_x:H	(Hydrogenated) amorphous silicon carbide
a-SiO_x:H	(Hydrogenated) amorphous silicon oxide
BCp, BCi, BCn,	Bottom cell p-, i- and n-layer
CB	Conduction band
DOS	Density of states
HCl	Hydrochloric acid
FTM	Field and temperature dependent mobilities
μc-Si:H	(Hydrogenated) microcrystalline silicon
μc-SiO_x:H	(Hydrogenated) microcrystalline silicon oxide
μc-SiC_x:H	(Hydrogenated) microcrystalline silicon carbide
PECVD	Plasma Enhanced Chemical Vapor Deposition
SnO_2:F	Fluor doped tin oxide
TAT	Trap assisted tunneling model
TCO	Transparent conducting oxide
TCp, TCi, TCn,	Top cell p-, i- and n-layer
VB	Valence band
ZnO:Al	Aluminum doped zinc oxide
ZnO:B	Boron doped zinc oxide

Bibliography

[1] MUNICH RE. *Climate and climate change*. Topics Geo p. 36 (2012).

[2] D. E. CARLSON and C. R. WRONSKI. *Amorphous silicon solar cell*. Applied Physics Letters **28**(11) 671 –673 (1976).

[3] M. FARAJI, S. GOKHALE, S. M. CHOUDHARI, M. G. TAKWALE and S. V. GHAISAS. *High mobility hydrogenated and oxygenated microcrystalline silicon as a photosensitive material in photovoltaic applications*. Applied Physics Letters **60**(26) 3289–3291 (1992).

[4] R. FLÜCKIGER, J. MEIER, H. KEPPNER, U. KROLL, A. S. O. GREIM, M. MORRIS, J. POHL, P. HAPKE and R. CARIUS. *Microcrystalline silicon prepared with the very high frequency glow discharge technique for p-i-n solar cell applications*. In *Proc. of the 11th EC Photovoltaic Solar Energy Conférence*, p. 617 (1992).

[5] J. MEIER, P. TORRES, PLATZ, R. S. DUBAIL, U. KROLL, J. A. ANNA SELVAN, N. PELLATON VAUCHER, CH. HOF, D. FISCHER, H. KEPPNER, A. SHAH, K. D. UFERT, GIANNOULÈS P. and J. KOEHLER. *On the Way Towards High Efficiency Thin Film Silicon Solar Cells by the 'Micromorph' Concept*. In *MRS Proceedings*, p. 420 (1996).

[6] U. KROLL, J. MEIER, L. FESQUET, J. STEINHAUSER, S. BENAGLI, J.B ORHAN, B. WOLF, D. BORRELLO, L. CASTENS, Y. DJERIDANE, X. MULTONE, G. CHOONG, D. DOMINE, J.-F. BOUCHER, P.-A. MADLIGER, M. MARMELO, G. MONTEDURO, B. DEHBOZORGI, D. ROMANG, E. OMNES, M. CHEVALLEY, G. CHARITAT, A. POMEY, E. VALLAT-SAUVAIN, S. MARJANOVIC, G. KOHNKE, K. KOCH, J. LIU, R. MODAVIS, D. THELEN, S. VALLON, A. ZAKHARIAN and D. WEIDMAN. *Recent Developments of High-Efficiency Micromorph Tandem Solar Cells in KAI-M/ Plasmabox PECVD Reactors*. In *Proceedings of the 26th European Photovoltaic Solar Energy Conference and Exhibition (3BO.2.6)* (2011).

[7] S. W. AHN, S. E. LEE and H. M. LEE. *Toward commercialization of triple-junction thin-film silicon solar panel with >12% efficiency*. In *27th European Photovoltaic Solar Energy Conference, 3AO5.1, Frankfurt* (2012).

[8] D. L. STAEBLER and C. R. WRONSKI. *Reversible conductivity changes in discharge-produced amorphous Si*. Applied Physics Letters **31**(4) 292–294 (1977).

[9] K. YAMAMOTO, M. YOSHIMI, Y. TAWADA, S. FUKUDA, T. SAWADA, T. MEGURO, H. TAKATA, T. SUEZAKI, Y. KOI, K. HAYASHI, T. SUZUKI, M. ICHIKAWA and A. NAKAJIMA. *Large area thin film Si module*. Solar Energy Materials and Solar Cells **74**(1-4) 449 – 455 (2002).

[10] P. BUEHLMANN, J. BAILAT, D. DOMINÉ, A. BILLET, F. MEILLAUD, A. FELTRIN and C. BALLIF. *In situ silicon oxide based intermediate reflector for thin-film silicon micromorph solar cells*. Applied Physics Letters **91**(14) 143505 (2007).

[11] A. LAMBERTZ, T. GRUNDLER and F. FINGER. *Hydrogenated amorphous silicon oxide containing a microcrystalline silicon phase and usage as an intermediate reflector in thin-film silicon solar cells*. Journal of Applied Physics **109**(11) 113109 (2011).

[12] Y. TAWADA, H. OKAMOTO and Y. HAMAKAWA. *a-SiC:H/a-Si:H heterojunction solar cell having more than 7.1conversion efficiency*. Applied Physics Letters **39**(3) 237–239 (1981).

[13] P. SICHANUGRIST, T. SASAKI, A. ASANO, Y. ICHIKAWA and H. SAKAI. *Amorphous silicon oxide and its application to metal/n-i-p/ITO type a-Si solar cells*. Solar Energy Materials and Solar Cells **34**(1 - 4) 415 – 422 (1994).

[14] S. KLEIN, R. CARIUS, F. FINGER and L. HOUBEN. *Low substrate temperature deposition of crystalline SiC using HWCVD*. Thin Solid Films **501**(1 - 2) 169 – 172 (2006).

[15] P. CUONY, D. T. L. ALEXANDER, I. PEREZ-WURFL, M. DESPEISSE, G. BUGNON, M. BOCCARD, T. SÖDERSTRÖM, A. HESSLER-WYSER, C. HÉBERT and C.S BALLIF. *Silicon Filaments in Silicon Oxide for Next-Generation Photovoltaics*. Advanced Materials **24**(9) 1182–1186 (2012).

[16] M. J. KEEVERS, T. L. YOUNG, U. SCHUBERT and M. A. GREEN. *10% Efficient CSG Minimodules*. In *Proceedings of the 22nd European Photovoltaic Solar Energy Conference, Milan* (2007).

[17] J. DORE, R. EVANS, B. D. EGGLESTON, S. VARLAMOV and M. A. GREEN. *Intermediate Layers for Thin-Film Polycrystalline Silicon Solar Cells on Glass Formed by Diode Laser Crystallization*. In *Proceedings of the Materials Research Society Spring Meeting, San Francisco* (2012).

[18] D. AMKREUTZ, J. MÜLLER, M. SCHMIDT, T. HÄNEL and T. F. SCHULZE. *Electron-beam crystallized large grained silicon solar cell on glass substrate*. Progress in Photovoltaics: Research and Applications **19**(8) 937 – 945 (2011).

[19] B. RECH, O. KLUTH, T. REPMANN, T. ROSCHEK, J. SPRINGER, J. MÜLLER, F. FINGER, H. STIEBIG and H. WAGNER. *New materials and deposition techniques for highly efficient silicon thin film solar cells*. Solar Energy Materials and Solar Cells **74**(1-4) 439 – 447 (2002).

[20] F. FINGER, J. MÜLLER, C. MALTEN, R. CARIUS and H. WAGNER. *Electronic properties of microcrystalline silicon investigated by electron spin resonance and transport measurements*. Journal of Non-Crystalline Solids **266** 511–518 (2000).

[21] T. ROSCHEK, B. RECH, J. MÜLLER, R. SCHMITZ and H. WAGNER. *Influence of the total gas flow on the deposition of microcrystalline silicon solar cells*. Thin Solid Films **451 - 452**(0) 466 – 469 (2004).

[22] B. RECH, T. REPMANN, M. N. VAN DEN DONKER, M. BERGINSKI, T. KILPER, J. HÜPKES, S. CALNAN, H. STIEBIG and S. WIEDER. *Challenges in microcrystalline silicon based solar cell technology*. Thin Solid Films **511-512**(0) 548 – 555 (2006).

[23] D. FISCHER, S. DUBAIL, J. A. ANNA SELVAN, N. PELLATON VAUCHER, R. PLATZ, CH. HOF, U. KROLL, J. MEIER, P. TORRES, H. KEPPNER, N. WYRSCH, M. GOETZ, A. SHAH and K.-D. UFERT. *The 'Micromorph' Solar Cell: Extending a-Si:H Technology Towards Thin Film Crystalline Silicon*. In *25th PVSC; May 13-17, Washington, D.C* (1996).

[24] J. MEIER, S. DUBAIL, J. CUPERUS, U. KROLL, R. PLATZ, P. TORRES, J. A. ANNA SELVAN, P. PERNET, N. BECK, N. PELLATON VAUCHER, CH. HOF, D. FISCHER, H. KEPPNER and A. SHAH. *Recent progress in micromorph solar cells*. Journal of Non-Crystalline Solids **227-230, Part 2**(0) 1250 – 1256 (1998).

[25] M. DESPEISSE, G. BUGNON, A. FELTRIN, M. STUECKELBERGER, P. CUONY, F. MEILLAUD, A. BILLET and C. BALLIF. *Resistive interlayer for improved performance of thin film silicon solar cells on highly textured substrate*. Applied Physics Letters **96**(7) 073507 (2010).

[26] R. E. I. SCHROPP and M. ZEMAN. *Amorphous and Microcrystalline Silicon Solar Cells: Modeling, Materials, and Device Technology*. Electronic Materials Series. Kluwer Academic (1998).

[27] A. V. SHAH and C. DROZ. *Thin-film Silicon: Photovoltaics and Large-area Electronics*. Engineering Sciences: Micro- And Nanotechnology. Taylor & Francis (2009).

[28] M. A. LIEBERMAN and A. J. LICHTENBERG. *Principles of Plasma Discharges and Materials Processing*. Wiley (2005).

[29] R. A. STREET. *Hydrogenated Amorphous Silicon*. Cambridge Solid State Science Series. Cambridge University Press (2005).

[30] H. F. STERLING and R. C. G. SWANN. *Chemical vapour deposition promoted by r.f. discharge*. Solid-State Electronics **8**(8) 653 – 654 (1965).

[31] M. STUTZMANN, W. B. JACKSON and C. C. TSAI. *Light-induced metastable defects in hydrogenated amorphous silicon: A systematic study*. Phys. Rev. B **32** 23–47 (Jul 1985).

[32] W. E. SPEAR and P. G. LE COMBER. *Substitutional doping of amorphous silicon*. Solid State Communications **17**(9) 1193 – 1196 (1975).

[33] O. VETTERL, F. FINGER, R. CARIUS, P. HAPKE, L. HOUBEN, O. KLUTH, A. LAMBERTZ, A. MÜCK, B. RECH and H. WAGNER. *Intrinsic microcrystalline silicon: A new material for photovoltaics*. Solar Energy Materials and Solar Cells **62**(1) 97 – 108 (2000).

[34] S. USUI and M. KIKUCHI. *Properties of heavily doped GD-Si with low resistivity*. Journal of Non-Crystalline Solids **34**(1) 1 – 11 (1979).

[35] B. RECH, T. ROSCHEK, T. REPMANN, J. MÜLLER, R. SCHMITZ and W. APPENZELLER. *Microcrystalline silicon for large area thin film solar cells*. Thin Solid Films **427**(1 - 2) 157 – 165 (2003).

[36] C. DROZ, E. VALLAT-SAUVAIN, J. BAILAT, L. FEITKNECHT, J. MEIER and A. SHAH. *Relationship between Raman crystallinity and open-circuit voltage in microcrystalline silicon solar cells*. Solar Energy Materials and Solar Cells **81**(1) 61 – 71 (2004).

[37] F FINGER, L. B. NETO, T. CARIUS, R.AND DYLLA and S KLEIN. *Paramagnetic defects in undoped microcrystalline silicon*. Physica Status Solidi (c) **1** 1248–1254 (2004).

[38] A.E. DELAHOY. *Recent developments in amorphous silicon photovoltaic research and manufacturing at chronar corporation*. Solar Cells **27**(1 - 4) 39 – 57 (1989).

[39] J. YANG, A. BANERJEE and S. GUHA. *Triple-junction amorphous silicon alloy solar cell with 14.6% initial and 13.0% stable conversion efficiencies*. Applied Physics Letters **70**(22) 2975–2977 (1997).

[40] B. YAN, G. YUE, L. SIVEC, J. YANG, S. GUHA and C. JIANG. *Innovative dual function nc-SiO_x:H layer leading to a > 16% efficient multi-junction thin-film silicon solar cell*. Applied Physics Letters **99**(11) 113512 (2011).

[41] J. SPRINGER, A. PORUBA and M. VANECEK. *Improved three-dimensional optical model for thin-film silicon solar cells*. Journal of Applied Physics **96**(9) 5329–5337 (2004).

[42] F. FINGER, O. ASTAKHOV, T. BRONGER, R. CARIUS, T. CHEN, A. DASGUPTA, A. GORDIJN, L. HOUBEN, Y. HUANG, S. KLEIN, M. LUYSBERG, H. WANG and L. XIAO. *Microcrystalline silicon carbide alloys prepared with HWCVD as highly transparent and conductive window layers for thin film solar cells*. Thin Solid Films **517**(12) 3507 – 3512 (2009).

[43] S. M. SZE and K. K. NG. *Physics of Semiconductor Devices*. Wiley (2006).

[44] A. R. DENTON and N. W. ASHCROFT. *Vegard's law*. Phys. Rev. A **43** 3161–3164 (Mar 1991).

[45] R. JANSSEN, A. JANOTTA, D. DIMOVA-MALINOVSKA and M. STUTZMANN. *Optical and electrical properties of doped amorphous silicon suboxides*. Phys. Rev. B **60** 13561–13572 (Nov 1999).

[46] F. DEMICHELIS, C. F. PIRRI and E. TRESSO. *Microcrystallization formation in silicon carbide thin films*. Philosophical Magazine Part B **66**(1) 135–146 (1992).

[47] F. DEMICHELIS, C. F. PIRRI and E. TRESSO. *Influence of doping on the structural and optoelectronic properties of amorphous and microcrystalline silicon carbide*. Journal of Applied Physics **72**(4) 1327–1333 (1992).

[48] S. SCHREIBER. *Untersuchungen zum epitaktischen Wachstum von 3C-SiC bei Verwendung einer C60-Kohlenstoffquelle*. Dissertation, TU Augsburg (2007).

[49] A. CATALANO, R. V. D'AIELLO, J. DRESNER, B. FAUGHNAN, A. FIRESTER, J. KANE, H. SCHADE, G. SCHWARTZ, Z.E. SMITH and A. TRIANO. *Attainment of 10solar cells*. In *Conference Rececord of the 16th IEEE Photovoltaic Specialsists Conference*. (1982).

[50] Y. TAWADA, M. KONDO, H. OKAMOTO and Y. HAMAKAWA. *Hydrogenated amorphous silicon carbide as a window material for high efficiency a-Si solar cells*. Solar Energy Materials **6**(3) 299 – 315 (1982).

[51] P. CUONY, M. MARENDING, D. T. L. ALEXANDER, M. BOCCARD, G. BUGNON, M. DESPEISSE and C. BALLIF. *Mixed-phase p-type silicon oxide containing silicon nanocrystals and its role in thin-film silicon solar cells*. Applied Physics Letters **97**(21) 213502 (2010).

[52] K. SCHWANITZ, S. KLEIN, T. STOLLEY, M. ROHDE, D. SEVERIN and R. TRASSL. *Anti-reflective microcrystalline silicon oxide p-layer for thin-film silicon solar cells on ZnO*. Solar Energy Materials and Solar Cells **105**(0) 187 – 191 (2012).

[53] S. Y. MYONG, K. S. LIM and J. M. PEARS. *Double amorphous silicon-carbide p-layer structures producing highly stabilized pin-type protocrystalline silicon multilayer solar cells*. Applied Physics Letters **87**(19) 193509 (2005).

[54] Y. XU, B. NEMETH, F. HASOON, L. HONG, A. DUDA and Q. WANG. *P-layer Optimization in High Performance a-Si:H Solar Cells*. MRS Online Proceedings Library **1245** (0 2010).

[55] O. VETTERL, A. LAMBERTZ, A. DASGUPTA, F. FINGER, B. RECH, O. KLUTH and H. WAGNER. *Thickness dependence of microcrystalline silicon solar cell properties*. Solar Energy Materials and Solar Cells **66**(1 - 4) 345 – 351 (2001).

[56] M. S. BENNETT, J. L. NEWTON and K. RAJAN. *The Influence of Electric Field on Stability*. In *Proc. of the 7th EC PVSEC, Sevilla*, p. 544 – 547 (1986).

[57] B. RECH and H. WAGNER. *Potential of amorphous silicon for solar cells*. Applied Physics A **69** 155–167 (1999).

[58] R. S. CRANDALL. *Transport in hydrogenated amorphous silicon p-i-n solar cells*. Journal of Applied Physics **53**(4) 3350–3352 (1982).

[59] SIR NEVILL FRANCIS MOTT and EDWARD ARTHUR DAVIS. *Electronic processes in non-crystalline materials*. Oxford : Clarendon Press ; New York : Oxford University Press, 2nd ed edition (1979). Includes index.

[60] M. ZEMAN, J. A. WILLEMEN, L. L. A. VOSTEEN, G. TAO and J. W. METSELAAR. *Computer modelling of current matching in a-Si : H/a-Si : H tandem solar cells on textured TCO substrates*. Solar Energy Materials and Solar Cells **46**(2) 81 – 99 (1997).

[61] OERLIKON SOLAR. *Oerlikon Solar Presents Record Cell Efficiency confirmed by NREL*. Media Release (2010).

[62] S. HÄNNI, D. T. L. ALEXANDER, L. DING, G. BUGNON, M. BOCCARD, C. BATTAGLIA, P. CUONY, J. ESCARRE, G. PARASCANDOLO, S. NICOLAY, M. CANTONI, M. DESPEISSE, F. MEILLAUD and C. BALLIF. *On the Interplay Between Microstructure and Interfaces in High-Efficiency Microcrystalline Silicon Solar Cells*. IEEE Journal of Photovoltaics **3**(1) 11 –16 (2013).

[63] Y. ICHIKAWA, S. FUJIKAKE, T. YOSHIDA, T. HAMA and H. SAKAI. *A stable 10% solar cell with a-Si/a-Si double junction structure*. In *Photovoltaic Specialists Conference, 1990., Conference Record of the Twenty First IEEE*, p. 1475 –1480 vol.2 (may 1990).

[64] T. SONTHEIMER, C. BECKER, U. BLOECK, S. GALL and B. RECH. *Crystallization kinetics in electron-beam evaporated amorphous silicon on ZnO:Al-coated glass for thin film solar cells*. Applied Physics Letters **95**(10) 101902 (2009).

[65] C. BECKER, F. RUSKE, T. SONTHEIMER, B. GORKA, U. BLOECK, S. GALL and B. RECH. *Microstructure and photovoltaic performance of polycrystalline silicon thin films on temperature-stable ZnO:Al layers*. Journal of Applied Physics **106**(8) 084506 (2009).

[66] S. GALL, C. BECKER, K. Y. LEE, T. SONTHEIMER and B. RECH. *Growth of polycrystalline silicon on glass for thin-film solar cells*. Journal of Crystal Growth **312**(8) 1277 – 1281 (2010).

[67] V. SMIRNOV, A. LAMBERTZ, B. GROOTOONK, R. CARIUS and F. FINGER. *Microcrystalline silicon oxide (μc-SiOx:H) alloys: A versatile material for application in thin film silicon single and tandem junction solar cells*. Journal of Non-Crystalline Solids **358**(17) 1954 – 1957 (2012).

[68] J. ZHAO, A. WANG, M. A. GREEN and F. FERRAZZA. *19.824.4 Applied Physics Letters* **73***(14) 1991–1993 (1998).*

[69] E. YABLONOVITCH. Statistical ray optics. *J. Opt. Soc. Am.* **72***(7) 899–907 (Jul 1982).*

[70] S. KUMAR *and* B. DREVILLON. A real time ellipsometry study of the growth of amorphous silicon on transparent conducting oxides. *Journal of Applied Physics* **65***(8) 3023–3034 (1989).*

[71] J. K. RATH *and* R. E. I. SCHROPP. Incorporation of p-type microcrystalline silicon films in amorphous silicon based solar cells in a superstrate structure. *Solar Energy Materials and Solar Cells* **53***(1 - 2) 189 – 203 (1998).*

[72] C. ROCKSTUHL, S. FAHR, K. BITTKAU, T. BECKERS, R. CARIUS, F.-J. HAUG, T. SÖDERSTRÖM, C. BALLIF *and* F. LEDERER. Comparison and optimization of randomly textured surfaces in thin-film solar cells. *Opt. Express* **18***(S3) A335–A341 (Sep 2010).*

[73] B. LIPOVSEK, M. CVEK, A. CAMPA, J. KRC *and* M. TOPIC. Analysis and Optimisation of Periodic Interface Textures in Thin-Film Silicon Solar Cells. *In* 25th European Photovoltaic Solar Energy Conference and Exhibition / 5th World Conference on Photovoltaic Energy Conversion, 6-10 September 2010, Valencia, Spain *(2010).*

[74] H. B. T. LI, K. H. M. VAN DER WERF, J. K. RATH *and* R. E. I. SCHROPP. Hot wire CVD deposition of nanocrystalline silicon solar cells on rough substrates. *Thin Solid Films* **517***(12) 3476 – 3480 (2009).*

[75] M. PYTHON, O. MADANI, D. DOMINÉ, F. MEILLAUD, E. VALLAT-SAUVAIN *and* C. BALLIF. Influence of the substrate geometrical parameters on microcrystalline silicon growth for thin-film solar cells. *Solar Energy Materials and Solar Cells* **93***(10) 1714 – 1720 (2009).*

[76] N. PELLATON VAUCHER, J.-L. NAGEL, R. PLATZ, D. FISCHER *and* A. SHAH. Light Management in Tandem Cells by An Intermediate Reflector Layer. *In* 2nd World Conference and Exhibition on Photovoltaic Solar Energy Conversion, 6-10 July 1998, Austria *(1998).*

[77] D. DOMINÉ. The Role of Front Electrodes and Intermediate Reflectors in the Optoelectronic Properties of High-efficiency Micromorph Solar Cells. *Dissertation, Université de Neuchâtel (2009).*

[78] C. ROCKSTUHL, F. LEDERER, K. BITTKAU, T. BECKERS *and* R. CARIUS. The impact of intermediate reflectors on light absorption in tandem solar cells with randomly textured surfaces. *Applied Physics Letters* **94***(21) 211101 (2009).*

[79] T. VAN MOL. Chemical Vapor Deposition of Tin Oxide Thin Films. *Dissertation, TU Eindhoven (2003).*

[80] O. KLUTH, B. RECH, L. HOUBEN, S. WIEDER, G. SCHÖPE, C. BENEKING, H. WAGNER, A. LÖFFL *and* H. W. SCHOCK. Texture etched ZnO:Al coated glass substrates for silicon based thin film solar cells. *Thin Solid Films* **351***(1 - 2) 247 – 253 (1999).*

[81] B. SZYSZKA, V. SITTINGER, X. JIANG, R.J. HONG, W. WERNER, A. PFLUG, M. RUSKE *and* A. LOPP. Transparent and conductive ZnO:Al films deposited by large area reactive magnetron sputtering. *Thin Solid Films* **442***(12) 179 – 183 (2003).*

[82] J. MÜLLER, B. RECH, J. SPRINGER *and* M. VANECEK. TCO and light trapping in silicon thin film solar cells. *Solar Energy* **77***(6) 917 – 930 (2004).*

[83] M. BERGINSKI, J. HÜPKES, M. SCHULTE, G. SCHOPE, H. STIEBIG, B. RECH *and* M. WUTTIG. The effect of front ZnO:Al surface texture and optical transparency on efficient light trapping in silicon thin-film solar cells. *Journal of Applied Physics* **101***(7) 074903–074903–11 (2007).*

[84] H. ZHU, J. HÜPKES, E. BUNTE, J. OWEN *and* S. M. HUANG. Novel etching method on high rate ZnO:Al thin films reactively sputtered from dual tube metallic targets for silicon-based solar cells. *Solar Energy Materials and Solar Cells* **95***(3) 964 – 968 (2011).*

[85] F. RUSKE, M. ROCZEN, K. LEE, M. WIMMER, S. GALL, J. HUPKES, D. HRUNSKI *and* B. RECH. Improved electrical transport in Al-doped zinc oxide by thermal treatment. *Journal of Applied Physics* **107***(1) 013708 –013708–8 (jan 2010).*

[86] M. WIMMER, F. RUSKE, S. SCHERF *and* B. RECH. Improving the electrical and optical properties of DC-sputtered ZnO:Al by thermal post deposition treatments. *Thin Solid Films* **520***(12) 4203 – 4207 (2012).*

[87] S. NEUBERT, M. WIMMER, F. RUSKE, S. CALNAN, O. GABRIEL, B. STANNOWSKI, R. SCHLATMANN *and* B. RECH. Improved conversion efficiency of a-Si:H/μc-Si:H thin-film solar cells by using annealed Al-doped zinc oxide as front electrode material. *Progress in Photovoltaics: Research and Applications (2013).*

[88] S. FAY, J. STEINHAUSER, S. NICOLAY *and* C. BALLIF. Polycrystalline ZnO: B grown by LPCVD as TCO for thin film silicon solar cells. *Thin Solid Films* **518***(11) 2961 – 2966 (2010).*

[89] A. LAMBERTZ, A. DASGUPTA, W. REETZ, A. GORDIJN, R. CARIUS *and* F. FINGER. Microcrystalline Silicon Oxide as Intermediate Reflector for Thin Film Silicon Solar Cells. *In* Proceedings of the 22nd EUPVSEC (European Photovoltaic Solar Energy Conference), *p. 1839–1842 (2007).*

[90] M. KONDO, M. FUKAWA, L. H. GUO *and* A. MATSUDA. High rate growth of microcrystalline silicon at low temperatures. *Journal of Non-Crystalline Solids* **266-269***(Part a) 84–89 (MAY 2000).*

[91] J. PERRIN, O. LEROY *and* M. C. BORDAGE. Cross-Sections, Rate Constants and Transport Coefficients in Silane Plasma Chemistry. *Contributions to Plasma Physics* **36***(1) 3–49 (1996).*

[92] U. KROLL, J. MEIER, A. SHAH, S. MIKHAILOV *and* J. WEBER. Hydrogen in amorphous and microcrystalline silicon films prepared by hydrogen dilution. *Journal of Applied Physics* **80***(9) 4971–4975 (1996).*

[93] A. MATSUDA. Formation kinetics and control of microcrystallite in μc-Si:H from glow discharge plasma. *Journal of Non-Crystalline Solids* **59 - 60, Part 2***(0) 767 – 774 (1983).*

[94] C. C. TSAI, G. B. ANDERSON, R. THOMPSON *and* B. WACKER. Control of silicon network structure in plasma deposition. *Journal of Non-Crystalline Solids* **114, Part 1***(0) 151 – 153 (1989).*

[95] K. NAKAMURA, K. YOSHINO, S. TAKEOKA *and* I. SHIMIZU. Roles of Atomic Hydrogen in Chemical Annealing. *Japanese Journal of Applied Physics* **34***(Part 1, No. 2A) 442–449 (1995).*

[96] A. MATSUDA. Growth mechanism of microcrystalline silicon obtained from reactive plasmas. *Thin Solid Films* **337***(1 - 2) 1 – 6 (1999).*

[97] T. ROSCHEK, T. REPMANN, J. MÜLLER, B. RECH *and* H. WAGNER. Comprehensive study of microcrystalline silicon solar cells deposited at high rate using 13.56 MHz plasma-enhanced chemical vapor deposition. *Journal of Vacuum Science & Technology A: Vacuum, Surfaces, and Films* **20***(2) 492–498 (2002).*

[98] T. MATSUI, M. KONDO *and* A. MATSUDA. Origin of the improved performance of high-deposition-rate microcrystalline silicon solar cells by high-pressure glow discharge. *Japanese Journal of Applied Physics, Part 2 - Letters* **42***(8A) L901–L903 (AUG 1 2003).*

[99] T. REPMANN. Solarzellen aus amorphem und mikrokristallinem Silizium. *Dissertation, RWTH Aachen, Jülich (2003).* `http://jwel.fz-juelich.de:8080/dspace/bitstream/2128/256/1/Juel_4082_Repmann.pdf`.

[100] S. M. IFTIQUAR. The roles of deposition pressure and rf power in opto-electronic properties of a-SiO:H films. *Journal of Physics D: Applied Physics* **31***(14) 1630 (1998).*

[101] J. PERRIN. Deposition of amorphous silicon alloys. *Pure Appl. Chem.* **62** *1681 – 1688 (1990).*

[102] J. MEIER, U. KROLL, E. VALLAT-SAUVAIN, J. SPITZNAGEL, U. GRAF *and* A. SHAH. Amorphous solar cells, the micromorph concept and the role of VHF-GD deposition technique. *Solar Energy* **77***(6) 983 – 993 (2004).*

[103] TOBIAS ROSCHEK. Microcrystalline Silicon Solar Cells Prepared by 13.56 MHz PECVD. *Dissertation, Universität Düsseldorf (2003).*

[104] Y. GUPTA, H. LIERS, S. WOODS, S. YOUNG, R. DEBLASIO *and* L. MRIG. Optimization of a-Si solar cell current collection. *In* 16th Photovoltaic Specialists Conference, *p. 1092–1101 (1982).* `http://adsabs.harvard.edu/abs/1982pvsp.conf.1092G` *Provided by the SAO/NASA Astrophysics Data System.*

[105] J. SPRINGER, A. PORUBA, L. MULLEROVA, M. VANECEK, O. KLUTH *and* B. RECH. Absorption loss at nanorough silver back reflector of thin-film silicon solar cells. *Journal of Applied Physics* **95***(3) 1427–1429 (2004).*

[106] M. PAULI, J. MULLER, K. HARTKOPF *and* T. BARTH. A line beam electron gun for rapid thermal processing. *Review of Scientific Instruments* **63***(4) 2288–2295 (1992).*

[107] F. GROMBALL, C. GROTH *and* J. MULLER. Controlled line shaped electron beam for silicon zone melting recrystallization on float glass substrates. *Review of Scientific Instruments* **76***(6) 063901 (2005).*

[108] B. HARBECKE. Coherent and incoherent reflection and transmission of multilayer structures. *Applied Physics B* **39** *165–170 (1986).*

[109] G. E. JELLISON *and* F. A. MODINE. Parameterization of the optical functions of amorphous materials in the interband region. *Applied Physics Letters* **69***(3) 371 –373 (jul 1996).*

[110] D. A. G. BRUGGEMAN. Berechnung verschiedener physikalischer Konstanten von heterogenen Substanzen. I. Dielektrizitïätskonstanten und Leitfäigkeiten der Mischkörper aus isotropen Substanzen. *Annalen der Physik* **416***(7) 636–664 (1935).*

[111] M. LOSURDO, M. M. GIANGREGORIO, P. CAPEZZUTO, G. BRUNO, M. F. CERQUEIRA, E. ALVES *and* M. STEPIKHOVA. Dielectric function of nanocrystalline silicon with few nanometers ([less-than] 3 nm) grain size. *Applied Physics Letters* **82***(18) 2993–2995 (2003).*

[112] S. K. RAM, MD. N. ISLAM, P. R. I CABARROCAS *and* S. KUMAR. Structural determination of nanocrystalline Si films using ellipsometry and Raman spectroscopy. *Thin Solid Films* **516***(20) 6863 – 6868 (2008).*

[113] Y. HISHIKAWA, N. NAKAMURA, S. TSUDA, S. NAKANO, Y. KISHI *and* Y. KUWANO. Interference-Free Determination of the Optical Absorption Coefficient and the Optical Gap of Amorphous Silicon Thin Films. *Japanese Journal of Applied Physics* **30***(Part 1, No. 5) 1008–1014 (1991).*

[114] A. SHAH. Thin-Film Silicon Solar Cells: Photovoltaics and Large-Area Electronics. *Engineering Sciences: Micro- And Nanotechnology. Efpl Press (2010).*

[115] B. RECH. Solarzellen aus amorphem Silizium mit hohem stabilem Wirkungsgrad. *Dissertation, RWTH Aachen (1997).*

[116] X. XU, J. YANG, A. BANERJEE, S. GUHA, K. VASANTH *and* S. WAGNER. Band edge discontinuities between microcrystalline and amorphous hydrogenated silicon alloys and their effect on solar cell performance. *Applied Physics Letters* **67***(16) 2323–2325 (1995).*

[117] S. HAMMA *and* P. ROCA I CABARROCAS. Determination of the mobility gap of microcrystalline silicon and of the band discontinuities at the amorphous/microcrystalline silicon interface using in situ Kelvin probe technique. *Applied Physics Letters* **74***(21) 3218–3220 (1999).*

[118] B. E. PIETERS, H. STIEBIG, M. ZEMAN *and* R. A. C. M. M. VAN SWAAIJ. Determination of the mobility gap of intrinsic mu c-Si:H in p-i-n solar cells. *Journal of Applied Physics* **105***(4) 044502 (2009).*

[119] H. H. BERGER. Models for contacts to planar devices. *Solid-State Electronics* **15***(2) 145 – 158 (1972).*

[120] M. H. BRODSKY, MANUEL CARDONA *and* J. J. CUOMO. Infrared and Raman spectra of the silicon-hydrogen bonds in amorphous silicon prepared by glow discharge and sputtering. *Phys. Rev. B* **16** *3556–3571 (Oct 1977).*

[121] D. W. FELDMAN, JAMES H. PARKER, W. J. CHOYKE *and* LYLE PATRICK. Phonon Dispersion Curves by Raman Scattering in SiC, Polytypes 3*C*, 4*H*, 6*H*, 15*R*, and 21*R*. *Phys. Rev.* **173** *787–793 (Sep 1968).*

[122] S. NAKASHIMA *and* H. HARIMA. Raman Investigation of SiC Polytypes. *physica status solidi (a)* **162***(1) 39–64 (1997).*

[123] J. C. BURTON, L. SUN, M. POPHRISTIC, S. J. LUKACS, F. H. LONG, Z. C. FENG *and* I. T. FERGUSON. Spatial characterization of doped SiC wafers by Raman spectroscopy. *Journal of Applied Physics* **84***(11) 6268–6273 (1998).*

[124] C. SMIT, R. A. C. M. M. VAN SWAAIJ, H. DONKER, A. M. H. N. PETIT, W. M. M. KESSELS *and* M. C. M. VAN DE SANDEN. Determining the material structure of microcrystalline silicon from Raman spectra. *Journal of Applied Physics* **94***(5) 3582–3588 (2003).*

[125] J. S. LANNIN, L. J. PILIONE, S. T. KSHIRSAGAR, R. MESSIER *and* R. C. ROSS. Variable structural order in amorphous silicon. *Phys. Rev. B* **26** *3506–3509 (Sep 1982).*

[126] R. J. NEMANICH, J. T. GLASS, G. LUCOVSKY *and* R. E. SHRODER. Raman scattering characterization of carbon bonding in diamond and diamondlike thin films. *Journal of Vacuum Science & Technology A: Vacuum, Surfaces, and Films* **6***(3) 1783–1787 (1988).*

[127] S. SORIEUL, J.-M. COSTANTINI, L. GOSMAIN, L. THOMÉ *and* J.-J. GROB. Raman spectroscopy study of heavy-ion-irradiated α-SiC. *Journal of Physics: Condensed Matter* **18***(22) 5235 (2006).*

[128] L. HOUBEN, M. LUYSBERG, P. HAPKE, R. CARIUS, F. FINGER *and* H. WAGNER. Structural properties of microcrystalline silicon in the transition from highly crystalline to amorphous growth. *Philosophical Magazine A* **77***(6) 1447–1460 (1998).*

[129] R. TSU, J. GONZALEZ-HERNANDEZ, S. S. CHAO, S. C. LEE *and* K. TANAKA. Critical volume fraction of crystallinity for conductivity percolation in phosphorus-doped Si:F:H alloys. *Applied Physics Letters* **40***(6) 534–535 (1982).*

[130] E. BUSTARRET, M. A. HACHICHA *and* M. BRUNEL. Experimental determination of the nanocrystalline volume fraction in silicon thin films from Raman spectroscopy. *Applied Physics Letters* **52***(20) 1675–1677 (1988).*

[131] H. RICHTER, Z. P. WANG *and* L. LEY. The one phonon Raman spectrum in microcrystalline silicon. *Solid State Communications* **39***(5) 625 – 629 (1981).*

[132] P. CHATTERJEE. Photovoltaic performance of a-Si:H homojunction p-i-n solar cells: A computer simulation study. *Journal of Applied Physics* **76***(2) 1301–1313 (1994).*

[133] A. STURIALE, H. T. LI, J. K. RATH, R. E. I. SCHROPP *and* F. A. RUBINELLI. Exploring dark current voltage characteristics of micromorph silicon tandem cells with computer simulations. *Journal of Applied Physics* **106***(1) 014502 (2009).*

[134] T. HAENEL. Spannungs- und intensitaetsabhaengige spektrale Empfindlichkeit von poly-Si Duennschichtsolarzellen. *Diplomarbeit, FHTW Berlin (2008).*

[135] K. DING, T. KIRCHARTZ, B. E. PIETERS, C. ULBRICH, A. M. ERMES, S. SCHICHO, A. LAMBERTZ, R. CARIUS *and* U. RAU. Characterization and simulation of a-Si:H/μc-Si:H tandem solar cells. *Solar Energy Materials and Solar Cells* **95***(12) 3318 – 3327 (2011).*

[136] J. MÜLLER, G. SCHOPE, B. RECH, H. SCHADE, P. LECHNER, R. GEYER, H. STIEBIG *and* W. REETZ. Role of the glass/TCO substrate in thin film silicon solar cells. *In* PROCEEDINGS OF 3RD WORLD CONFERENCE ON PHOTOVOLTAIC ENERGY CONVERSION, VOLS A-C, *p. 1839–1842 (2003).*

[137] D. DAS, S. MANDAL *and* A. K. BARUA. Intrinsic Hydrogenated Microcrystalline Silicon Oxide Films Prepared by RF Glow Discharge. *Journal of Materials Science Letters* **17***(Number 24) 2097–2100 (1998).*

[138] S. KLEIN, S. WIEDER, S. BUSCHBAUM, M. ROHDE, K. SCHWANITZ, T. STOLLEY, C. STÖMMER, D. SEVERIN, A. STRAUB, U. I. SCHMIDT *and* K. AHMED. Large area thin film silicon modules with 10 per cent efficiency for production. *Physica Status Solidi (c)* **8***(10) 2978–2981 (2011).*

[139] V. SMIRNOV, W. BÖTTLER, A. LAMBERTZ, H. WANG, R. CARIUS *and* F. FINGER. Microcrystalline silicon n-i-p solar cells prepared with microcrystalline silicon oxide μc-SiOx:H) n-layer. *Physica Status Solidi (c)* **7***(3-4) 1053–1056 (2010).*

[140] P. DELLI VENERI, L. V. MERCALDO *and* I. USATII. Silicon oxide based n-doped layer for improved performance of thin film silicon solar cells. *Applied Physics Letters* **97***(2) 023512 (2010).*

[141] B. JANTHONG, A. HONGSINGTHONG, T. KRAJANGSANG, L. ZHANG, P. SICHANUGRIST *and* M. KONAGAI. Novel a-Si:H/μc-Si:H tandem cell with lower optical loss. *Journal of Non-Crystalline Solids* **358***(17) 2478 – 2481 (2012).*

[142] C. BANERJEE, J. SRITHARATHIKHUN, A. YAMADA *and* M. KONAGAI. Fabrication of heterojunction solar cells by using microcrystalline hydrogenated silicon oxide film as an emitter. *Journal of Physics D: Applied Physics* **41***(18) 185107 (2008).*

[143] J. SRITHARATHIKHUN, F. JIANG, S. MIYAJIMA, A. YAMADA *and* M. KONAGAI. Optimization of p-Type Hydrogenated Microcrystalline Silicon Oxide Window Layer for High-Efficiency Crystalline Silicon Heterojunction Solar Cells. *Japanese Journal of Applied Physics* **48***(10) 101603 (2009).*

[144] K. DING, U. AEBERHARD, F. FINGER *and* U. RAU. Silicon heterojunction solar cell with amorphous silicon oxide buffer and microcrystalline silicon oxide contact layers. *physica status solidi (RRL) Rapid Research Letters* **6***(5) 193–195 (2012).*

[145] D. DAS *and* A. K. BARUA. Highly Conducting Undoped μc-SiO:H Films Prepared by RF Glow Discharge. *Japanese Journal of Applied Physics* **38***(Part 2, No. 7A) L697–L699 (1999).*

[146] R. CARIUS, R. FISCHER, E. HOLZENKAMPFER *and* J. STUKE. Photoluminescence in the amorphous system SiO[sub x]. *Journal of Applied Physics* **52***(6) 4241–4243 (1981).*

[147] A. J. BENNETT *and* L. M. ROTH. Calculation of the Optical Properties of Amorphous SiO_x Materials. *Phys. Rev. B* **4** *2686–2696 (Oct 1971).*

[148] M. LANNOO *and* G. ALLAN. A cluster plus effective medium tight-binding study of SiOx systems. *Solid State Communications* **28***(9) 733 – 739 (1978).*

[149] S. KIRNER, O. GABRIEL, B. STANNOWSKI, B. RECH *and* R. SCHLATMANN. The growth of microcrystalline silicon oxide thin films studied by in situ plasma diagnostics. *Applied Physics Letters* **102***(5) 051906 (2013).*

[150] A. SARKER, C. BANERJEE *and* A. K. BARUA. Preparation and characterization of n-type microcrystalline hydrogenated silicon oxide films. *Journal of Physics D: Applied Physics* **35***(11) 1205 (2002).*

[151] L. GUO, M. KONDO, M. FUKAWA, K. SAITOH *and* A. MATSUDA. High Rate Deposition of Microcrystalline Silicon Using Conventional Plasma-Enhanced Chemical Vapor Deposition. *Japanese Journal of Applied Physics* **37***(Part 2, No. 10A) L1116–L1118 (1998).*

[152] M. FUKAWA, S. SUZUKI, L. GUO, M. KONDO *and* A. MATSUDA. High rate growth of microcrystalline silicon using a high-pressure depletion method with VHF plasma. *Solar Energy Materials and Solar Cells* **66***(14) 217 – 223 (2001).*

[153] J. K. RATH, R. H. J. FRANKEN, A. GORDIJN, R. E. I. SCHROPP *and* W. J. GOEDHEER. Growth mechanism of microcrystalline silicon at high pressure conditions. *Journal of Non-Crystalline Solids* **338-340** *56–60 (JUN 15 2004).*

[154] A. LAMBERTZ, F. FINGER, B. HOLLAENDER, J. K. RATH *and* R. E. I. SCHROPP. Boron-doped hydrogenated microcrystalline silicon oxide (μc-SiOx:H) for application in thin-film silicon solar cells. *Journal of Non-Crystalline Solids* **358***(17) 1962 – 1965 (2012).*

[155] M. ISOMURA, T. KINOSHITA *and* S. TSUDA. Boron-compensation effect on hydrogenated amorphous silicon with oxygen and nitrogen impurities. *Applied Physics Letters* **68***(9) 1201–1203 (1996).*

[156] J. I. PANKOVE, P. J. ZANZUCCHI, C. W. MAGEE *and* G. LUCOVSKY. Hydrogen localization near boron in silicon. *Applied Physics Letters* **46***(4) 421–423 (1985).*

[157] N. M. JOHNSON. Mechanism for hydrogen compensation of shallow-acceptor impurities in single-crystal silicon. *Phys. Rev. B* **31** *5525–5528 (Apr 1985).*

[158] Y. DU, Y. ZHANG, Q. GUO-GANG *and* W. SHI-FU. Localized vibrational mode infrared absorption of BH pair in silicon. *Solid State Communications* **55***(6) 501 – 503 (1985).*

[159] T. ROSCHEK, J. MÜLLER, S. WIEDER, B. RECH *and* H. WAGNER. Microcrystalline p-Layers Prepared by RF-PECVD for Silicon Thin Film Solar Cells with Zinc Oxide Front Contact. *In* Proceedings of the 16th European Photovoltaic Solar Energy Conference *(2000).*

[160] K. J. LAIDLER. Chemical Kinetics. *McGraw-Hill (1965).*

[161] J. PERRIN, Y. TAKEDA, N. HIRANO, Y. TAKEUCHI *and* A. MATSUDA. Sticking and recombination of the SiH3 radical on hydrogenated amorphous silicon: The catalytic effect of diborane. *Surface Science* **210***(1-2) 114 – 128 (1989).*

[162] S. KAMANARU, T. NAGAI, H. SANNAI, J. CHANTANA *and* Y. SOBAJIMA. Investigation of Growth Process in p-type μc-Si:H for Thin Film-Si Solar Cells. *In* Proceedings of 25th European Photovoltaic Solar Energy Conference and Exhibition *(2010).*

[163] M. GOERLITZER, P. TORRES, N. BECK, N. WYRSCH, H. KEPPNER, J. POHL *and* A. SHAH. Structural properties and electronic transport in intrinsic microcrystalline silicon deposited by the VHF-GD technique. *Journal of Non-Crystalline Solids* **227-230, Part 2***(0) 996 – 1000 (1998).*

[164] F. FINGER, R. CARIUS, T. DYLLA, S. KLEIN, S. OKUR *and* M. GUNES. Stability of microcrystalline silicon for thin film solar cell applications. *Circuits, Devices and Systems, IEE Proceedings -* **150***(4) 300–8– (2003).*

[165] D. A. ANDERSON *and* W. E. SPEAR. Electrical and optical properties of amorphous silicon carbide, silicon nitride and germanium carbide prepared by the glow discharge technique. *Philosophical Magazine* **35***(1) 1–16 (1977).*

[166] J. BULLOT *and* M. P. SCHMIDT. Physics of Amorphous Silicon - Carbon Alloys. *physica status solidi (b)* **143***(2) 345–418 (1987).*

[167] B. RECH, C. BENEKING *and* H. WAGNER. Improvement in stabilized efficiency of a-Si:H solar cells through optimized p/i-interface layers. *Solar Energy Materials and Solar Cells* **41 - 42***(0) 475 – 483 (1996).*

[168] R. FLÜCKIGER, J. MEIER, A. SHAH, J. POHL, M. TZOLOV *and* R. CARIUS. Structural, Optical and Electrical Properties of μc-SiC:H Thin Films Deposited by the VHF-GD. *MRS Online Proceedings Library* **358** *(0 1994).*

[169] F. FINGER. *Forschungszentrum Jülich - Private Communication (2012).*

[170] T. FUTAGI, M. KATSUNO, N. OHTANI, Y. OHTA, H. MIMURA *and* K. KAWAMURA. Highly conductive and wide optical band gap n-type mu c-SiC prepared by electron cyclotron resonance plasma-enhanced chemical vapor deposition. *Applied Physics Letters* **58***(25) 2948–2950 (1991).*

[171] W. MA, C. C. LIM, T. SAIDA, H. OKAMOTO *and* Y. HAMAKAWA. Microcrystalline silicon carbide - New useful material for improvement of solar cell performance. *Solar Energy Materials and Solar Cells* **34***(1 - 4) 401 – 407 (1994).*

[172] E. ACHESON. Manufacturing of Graphite *(1895).*

[173] D. H. STUTZ, S. PROCHAZKA *and* J. LORENZ. Sintering and Microstructure Formation of β-Silicon Carbide. *Journal of the American Ceramic Society* **68***(9) 479 – 482 (1985).*

[174] GESTIS MATERIAL DATABASE. Siliciumcarbid. *Online 2013.*

[175] C. W. LIU *and* J. C. STURM. Low temperature chemical vapor deposition growth of beta-SiC on (100) Si using methylsilane and device characteristics. *Journal of Applied Physics* **82***(9) 4558–4565 (1997).*

[176] M. B. YU, RUSLI, S. F. YOON, Z. M. CHEN, J. AHN, Q. ZHANG, K. CHEW *and* J. CUI. Deposition of nanocrystalline cubic silicon carbide films using the hot-filament chemical-vapor-deposition method. *Journal of Applied Physics* **87***(11) 8155–8158 (2000).*

[177] S. MIYAJIMA, A. YAMADA *and* M. KONAGAI. Properties of Hydrogenated Microcrystalline Cubic Silicon Carbide Films Deposited by Hot Wire Chemical Vapor Deposition at a Low Substrate Temperature. *Japanese Journal of Applied Physics* **43***(9A/B) L1190–L1192 (2004).*

[178] S. KLEIN, A. DASGUPTA, F. FINGER, R. CARIUS *and* T. BRONGER. Electronic properties of low temperature microcrystalline silicon carbide prepared by Hot Wire CVD. *Thin Solid Films* **516***(5) 630 – 632 (2008).*

[179] A. DASGUPTA, Y. HUANG, L. HOUBEN, S. KLEIN, F. FINGER, R. CARIUS *and* M. LUYSBERG. Effect of filament and substrate temperatures on the structural and electrical properties of SiC thin films grown by the HWCVD technique. *Thin Solid Films* **516***(5) 622 – 625 (2008).*

[180] S. KLEIN, L. HOUBEN, R. CARIUS, F. FINGER *and* W. FISCHER. Structural properties of microcrystalline SiC deposited at low substrate temperatures by HWCVD. *Journal of Non-Crystalline Solids* **352***(9 - 20) 1376 – 1379 (2006).*

[181] Y. HUANG, A. DASGUPTA, A. GORDIJN, F. FINGER *and* R. CARIUS. Highly transparent microcrystalline silicon carbide grown with hot wire chemical vapor deposition as window layers in n-i-p microcrystalline silicon solar cells. *Applied Physics Letters* **90***(20) 203502 (2007).*

[182] S. KERDILES, A. BERTHELOT, F. GOURBILLEAU *and* R. RIZK. Low temperature deposition of nanocrystalline silicon carbide thin films. *Applied Physics Letters* **76***(17) 2373–2375 (2000).*

[183] T. RAJAGOPALAN, X. WANG, B. LAHLOUH, C. RAMKUMAR, PARTHA DUTTA *and* S. GANGOPADHYAY. Low temperature deposition of nanocrystalline silicon carbide films by plasma enhanced chemical vapor deposition and their structural and optical characterization. *Journal of Applied Physics* **94***(8) 5252–5260 (2003).*

[184] S. MIYAJIMA, M. SAWAMURA, A. YAMADA *and* M. KONAGAI. Effects of Hydrogen Dilution Ratio on Properties of Hydrogenated Nanocrystalline Cubic Silicon Carbide Films Deposited by Very High-Frequency Plasma-Enhanced Chemical Vapor Deposition. *Japanese Journal of Applied Physics* **46***(28) L693–L695 (2007).*

[185] MAURICE NUYS. Strukturelle und elektronische Eigenschaften stöchiometrischer Siliziumkarbidschichten hergestellt mittels niedertemperatur PECVD. *Diplomarbeit, RWTH Aachen (2010).*

[186] C. PALMA, M.C. ROSSI, C. SAPIA *and* E. BEMPORAD. Laser-induced crystallization of amorphous silicon-carbon alloys studied by Raman microspectroscopy. *Applied Surface Science* **138-139***(0) 24 – 28 (1999).*

[187] C. PALMA *and* C. SAPIA. Laser pattern-write crystallization of amorphous SiC alloys. *Journal of Electronic Materials* **29** *607–610 (2000).*

[188] S. URBAN *and* F. FALK. Laser crystallization of amorphous SiC thin films on glass. *Applied Surface Science* **184***(1-4) 356 – 361 (2001).*

[189] S. KIRNER. Modellierung und Charakterisierung von a-Si/a-Si Tandemsolarzellen. *Diplomarbeit, TU Berlin (2010).*

[190] S. KIRNER, S. CALNAN, O. GABRIEL, S. NEUBERT, M. ZELT, B. STANNOWSKI, B. RECH *and* R. SCHLATMANN. An improved silicon-oxide-based intermediate-reflector for micromorph solar cells. *Physica Status Solidi (c)* **9***(10-11) 2145–2148 (2012).*

[191] S. S. HEGEDUS, F. KAMPAS *and* J. XI. Current transport in amorphous silicon n/p junctions and their application as "tunnel" junctions in tandem solar cells. *Applied Physics Letters* **67***(6) 813–815 (1995).*

[192] J. A. WILLEMEN, M. ZEMAN *and* J. W. METSELAAR. Computer Modelling of Amorphous Silicon Tandem Cells. *In* Proceedings of 1st WCPC-I, Hawaii, *p. 599–602 (1994).*

[193] J. A. WILLEMEN. Modeling of Amorphous Silicon Single- and Multi-Junction Solar Cells. *Dissertation, TU Delft (1998).*

[194] G. A. M. HURKX. On the modelling of tunnelling currents in reverse-biased p-n junctions. *Solid-State Electronics* **32***(8) 665 – 668 (1989).*

[195] G. A. M. HURKX, D. B. M. KLAASSEN *and* M. P. G. KNUVERS. A new recombination model for device simulation including tunneling. *Electron Devices, IEEE Transactions on* **39***(2) 331 –338 (feb 1992).*

[196] M. VUKADINOVIC, F. SMOLE, M. TOPIC, R. E. I. SCHROPP *and* F. A. RUBINELLI. Transport in tunneling recombination junctions: A combined computer simulation study. *Journal of Applied Physics* **96***(12) 7289–7299 (2004).*

[197] F. A. RUBINELLI, J. K. RATH *and* R. E. I. SCHROPP. Microcrystalline n-i-p tunnel junction in a-Si:H/a-Si:H tandem cells. *Journal of Applied Physics* **89***(7) 4010–4018 (2001).*

[198] J. Y. HOU, J. K. ARCH *and* S. J. FONASH. An Examination of the Tunnel Junctions in Triple Junction a-Si:H Based Solar Cells: Modeling and Effects on Performance. *In* Proceedings of the 22nd IEEE PVSC *(1991).*

[199] G. JUSKA, J. KOCKA, K. ARLAUSKAS *and* G. JUKONIS. Electron drift mobility in a-Si : H under extremely high electric field. *Solid State Communications* **75***(6) 531 – 533 (1990).*

[200] J. FURLAN. Tunnelling generation recombination currents in a-Si junctions. *Progress in Quantum Electronics* **25***(2) 55 – 96 (2001).*

[201] Y. SAKAI, K. FUKUYAMA, M. MATSUMURA, Y. NAKATO *and* H. TSUBOMURA. The effect of interposing thin oxide layers on the photovoltaic properties of a-Si:H solar cells II between the middle n and p layers of a tandem-type cell. *Journal of Applied Physics* **64***(1) 394–398 (1988).*

[202] M. KOLTER, C. BENEKING, D. PAVLOV, T. EICKHOFF, P. HAPKE, S. FROHNHOFF, H. MUENDER *and* H. WAGNER. Highly conductive microcrystalline n-layers for amorphous silicon stacked solar cells: preparation, properties, and device application. *In* Photovoltaic Specialists Conference, 1993., Conference Record of the Twenty Third IEEE, *p. 1031–1036 (1993).*

[203] O. GABRIEL, S. KIRNER, C. LEENDERTZ, M. GERHARDT, A. HEIDELBERG, H. BLOESS, R. SCHLATMANN *and* B. RECH. Large area PECVD of a-Si:H/a-Si:H tandem solar cells. *physica status solidi (c)* **8***(10) 2982–2985 (2011).*

[204] M. TANAKA, M. TAGUCHI, T. MATSUYAMA, T. SAWADA, S. TSUDA, S. NAKANO, H. HANAFUSA *and* Y. KUWANO. Development of New a-Si/c-Si Heterojunction Solar Cells: ACJ-HIT (Artificially Constructed Junction-Heterojunction with Intrinsic Thin-Layer). *Japanese Journal of Applied Physics* **31***(Part 1, No. 11) 3518–3522 (1992).*

[205] R. STANGL, A. FROITZHEIM, L. ELSTNER *and* FUHS W. Amorphous/crystalline silicon heterojunction solar cells, a simulation study. *In* Proceedings of the 17th European PVSEC, Munich, *p. 1387 – 1390 (2001).*

[206] M. SCHMIDT, L. KORTE, A. LAADES, R. STANGL, CH. SCHUBERT, H. ANGERMANN, E. CONRAD *and* K.V. MAYDELL. Physical aspects of a-Si:H/c-Si hetero-junction solar cells. *Thin Solid Films* **515***(19) 7475 – 7480 (2007).*

[207] R. BIRON, C. PAHUD, F.-J. HAUG, J. ESCARRE, K. SODERSTROM *and* C. BALLIF. Window layer with p doped silicon oxide for high V_{oc} thin-film silicon n-i-p solar cells. *Journal of Applied Physics* **110***(12) 124511 (2011).*

[208] S. KIRNER, M. HAMMERSCHMIDT, C. SCHWANKE, D. LOCKAU, S. CALNAN, T. FRIJNTS, S. NEUBERT, A. SCHOPKE, F. SCHMIDT, J.-H. ZOLLONDZ, A. HEIDELBERG, B. STANNOWSKI, B. RECH *and* R. SCHLATMANN. Implications of TCO Topography on Intermediate Reflector Design for a-Si/ μc-Si Tandem Solar Cells—Experiments and Rigorous Optical Simulations. *IEEE Journal of Photovoltaics* **4** *10 – 15 (2013).*

[209] J. KRC, F. SMOLE *and* M. TOPIC. Analysis of light scattering in amorphous Si:H solar cells by a one-dimensional semi-coherent optical model. *Prog. Photovolt: Res. Appl.* **11***(1) 15–26 (2003).*

[210] D. DOMINÉ, J. BAILAT, J. STEINHAUSER, A. SHAH *and* C. BALLIF. Micromorph Solar Cell Optimization using a ZnO Layer as Intermediate Reflector. *In* Photovoltaic Energy Conversion, Conference Record of the 2006 IEEE 4th World Conference on, *Bd. 2, p. 1465 –1468 (may 2006).*

[211] D. LOCKAU. Optical modeling of thin film silicon solar cells with random and periodic light management textures. *Dissertation, TU Berlin (2012).*

[212] CHRISTOPH SCHWANKE. 2D Optical Simulation of the Micromorph Solar Cell. *Diplomarbeit, HU Berlin (2012).*

[213] C. NOCK. Analytik des Streuverhaltens von Schichtsystemen für Solarzellen mittels winkelaufgelöster Streulichtmessungen. *Diplomarbeit, TU Berlin (2012).*

[214] A. BIELAWNY, C. ROCKSTUHL, F. LEDERER *and* R. B. WEHRSPOHN. Intermediate reflectors for enhanced topcell performance in photovoltaicthin-film tandem cells. *Opt. Express* **17***(10) 8439–8446 (May 2009).*

[215] STEPHAN FAHR, CARSTEN ROCKSTUHL *and* FALK LEDERER. The interplay of intermediate reflectors and randomly textured surfaces in tandem solar cells. *Applied Physics Letters* **97***(17) 173510 (2010).*

[216] C. ULBRICH, A. GERBER, K. HERMANS, A. LAMBERTZ *and* U. RAU. Analysis of short circuit current gains by an anti-reflective textured cover on silicon thin film solar cells. *Prog. Photovolt: Res. Appl. p. n/a–n/a (2012).*

List of publications

S. KIRNER, M. HAMMERSCHMIDT, C. SCHWANKE, D. LOCKAU, S. CALNAN, T. FRIJNTS, S. NEUBERT, A. SCHÖPKE, F. SCHMIDT, H. ZOLLONDZ, A. HEIDELBERG, B. STANNOWSKI, B. RECH and R. SCHLATMANN. *Implications of TCO Topography on Intermediate Reflector Design for a-Si/µc-Si Tandem Solar Cells – Experiments and Rigorous Optical Simulations*. IEEE Journal of Photovoltaics, submitted (2013).

S. KIRNER, O. GABRIEL, B. STANNOWSKI, B. RECH and R. SCHLATMANN. *The growth of microcrystalline silicon oxide thin films studied by in situ plasma diagnostics*. Applied Physics Letters **102**(5) 051906 (2013).

S. KIRNER, S. CALNAN, O. GABRIEL, S. NEUBERT, M. ZELT, B. STANNOWSKI, B. RECH and R. SCHLATMANN. *An improved silicon-oxide-based intermediate-reflector for micromorph solar cells*. Physica Status Solidi (c) **9**(10-11) 2145–2148 (2012).

B. STANNOWSKI, O. GABRIEL, S. CALNAN, T. FRIJNTS, A. HEIDELBERG, S. NEUBERT, S. KIRNER, S. RING, M. ZELT, B. RAU, J.-H. ZOLLONDZ, H. BLOESS, R. SCHLATMANN, B. RECH. *Achievements and challenges in thin film silicon module production*. Solar Energy Materials and Solar Cells, *submitted, http://dx.doi.org/10.1016/j.solmat.2013.06.043i* (2013).

M. HAMMERSCHMIDT, D. LOCKAU, S. BURGER, F. SCHMIDT, C. SCHWANKE, S. KIRNER, S. CALNAN, B. STANNOWSKI and B. RECH. *FEM-based optical modeling of silicon thin-film tandem solar cells with randomly textured interfaces in 3D*. Proceedings of SPIE 8620(2013).

O. GABRIEL, S. KIRNER, C. LEENDERTZ, M. GERHARDT, A. HEIDELBERG, H. BLOESS, R. SCHLATMANN and B. RECH. *Large area PECVD of a-Si:H/a-Si:H tandem solar cells*. Physica Status Solidi (c) **8**(10) 2982–2985 (2011).

Danksagung

Ich bedanke mich bei:

- Prof. Dr. Bernd Rech für die interessante Aufgabenstellung sowie für die Möglichkeit der Promotion am HZB.
- Prof. Dr. Rutger Schlatmann für die Leitung des PVcomB und die damit einhergehende Ermöglichung unserer Forschung an demselben.
- Dr. Bernd Stannowski für die engagierte Betreuung und das wiederholte Korrekturlesen.
- Dr. Sonya Calnan für das sehr detaillierte Korrekturlesen und Ihr immer offenes Ohr hinsichtich Fragen besonders zu TCOs.
- Dr. Onno Gabriel für das Korrekturlesen, sowie für die Möglichkeit von ihm so viel über Plasmaphysik und -diagnostik lernen zu können.
- Christoph Schwanke für die optischen 2D Simulationen und die interessanten Diskussion.
- Martin Hammerschmidt und Dr. Daniel Lockau für die 3D Simulationen und die vielen Diskussion, die mir sehr geholfen haben zum Verständnis der optischen Fragestellungen.
- Max Klingsporn für die TEM und die EDX Messungen und die super nette Zusammenarbeit.
- Sebastian Neubert für die vielen hilfreichen Diskussionen und das super ZnO:Al.
- Matthias Zelt für die Hilfe bei den vielen, vielen Depositionen.
- Martin Rohde für die viele Hilfe beim Kennenlernen der AKT.
- Gerald Troppens für die regelmäßigen Raman-Umbauten.
- Dr. Sven Ring für die hilfreichen Diskussionen und die super AFM Bilder.
- Dr. Felice Friedrich für die XRF Messungen.
- Tim Frijnts für viele gute Ideen und Anregungen.
- Dr. Caspar Leendertz, Dr. Rolf Stangl und Ana-Maria Teodoreanu für die Hilfe mit AFORS-HET.
- Katrin Frank für die viele Hilfe und den kontinuierlichen Substratnachschub.
- Karolina Mack, Tobias Hänel und Daniel Kubsch für die Hilfe bei den vielen Messungen und für die Wartung und Pflege der Messaufbauten.
- Dr. Moshe Weizman für viele hilfreiche Diskussionen und die Organisation der wöchentlichen

Leibesertüchtigung.

- Dr. Florian Ruske für viele interessante Diskussionen.
- Dr. Björn Rau für die Ermöglichung der Infrastuktur am PVcomB und die Wahrung der Sicherheit.
- Martin Reiche für die Hilfe und die Ratschläge bei den SiC Depositionen.
- Dr. Daniel Amkreutz und Paul Plocica für die E-Beam Kristallisationen.
- Dr. Andreas Schöpke für die AFM Messungen.
- Den Studenten am PVcomB für das Messen unzähliger Zellen und die damit einhergehende Aufrechterhaltung der Baseline: Martin Heckmann, Corinna Nock, Tobias Rückwaldt, Ivo Kirschner, Florian Welker (auch für das ZnO:Al), Roland Wintzer (besonders für die vielen interessanten Mittagsdiskussionen auch abseits vom Silizium).
- Meiner Familie und meinen Freunden für die Unterstützung und Abwechslung. Ganz besonders erwähnt seien hier meine Nachbarn Teo und Tobi.